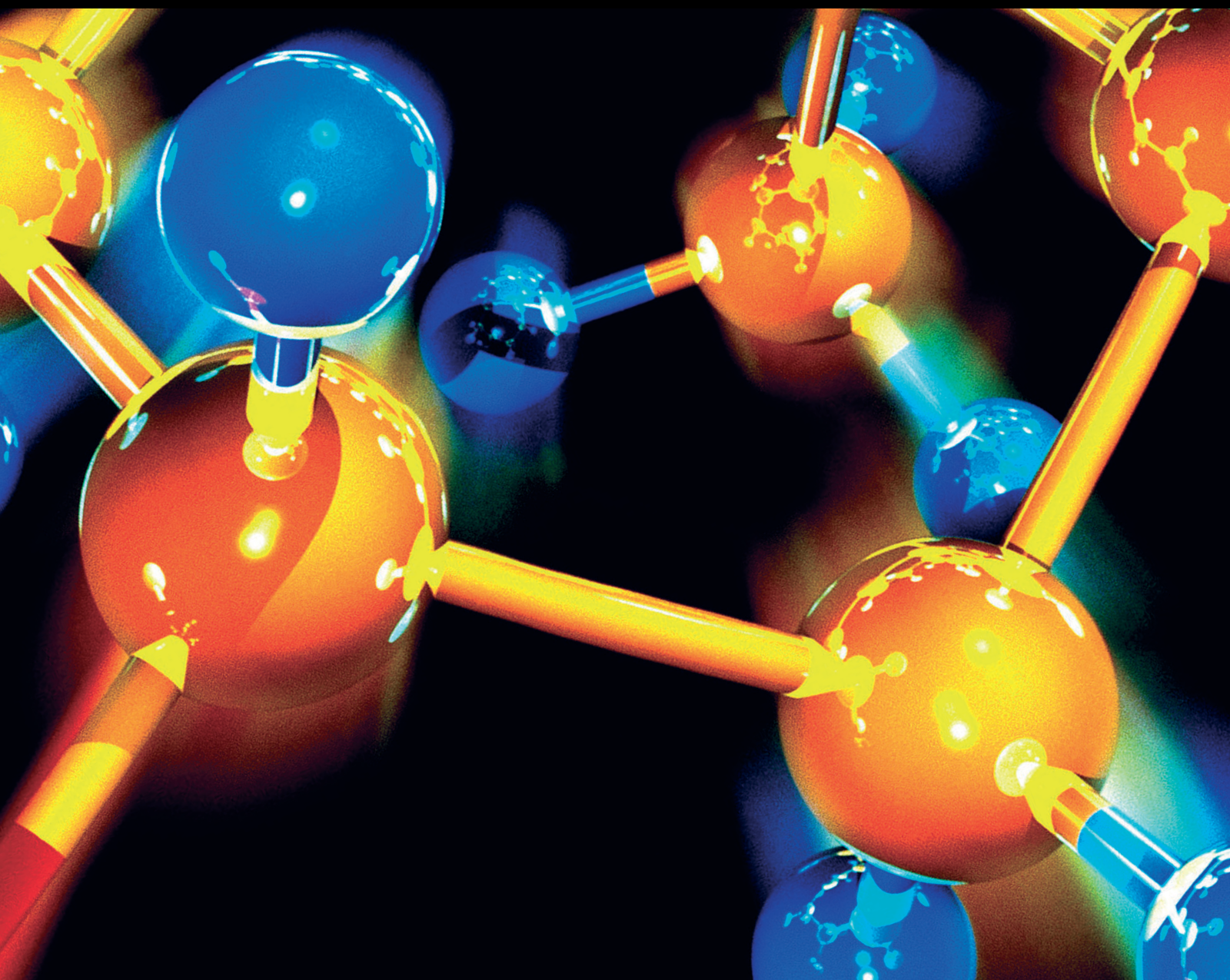


Journal of Chemistry

Chemistry in Combustion Science and Technology: From Molecules to Practices

Lead Guest Editor: Yaojie Tu

Guest Editors: Jiaqiang E. and Dezhi Zhou





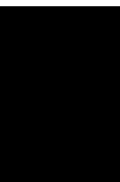
Chemistry in Combustion Science and Technology: From Molecules to Practices

Journal of Chemistry

**Chemistry in Combustion Science
and Technology: From Molecules to
Practices**

Lead Guest Editor: Yaojie Tu

Guest Editors: Jiaqiang E. and Dezhi Zhou



Copyright © 2020 Hindawi Limited. All rights reserved.

This is a special issue published in "Journal of Chemistry." All articles are open access articles distributed under the Creative Commons Attribution License, which permits unrestricted use, distribution, and reproduction in any medium, provided the original work is properly cited.

Chief Editor

Kaustubha Mohanty, India

Associate Editors

Mohammad Al-Ghouti, Qatar

Tingyue Gu , USA

Teodorico C. Ramalho , Brazil

Artur M. S. Silva , Portugal

Contents

Effect Analysis on Combustion and Emission Characteristics of a Rotary Burner Fueled by Biomass Pellet Fuel

Guohai Jia , Lijun Li , and D. M. Zhang


Research Article (12 pages), Article ID 3618382, Volume 2020 (2020)

Experimental Study on Spray Characteristics of Gasoline/Hydrogenated Catalytic Biodiesel under GCI Conditions

Wenhua Yuan , Jingjing Liao , Bei Li, and Wenjun Zhong




Research Article (9 pages), Article ID 4285460, Volume 2020 (2020)

Effects of Ethanol Blending on the Formation of Soot in *n*-Heptane/Air Coflow Diffusion Flame

Yuchen Ya, Xiaokang Nie, Licheng Peng, Longkai Xiang, Jialong Hu, Wenlong Dong, and Huaqiang Chu 


Research Article (10 pages), Article ID 8403940, Volume 2020 (2020)

Exploring the Benefits of Annular Rectangular Rib for Enhancing Thermal Efficiency of Nonpremixed Micro-Combustor

Hongcai Wang, Hongru Fang, Bingqian Lou, Shitu Abubakar , Yuqiang Li , and Lei Meng 


Research Article (13 pages), Article ID 9410389, Volume 2020 (2020)

Effect of Acetone-*n*-Butanol-Ethanol (ABE) as an Oxygenate on Combustion, Performance, and Emission Characteristics of a Spark Ignition Engine

Gang Wu, Deng Wu, Yuelin Li, and Lei Meng 

Research Article (11 pages), Article ID 7468651, Volume 2020 (2020)

Numerical Investigation of the Combustion in an Improved Microcombustion Chamber with Rib

Hai Chen  and Wei-qiang Liu

Research Article (12 pages), Article ID 8354541, Volume 2019 (2019)

Research Article

Effect Analysis on Combustion and Emission Characteristics of a Rotary Burner Fueled by Biomass Pellet Fuel

Guohai Jia ¹, Lijun Li ¹ and D. M. Zhang²

¹College of Mechanical and Electrical Engineering, Central South University of Forestry and Technology, Changsha 410004, China

²Department of Industrial Technology, California State University, Fresno, CA 93740-8002, USA

Correspondence should be addressed to Lijun Li; junlili1122@163.com

Received 11 October 2019; Revised 20 January 2020; Accepted 6 March 2020; Published 21 July 2020

Guest Editor: Yaojie Tu

Copyright © 2020 Guohai Jia et al. This is an open access article distributed under the Creative Commons Attribution License, which permits unrestricted use, distribution, and reproduction in any medium, provided the original work is properly cited.

A biomass pellet rotary burner was chosen as the research object, in order to study the influence of excess air coefficient on the combustion phenomenon of biomass rotary burner, the finite element simulation model of a biomass rotary burner was established, and simulation results of a biomass rotary burner were verified by the experiment. The computational fluid dynamics software was applied to simulate the combustion characteristics of biomass rotary burner in a steady-state condition, and the effect of excess air coefficient on temperature field and component concentration field in biomass rotary burner was analyzed. The results show that the flue gas flow rate inside the burner gradually increases with the increase of air velocity, the area with large temperature is mainly concentrated in the middle region of the rotary burner, and the maximum combustion temperature also appeared in the middle region of the combustion chamber, and the formation area of CO decreases with the increase of excess air coefficient. CO₂ is mainly concentrated in the middle region of the burner, and the CO₂ generating region decreases with the increase of excess air coefficient. The experimental value of the combustion temperature of the biomass rotary burner is in good agreement with the simulation results.

1. Introduction

With the rapid development of modern economy and technology, the energy crisis and air pollution from the combustion of fossil fuels have become increasingly serious [1–3]. In order to meet the requirements of resource and environment problems, many researches had been done to improve combustion technologies and look for alternatives to replace fossil fuels [4, 5]. Biomass pellet fuel is a typical biomass solid forming fuel, with high efficiency, clean, easy to ignition, CO₂ near-zero emissions, and so on [6–8]. It can replace coal and other fossil fuels used in cooking, heating, and other civilian areas and boiler combustion, power generation, and other industrial areas [9, 10].

In recent years, biomass pellet fuel is being developed rapidly in the EU, North America, and China [11–13]. Another advantage of biomass pellet fuel is that it can be used in small boilers, hot blast furnaces, and heating furnaces. The automatic control system is used to achieve the

continuous combustion of biomass pellet fuel burner. After years of research, biomass pellet burners are being developed rapidly. These burners mainly use wood pellets as fuel. Wood pellets have many advantages, such as high calorific value, low ash content, high ash melting point, and being not easy to slag after combustion [14, 15].

Khodaei et al. [16] addressed a comparative CFD-based analysis of different drying models. Several submodels were simulated to investigate the evaporation process of different geometries based on standard densified wood pellets. Buchmayr et al. [17] presented an accurate, time-efficient CFD approach for small-scale biomass combustion systems equipped with enhanced air staging. The model can handle the high amount of biomass tars in the primary combustion product at very low primary air ratios. Gas phase combustion in the freeboard was performed by the Steady Flamelet Model (SFM) together with a detailed heptane combustion mechanism. Farokhi et al. [18] presented a computational study to evaluate the influence of turbulence

and combustion models as well as chemistry schemes on the combustion of an 8–11 kW small lab-scale biomass furnace. Fagerström et al. [19] used a macro-TGA reactor to determine the release of ash forming elements during devolatilization and char combustion of single pellets. Soft wood and wheat straw were combusted at two temperatures (700°C and 1000°C), and the residual ashes were collected and analyzed for morphology, elemental, and phase composition. Roy et al. [20] presented combustion and emission results obtained using a prototype pellet furnace with 7–32 kW capacity (designed for burning high ash content pellet fuels) for four biomass pellets: one grass pellet and three wood pellets. Fuel property, gas emissions, and furnace efficiency are compared. Vicente and Alves [21] presented an extensive tabulation of particulate matter emission factors obtained worldwide and critically evaluated. Henderson et al. [22] explained how local economies can benefit from wood pellet manufacturing by expressing the economic multiplier effect of wood pellet plant operations in terms of employment, wages and salaries, and value-added in each of the 13 states in the U.S. South. Nunes et al. [23] studied several studies on the torrefaction of biomass for heat and power applications in the literature, which need to be reviewed and analyzed for further actions in the field, because significant gaps remain in the understanding of the biomass torrefaction process, which necessitate further study, mainly concerning the characterization of the torrefaction chemical reactions, investigation of equipment performance and design, and elucidation of supply chain impacts. Mobini et al. [24] used a dynamic simulation modeling approach to assess the integration of torrefaction into the wood pellet production and distribution supply chain. The developed a model that combined discrete event and discrete rate simulation approaches and allowed considering uncertainties, interdependencies, and resource constraints along the supply chain which were usually simplified or ignored in static and deterministic models.

Proskurina et al. [25] presented an overview of the current status of the Finnish wood pellet business and discussed the main opportunities and challenges facing the future development of the industry. Coelho et al. [26] studied several base case power plants and hybrid biomass/CSP options: wood gasification, refuse-derived fuel pellets, biogas from a wastewater anaerobic digester, and biogas from a landfill and natural gas. Roni et al. [27] investigated the existing cofiring plants with technologies and the availability of biomass resources in different countries of the world. Finally, this paper summarized the major global biomass cofiring initiatives and the prospects of biomass cofiring in securing renewable energy targets. Toklu [28] showed that there is an important biomass energy potential for climate change mitigation and energy sustainability in Turkey. Proskurina et al. [29] evaluated the potential of torrefied biomass in different industries, both power and nonpower generation industries, and considered the impact of such use on the international biomass market. Carvalho et al. [30] compared different technologies, such as CFB air and oxygen gasification, dual fluidized bed (DFB) steam gasification, and bio-synthetic natural gas (bio-SNG) production, focusing on the use of the product gas in an

iron ore pelletizing process located in the Southeast of Brazil. García et al. [31] analyzed thirteen alternative raw biomass samples and compared them with briquette, wood pellets, and charcoal and considered the data of their proximate, ultimate, and calorimetric analysis and physical properties. Silva et al. [32] evaluated the application potential of torrefaction in the solid fuel's production from lignocellulosic biomasses in Brazil. Xu et al. [33] evaluated the reductions in PM_{2.5}, organic carbon (OC) and elemental carbon (EC) emissions by comparing emission factors (EFs) among 19 combinations of biofuel/residential stove types measured using a dilution sampling system. Ahn and Jang [34] manufactured and tested a prototype of a 230 kW class wood pellet boiler employing a four-step grate. Ndibe et al. [35] investigated cofiring characteristics of torrefied biomass fuels at 50% thermal shares with coals and 100% combustion cases. Kraszkiwicz et al. [36] analyzed the results of the CO, NO, and SO₂ emission from burning pellets of oil cake, rape straw, and birch sawdust in the low-temperature water boiler of the top combustion. Chai and Saffron [37] optimized the biomass upgrading depot capacity and biomass feedstock moisture to obtain the minimum production cost at the depot gate to produce woody biofuels.

In this paper, a biomass pellet rotary burner with the spiral cleaning and slagging device was chosen as the research object in order to study the influence of excess air coefficient on the combustion efficiency. According to the combustion characteristics of the biomass (wood pellet), a high-efficiency double-layer combustion drum device has been designed to achieve a better flow distribution in this study. The flow velocity distribution characteristics in the burner have an important effect on the combustion efficiency of the biomass (wood pellet). The flow field distribution and combustion field distribution of the new biomass rotary burner are studied, which can reduce the test workload and shorten the design cycle. The CFD software was applied to simulate the combustion characteristics of biomass rotary burner in steady condition, and the effects of the excess air ratio on the temperature field and component concentration field in the biomass rotary burner were analyzed.

2. Numerical Model

2.1. Physical Model of Biomass Rotary Burner. In order to improve the thermal efficiency of the biomass rotary burner, a rotary combustion chamber has been used in the biomass rotary burner for reducing the pollutants. A screw feed device is used to control the appropriate amount of biomass (wood pellet). The schematic diagram of the biomass rotary burner is shown in Figure 1 which is mainly constituted by the spiral feeding mechanism, rotary combustion chamber, small combustion chamber, connecting flange, and other components.

When the burner is working, the biomass pellets are fed from the feed spiral tube into the rotary combustion chamber. The air is blown into the rotary combustion chamber through the secondary air pores to make the biomass particles burn completely. The combustion characteristics of the burner in the steady state are studied in the paper.

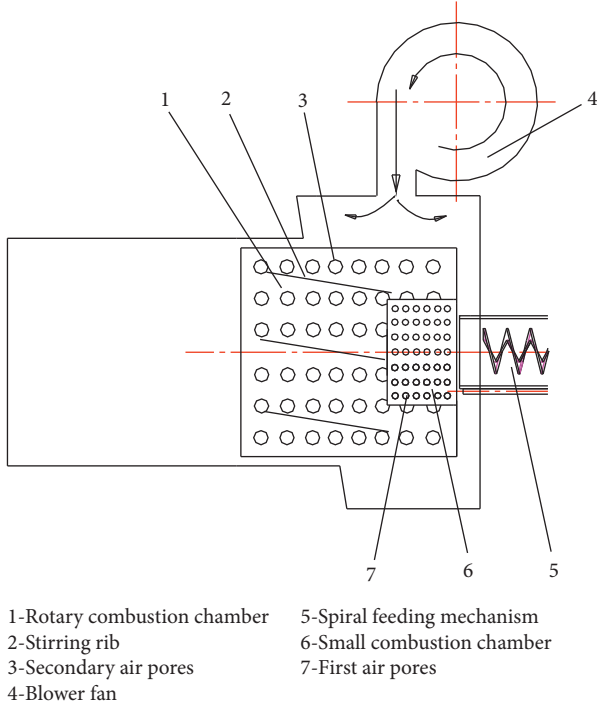


FIGURE 1: Schematic of biomass pellet rotary burner.

2.2. Mathematical Model. In this work, the combustion characteristics of the biomass rotary burner were studied by Fluent software. In the numerical calculation, the turbulent flow adopts the k - ε equation model, and the P-1 model was used to simulate the radiative heat transfer. The discrete phase particle trajectory was adopted. A power-diffusion limiting model was used in the stochastic tracking model for combustion. A two-step competitive reaction model was adopted for calculating volatile pyrolysis, and a mixture fraction/probability density function (PDF) was used for simulating gas phase turbulent combustion.

In the fluid simulation of biomass rotary burner, it is regarded as steady-state turbulent motion. The flow and heat transfer conservation equations of mass, momentum, and energy are as follows.

The mass conservation equation is

$$\operatorname{div}(\rho U) = 0, \quad (1)$$

where ρ is the fluid density and U is the fluid velocity vector.

The momentum conservation equation is

$$\left\{ \begin{array}{l} \operatorname{div}(\rho u U) = \operatorname{div}(\mu \operatorname{grad} u) - \frac{\partial p}{\partial x} + S_u, \\ \operatorname{div}(\rho v U) = \operatorname{div}(\mu \operatorname{grad} v) - \frac{\partial p}{\partial y} + S_v, \\ \operatorname{div}(\rho w U) = \operatorname{div}(\mu \operatorname{grad} w) - \frac{\partial p}{\partial z} + S_w, \end{array} \right. \quad (2)$$

where p is the fluid pressure, μ is the dynamic viscosity, and S_u , S_v , and S_w are the generalized source terms for the momentum conservation equation.

The energy conservation equation is

$$\operatorname{div}(\rho U T) = \operatorname{div}\left(\frac{h}{c_p} \operatorname{grad} T\right) + S_T, \quad (3)$$

where c_p is the specific heat capacity of fluid, T is the fluid temperature, h is the heat transfer coefficient of fluid, and S_T is the viscous dissipation term.

The turbulence kinetic equation and the turbulence stress equation which reflect the influence of the turbulence pulsation on flow can be obtained by the k - ε equation in the following form:

$$\frac{\partial(\rho k u_i)}{\partial x_i} = \frac{\partial}{\partial x_j} \left[\left(\mu + \frac{\mu_t}{\sigma_k} \right) \frac{\partial k}{\partial x_j} \right] + G_k - \rho \varepsilon + S_k, \quad (4)$$

where k is the turbulent kinetic energy, μ_t is the turbulent viscosity, G_k is the generation term of the turbulent kinetic k caused by mean velocity gradient, S_k is the source term of turbulent kinetic energy, and σ_k is the Prandtl number corresponding to the turbulent kinetic k .

$$\frac{\partial(\rho \varepsilon u_i)}{\partial x_i} = \frac{\partial}{\partial x_j} \left[\left(\mu + \frac{\mu_t}{\sigma_\varepsilon} \right) \frac{\partial \varepsilon}{\partial x_j} \right] + \frac{\varepsilon}{k} (C_{1\varepsilon} G_k - \rho \varepsilon G_{2\varepsilon}) + S_\varepsilon, \quad (5)$$

where ε is the turbulent dissipation rate, S_ε is the turbulent dissipation source, σ_ε is the Prandtl number corresponding to the turbulent kinetic energy dissipation ε , and $C_{1\varepsilon}$ and $C_{2\varepsilon}$ are the empirical constants, $\sigma_k = 1.0$, $\sigma_\varepsilon = 1.3$, $C_{1\varepsilon} = 1.44$, and $C_{2\varepsilon} = 1.92$.

In the mixed fraction model, the instantaneous thermochemical parameters of the fluid are related to the mixing fraction. The mixing fraction can be calculated by equation (6) according to the atomic mass fraction of the fuel and oxidant including the inert component:

$$f = \frac{Z_i - Z_{i,ox}}{Z_{i,fuel} - Z_{i,ox}}, \quad (6)$$

where Z_i is the elemental mass fraction of element i , the subscript ox is the value at the inlet of oxidant stream, and fuel is the value at the inlet of the fuel stream. The mixing fraction is the local mass fraction of all components (CO_2 , H_2O , O_2 , etc.) including the combusted and unburned fuel stream elements (C, H, etc.). The average (time average) mixed fraction and its mean square equation are

$$\left\{ \begin{array}{l} \frac{\partial}{\partial t} (\rho \bar{f}) + \nabla \cdot (\rho \bar{V} \bar{f}) = \nabla \cdot \left(\frac{\mu_t}{\sigma_f} \nabla \bar{f} \right) + S_m, \\ \frac{\partial}{\partial t} (\rho \overline{f'^2}) + \nabla \cdot (\rho \bar{V} \overline{f'^2}) = \nabla \cdot \left(\frac{\mu_t}{\sigma_f} \nabla \overline{f'^2} \right) + C_g \mu_t (\nabla^2 \bar{f}) \\ \quad - C_d \rho \frac{\varepsilon}{k} \cdot \overline{f'^2}, \end{array} \right. \quad (7)$$

where \bar{V} is the average velocity vector, m/s; μ_t is the turbulent viscosity, kg/(m·s); σ_f is the turbulent Prandtl number; S_m is the source term caused by chemical reaction, kg/(m³·s); and

C_g and C_d are the model constants which are 2.86 and 2.00, respectively.

For radiant heat flow q_r , it can be expressed by

$$q_r = \frac{1}{3(a + \sigma_s) - C\sigma_s} \nabla G, \quad (8)$$

where a is the absorption coefficient; σ_s is the scattering coefficient; G is the incident radiation, W/m^2 ; and C is the linear anisotropic phase function coefficient.

Introducing the parameter $\Gamma = 1/[3(a + \sigma_s) - C\sigma_s]$, equation (8) can be turned into

$$q_r = -\Gamma \nabla G. \quad (9)$$

The transport equation for G is

$$\nabla(\Gamma \nabla G) - aG + 4a\sigma T^4 = S_G, \quad (10)$$

where σ is the Stephen-Boltzmann constant, $5.67 \times 10^{-8} \text{ W}/(\text{m}^2 \cdot \text{K}^4)$; and S_G is the source term of user-defined radiation, W/m^2 .

When using the P-1 model, the local radiation intensity is used to solve this equation. Equation (11) can be calculated by combining equations (9) and (10):

$$-\nabla q_r = aG - 4a\sigma T^4, \quad (11)$$

where $-\nabla q_r$ is an expression that can be directly substituted into the energy equation to obtain a heat source due to radiation.

The precipitation of biomass volatiles was simulated using a two-competing-rate model, and the parameter was determined based on the properties of biomass.

$$\frac{m_v(t)}{(1 - f_{w,0})m_{p,0} - m_a} = \int_0^t (\alpha_1 R_1 + \alpha_2 R_2) \cdot \exp\left(-\int_0^t (R_1 + R_2) dt\right) dt, \quad (12)$$

where $m_v(t)$ is the mass of volatiles precipitated at time t , kg; $f_{w,0}$ is the initial volatile mass fraction of the particles; $m_{p,0}$ is the initial particle mass of the jet source, kg; m_a is the ash content of the particles, kg; α_1 and α_2 are production rate factors; and R_1 and R_2 are competitive precipitation rate constants, controlling the precipitation rate in different temperature ranges, $R_i = A_i \exp(-E_i/RT_p)$, $\text{kg}/(\text{kg} \cdot \text{s})$.

Through the experimental study, the components attached to the combustion are similar to coke which is very close to the chemical properties of coke. It is assumed that the coke surface reaction rate in the dynamic diffusion control combustion model is simultaneously controlled by the diffusion process and chemical reaction kinetics. The coke combustion rate is

$$\frac{dm_p}{dt} = -\pi d_p^2 p_{\text{ox}} \frac{aR}{a + R}, \quad (13)$$

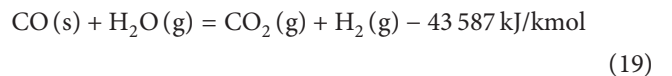
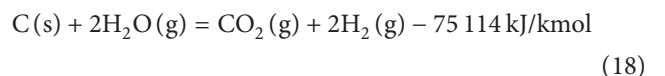
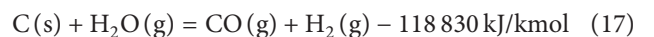
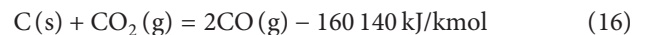
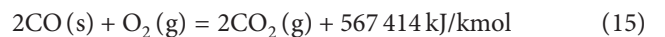
where R is the chemical reaction rate constant, $R = C_2 \exp(-E/RT_p)$, $\text{kg}/(\text{kg} \cdot \text{s})$; M_p is the current pellet mass of coke, kg; d_p is the current particle diameter of coke, m; and p_{ox} is the

partial pressure of oxidant in vapor phase around the coke particles.

2.3. Computational Mesh and Boundary. Before calculating by numerical simulation method, a 3D model of biomass pellet rotary burner was established. For making the calculation of the simulation model faster, the burner surface chamfer and fine structure were properly simplified without affecting the accuracy of the calculation. The fluid model in the burner was established by Gambit. The tetrahedral mesh was used to divide the body mesh of the fluid model in the burner. Figure 2 shows a three-dimensional volume model of fluid in the burner with a number of nodes of 133078 and a number of grids of 600240 after grid independence.

In this paper, the boundary conditions are set including the inlet velocity boundary, the pressure outlet boundary, and the wall boundary, and the near-wall region simulation uses the wall function method. The k - ϵ model is used to simulate turbulent gas phase flow, the scalar conserved mixed fractional probability density function is used to simulate volatile combustion, and the P-1 radiation model is used for simulation research to calculate the radiation exchange. The kinetic/diffusion control reaction rate model is used to simulate the coke combustion. The distribution characteristic of the solid phase particle is set to uniform. The Lagrange discrete phase model is used to calculate the interaction between the particle phase and the gas phase, and the random orbit model is used to track the particle motion. The WSGGM-domain-based model is used to calculate the absorption coefficient. The inlet boundary is set to the velocity inlet, and the temperature T is set to 300 K. The turbulence intensity is determined by the method of turbulence intensity and hydraulic diameter. The outlet boundary condition is set to the type of pressure outlet. In the process of simulating the adiabatic combustion, the wall is set to an adiabatic wall surface with no heat flux and mass flux. It is assumed that the velocity on the wall surface is zero. The proximate and ultimate analyses of the biomass pellet used in the simulation are listed in Table 1.

The productions of the volatile pyrolysis of the biomass fuel are CO, H₂, H₂O, and so forth. The pyrolysis equations of the combustion process are as follows:



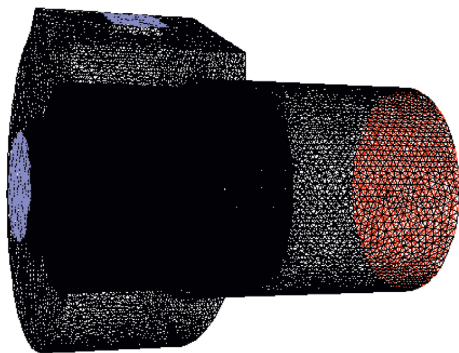


FIGURE 2: Three-dimensional mesh model of fluid in the burner.

TABLE 1: The proximate and ultimate analyses of China fir (air dry).

Proximate analysis				
	Mass ratio (%)			Lower heating value (MJ·kg ⁻¹)
Moisture	Ash	Volatile	Fixed carbon	
11.92	1.77	64.895	21.415	16.76

For simulating the combustion of the biomass pellet rotary burner, it is necessary to determine the independence between the grid and the calculated results. In the paper, four different density grids of the burner are divided, and the results are shown in Table 2.

It can be seen from the table that when the grid is increased to 845772, the maximum temperature of the outer burner remains substantially stable. When the grid is too dense, the simulation time and the computational cost will increase; therefore, the second grid is adopted in the analysis.

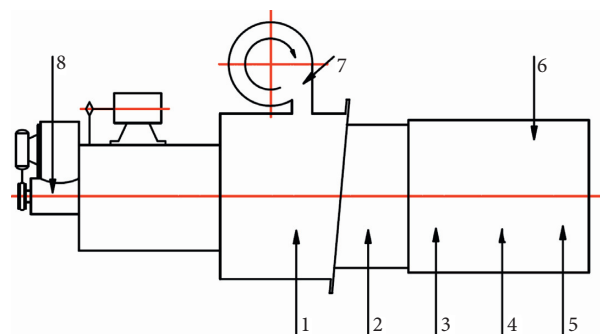
2.4. Model Validation. In order to test the simulation model, the team established a test bench for the biomass rotary burner. A schematic diagram of the test device for the biomass rotary burner is shown in Figure 3. It can be seen that the test instruments include thermocouples, flue gas analyzers, fan flow meters, and feed screw speed detection devices. Because this research mainly discusses the combustion efficiency of the burner, the temperature is the best evaluation index. Therefore, temperature measurement is the key condition of model validation. The measuring instruments used in the test are specially customized.

The test steps of the main experiments are as follows:

- (1) At the test site, all test devices required for the test platform are installed
- (2) Check that all test devices are complete and whether they are consistent with the predetermined size
- (3) Check the air tightness of the whole device, and check whether there is any loose connection
- (4) Install various sensors and measuring devices
- (5) Power on the instrument and ensure that all pipelines are connected
- (6) Carry out the experiment according to the experiment manual

TABLE 2: Results of the highest temperature of the outlet dependent on different grid densities.

Calculation method	1	2	3	4
Grid number	19 5064	338 087	62 3300	84 5772
Highest temperature (K)	1680	1700	1790	1760



1~5. Thermocouples
6. Flue gas analyzer
7. Fan flow meter
8. Feed spiral speed detection

FIGURE 3: Schematic diagram of the thermocouple position in the burner test device.

The biomass pellet fuel used in the test was fir wood pellet fuel which was compressed into a cylindrical shape by a fuel molding machine with a diameter of 5 mm. The processes are as follows:

- (1) Convey the wood pellet fuel by the screw conveyor; the conveying capacity of the conveyor was kept at 12 kg/h.
- (2) The hot air gun was energized, and the burner was heated by the hot air for about 10 minutes.
- (3) When the hot air gun was energized, the fan started to work, and then the wind was blasted into the combustion chamber.
- (4) When the flame was detected, the hot air gun was powered off and stops working. After that, the inlet valve was adjusted to change the intake air volume of the combustion chamber.

Only the measured temperature is reliable due to the error of measuring instruments caused by high temperatures.

It can be seen from Figures 4 and 5 that the experimental values of the combustion temperature of the biomass rotary burner are in good agreement with the simulation results, and the maximum error is 11.9%, because the model is appropriately simplified during the simulation.

3. Results and Discussions

In order to make a better comparison with the test results, the fir particle fuel has been chosen as the simulated fuel. Its ultimate and proximate analysis is shown in Table 1. The feed amount of biomass pellet fuel is set to 12 kg/h, and the

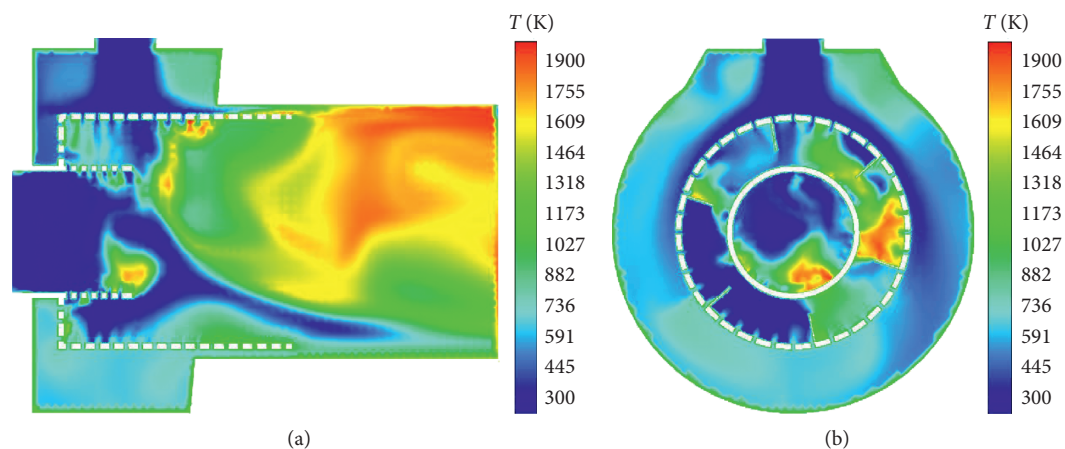


FIGURE 4: Temperature distribution of the gas phase in the burner. (a) Longitudinal distribution ($\alpha=1.2$). (b) Horizontal distribution ($\alpha=1.2$) ($Y=0.364$ m).

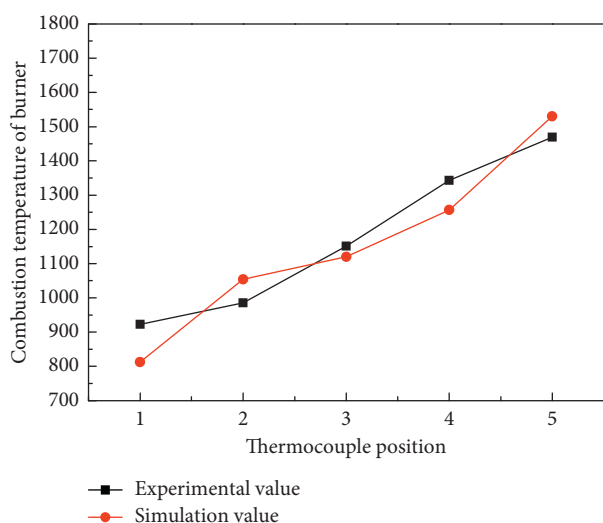


FIGURE 5: Comparison of simulation and experimental values of the burners' combustion temperature.

temperature field and CO, CO₂, and O₂ concentrations of the biomass pellet burner are numerically simulated under four conditions of excess air coefficient of 1.0, 1.4, 1.8, and 2.2.

3.1. Effect of Excess Air Coefficient on Temperature Distribution. Figure 6 shows the longitudinal distribution of the combustion temperature of the rotary burner under different excess air coefficients. It can be seen from Figure 6 that the temperature changes greatly and is mainly concentrated in the middle region of the rotary burner. The combustion temperature reaches the maximum in the middle region of the combustion chamber. With the increase of excess air ratio, the temperature is correspondingly reduced. When the excess air coefficient α is 1.0, 1.4, 1.8, and 2.2, the maximum temperature of the rotary combustion chamber is 1700 K, 1600 K, 1700 K, and 1600 K, respectively.

Figure 7 shows the temperature distribution along the longitudinal centerline of the burner under different excess air coefficients. It can be seen from Figure 7 that the maximum temperature decreases with the increase of excess air coefficient. This is because as the excess air coefficient standing for the fuel is larger, it will be blown to the tail of the burner before the combustion in the combustion chamber is completed. This will lead to an increase in the velocity of the burner outlet, which is consistent with the simulation results.

3.2. Effect of Excess Air Coefficient on CO Concentration Distribution. The CO concentration distribution of the burner is shown in Figure 8.

It can be seen that CO is mainly concentrated near the fuel inlet where the biomass fuel is richer than other areas, so the CO concentration is also richer, and the CO generating region decreases when the excess air coefficient increases. When the excess air coefficient α is 1.0, CO is almost distributed throughout the rotary combustion chamber, indicating that the oxygen supply is insufficient in this area. When the excess air coefficient α is 1.4, the CO concentration range decreases with the increase of the oxygen content, and it is limited to the small combustion chamber of biomass rotary burner. When the excess air coefficient α is 2.2, the CO concentration range is further reduced, and the range of the maximum CO concentration is greatly reduced.

Figure 9 shows the distribution of the CO concentration along the axial centerline of the burner under four operating conditions.

It can be seen from the curve in Figure 9 that the CO concentration under the four working conditions shows an approximate parabolic distribution. It increases rapidly first and then decreases slowly, indicating that the biomass fuel is enough when it enters the combustion chamber, and an incomplete combustion reaction occurs, and then the CO concentration increases. With the increase of O₂, CO undergoes further oxidation reaction to form CO₂, which causes the CO concentration to decrease, while the CO₂

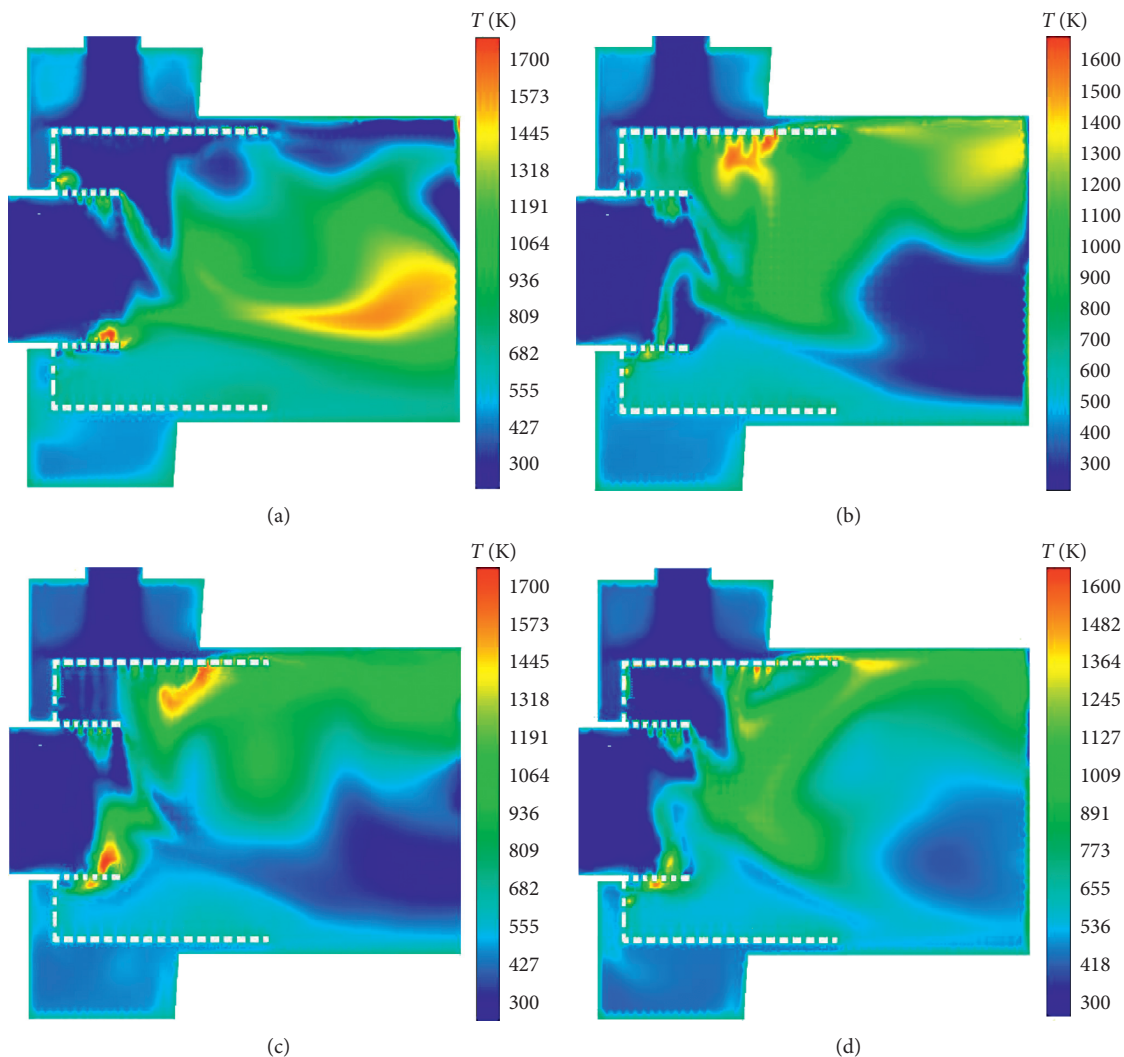


FIGURE 6: Longitudinal distribution of the combustion temperature of the rotary burner under different excess air coefficients. (a) $\alpha = 1.0$. (b) $\alpha = 1.4$. (c) $\alpha = 1.8$. (d) $\alpha = 2.2$.

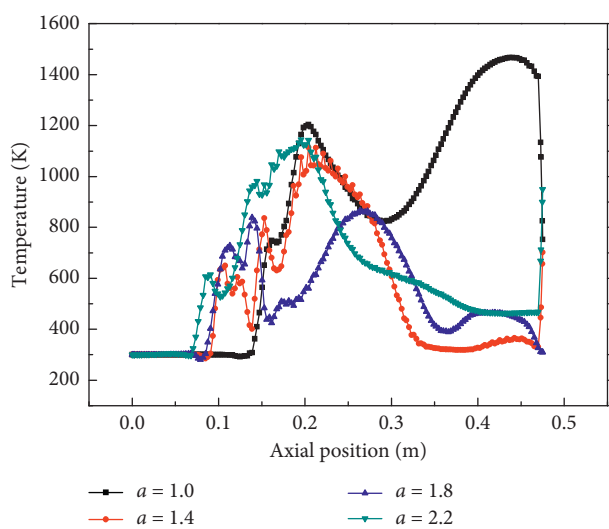


FIGURE 7: Temperature distribution along the longitudinal centerline of the burner under different excess air coefficients.

concentration is corresponding to increase. It can be seen that the CO concentration in the burner gradually decreases with the increase of the excess air coefficient.

3.3. Effect of Excess Air Coefficient on CO_2 Concentration Distribution. The CO_2 concentration distribution of the rotary burner is shown in Figure 10. The CO_2 concentration is mainly concentrated in the middle region of the burner. The CO_2 generating region decreases with the increase of the excess air coefficient. When the excess air coefficient α is 1.0, CO_2 is almost distributed throughout the rotary combustion chamber, indicating that biomass fuel is almost combusted completely. When the excess air coefficient α is 1.4, the area of the CO_2 concentration range decreases compared with the excess air coefficient 1.0. When the excess air coefficient α is 1.8, the CO_2 concentration range decreases with the increase of the oxygen content, and it is limited to the longitudinal region of the biomass rotary burner. When the excess air coefficient α is 2.4, the CO_2 concentration range is further

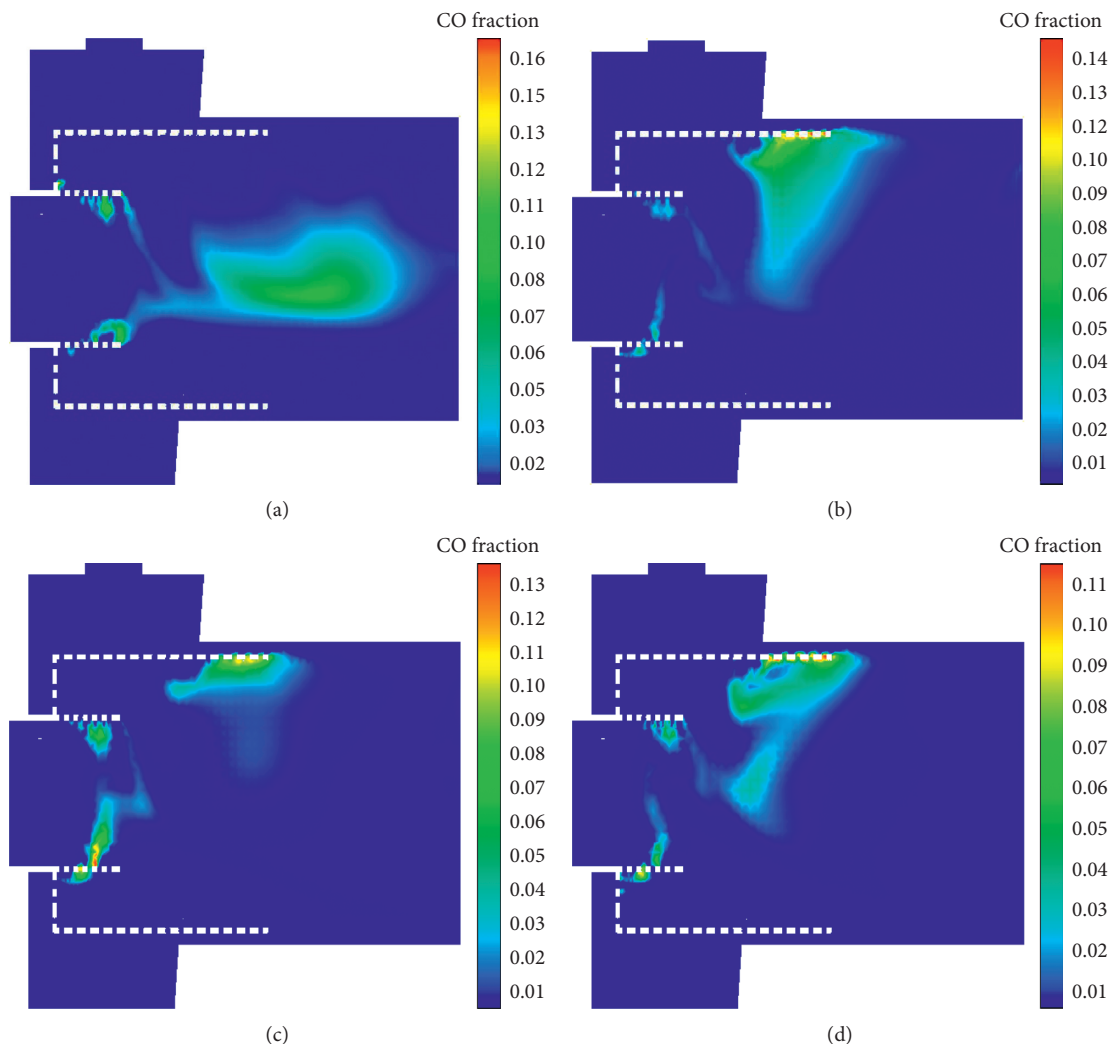


FIGURE 8: Longitudinal distribution of the CO concentration of the rotary burner under different excess air coefficients. (a) $\alpha = 1.0$. (b) $\alpha = 1.4$. (c) $\alpha = 1.8$. (d) $\alpha = 2.2$.

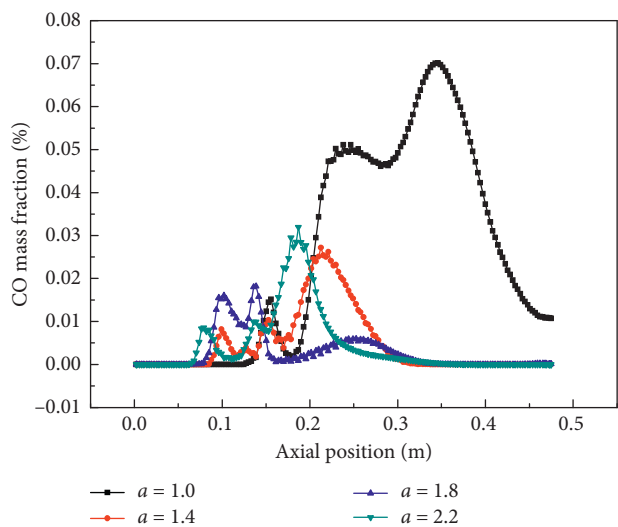


FIGURE 9: CO concentration distribution along the longitudinal centerline of the burner under different excess air coefficients.

reduced, and the range of the maximum CO_2 concentration is also greatly reduced.

Figure 11 shows the distribution of CO_2 concentration along the longitudinal centerline of the burner under four operating conditions. It can be seen from the curve in Figure 11 that the CO_2 concentration under the four operating conditions gradually increases with the reaction of combustion, and then it remains stable. As excess air coefficient increases, the CO_2 concentration in the burner is gradually reduced.

3.4. Effect of Excess Air Coefficient on O_2 Concentration Distribution. The O_2 concentration distribution of the burner is shown in Figure 12. As shown in Figure 12, O_2 is mainly concentrated near the airflow inlet at a lower excess air coefficient. When the excess air coefficient increases, the biomass fuel will burn faster and the O_2 region will increase with the increase of excess air coefficient. Figure 13 is a distribution curve of the O_2 concentration along the

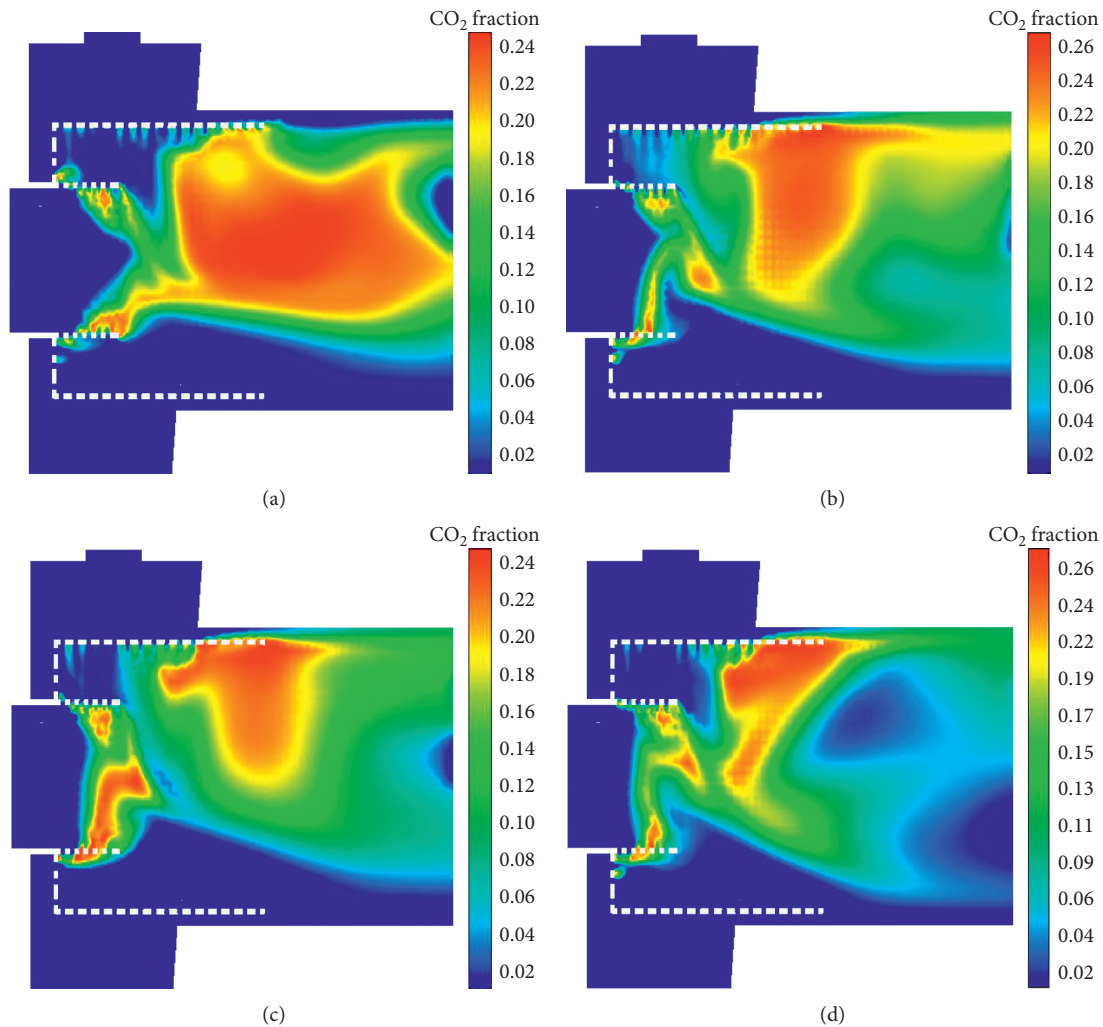


FIGURE 10: Longitudinal distribution of the CO_2 concentration of the rotary burner under different excess air coefficients. (a) $\alpha = 1.0$ (b) $\alpha = 1.4$. (c) $\alpha = 1.8$. (d) $\alpha = 2.2$.

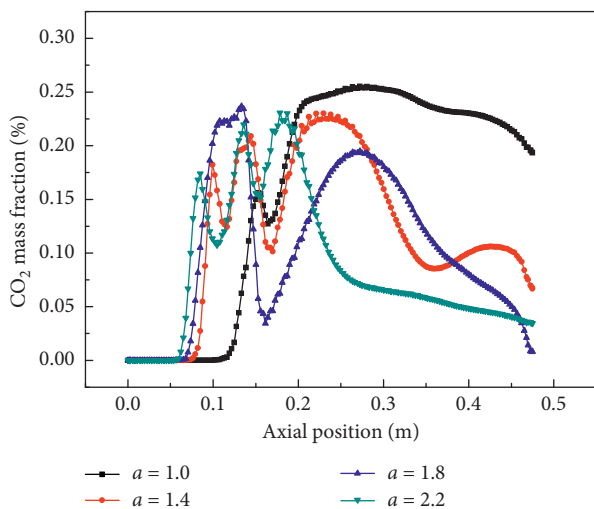


FIGURE 11: CO_2 concentration distribution along the longitudinal centerline of the burner under different excess air coefficients.

longitudinal centerline of the burner under four operating conditions. As shown in Figure 13, the distribution of O_2 concentration gradually increases with the increase of excess air coefficient under the four operating conditions. At a lower excess air coefficient, oxygen is concentrated mainly near the airflow inlet. The middle and lower regions of the burner form a relatively low oxygen atmosphere.

3.5. Current and Future Developments. It is a very important research topic to improve combustion efficiency [38–40] and reduce pollutant emissions [41–46] by changing the shape and structure size of the burners. As for the swirl burner, the latter research should be based on the existing model research and carry out relevant simulation and experimental research. Relevant model modification and parameter sensitivity should be explored. The internal distribution and main distribution trend of the flow field are obtained. The computational fluid dynamics software can be applied to

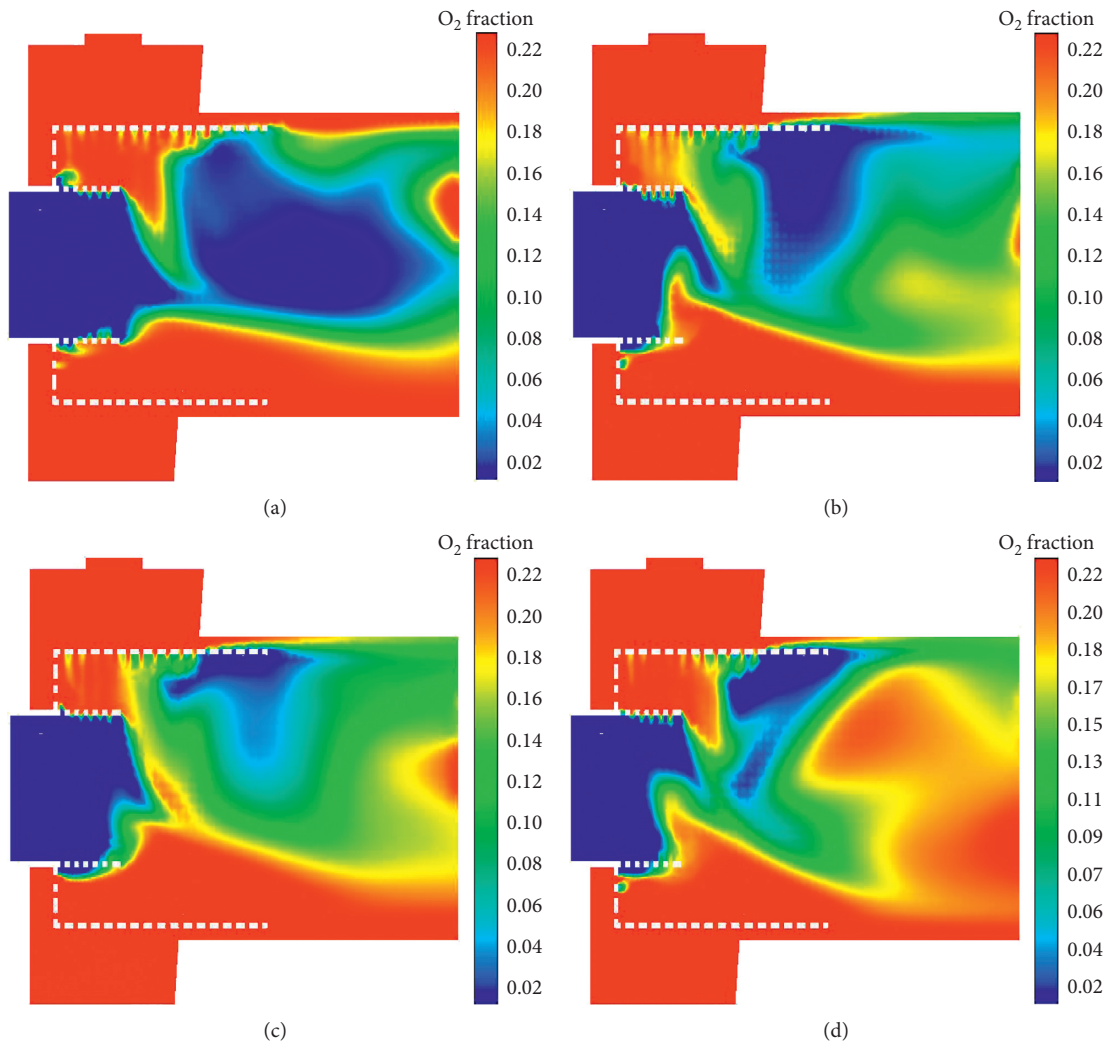


FIGURE 12: Longitudinal distribution of the O₂ concentration of the rotary burner under different excess air coefficients. (a) $\alpha = 1.0$. (b) $\alpha = 1.4$. (c) $\alpha = 1.8$. (d) $\alpha = 2.2$.

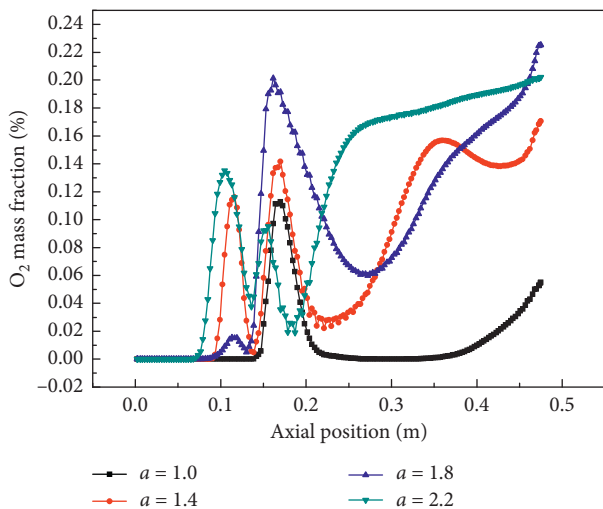


FIGURE 13: O₂ concentration distribution along the longitudinal centerline of the burner under different excess air coefficients.

simulate the combustion characteristics of the biomass rotary burner in steady condition. The structure of the swirl burner will be more reasonable and it can use fuel efficiently.

4. Conclusions

Through the simulation and experimental research on the combustion characteristics of the biomass rotary burner, the conclusions are obtained as follows:

- (1) The area where the temperature changes greatly is mainly concentrated in the middle part of the rotary combustor, the combustion temperature reaches the maximum in this region, and the temperature is smaller in other regions. According to the simulation results, the temperature of the burner decreases with the increase of the excess air coefficient.
- (2) CO is mainly concentrated near the fuel inlet, because the excess air coefficient is bigger than other

areas, so CO is richer than other regions. According to the simulation results, the region of CO decreases with the increase of the excess air coefficient. CO₂ is mainly concentrated in the middle region of the burner and the CO₂ generating region decreases with the increase of excess air coefficient. O₂ is mainly concentrated near the airflow inlet at lower excess air coefficient, and the biomass fuel burns faster and O₂ region also increases with the increase of excess air coefficient.

- (3) The experimental values of the combustion temperature of the biomass rotary burner are in good agreement with the simulation results. It is because the model is appropriately simplified in the simulation.

Nomenclature

ρ :	The fluid density, kg/m ³
c_p :	The specific heat of fluid, J/(kg·K)
U :	The velocity field, m/s
T :	The temperature, K
h :	The thermal conductivity, W/(m·K)
p :	The fluid pressure, Pa
μ :	The dynamic viscosity, Pa·s
S_w, S_v ,	The generalized source terms for the momentum conservation equation
k :	The turbulent kinetic energy, J
μ_t :	The turbulent viscosity, kg/(m·s)
G_k :	The generation term of the turbulent kinetic, J
S_k :	The source term of turbulent kinetic energy, J
σ_k :	The Prandtl number
\bar{V} :	The average velocity vector, m/s
S_m :	The source term caused by chemical reaction, kg/(m ³ ·s)
a :	The absorption coefficient
σ_s :	The scattering coefficient
G :	The incident radiation, W/m ²
C :	The linear anisotropic phase function coefficient
S_G :	The source term of user-defined radiation, W/m ² .

Data Availability

The data in this paper are provided by the manufacturer company, which involves product matching and technical parameters of the company.

Conflicts of Interest

The authors declare that they have no conflicts of interest regarding the publication of this paper.

Acknowledgments

This work was supported by the China Post-doctoral Science Foundation (2016M592455), Hunan Provincial Education Department's Scientific Research Project (17B278), Hunan Provincial University's Science and Technology Innovation Team Support Plan (2014207), and Central South University

of Forestry and Technology's School-level Youth Science Foundation Project (QJ2017006B).

References

- [1] D. Zhao and L. Li, "Effect of choked outlet on transient energy growth analysis of a thermoacoustic system," *Applied Energy*, vol. 160, pp. 502–510, 2015.
- [2] J. Chen, W. Xu, H. Zuo et al., "System development and environmental performance analysis of a solar-driven supercritical water gasification pilot plant for hydrogen production using life cycle assessment approach," *Energy Conversion and Management*, vol. 184, pp. 60–73, 2019.
- [3] H. Zuo, G. Liu, E. Jiaqiang et al., "Catastrophic analysis on the stability of a large dish solar thermal power generation system with wind-induced vibration," *Solar Energy*, vol. 183, pp. 40–49, 2019.
- [4] X. Zhao, G. Wu, E. Jiaqiang et al., "A review of studies using graphenes in energy conversion, energy storage and heat transfer development," *Energy Conversion and Management*, vol. 184, pp. 581–599, 2019.
- [5] E. Jiaqiang, G. Liu, Z. Zhang et al., "Effect analysis on cold starting performance enhancement of a diesel engine fueled with biodiesel fuel based on an improved thermodynamic model," *Applied Energy*, vol. 243, pp. 321–335, 2019.
- [6] E. Jiaqiang, J. Gao, Q. Peng, Z. Zhang, and P. M. Hieu, "Effect analysis on pressure drop of the continuous regeneration-diesel particulate filter based on NO₂ assisted regeneration," *Applied Thermal Engineering*, vol. 100, pp. 356–366, 2016.
- [7] E. Jiaqiang, Z. Zhang, J. Chen et al., "Performance and emission evaluation of a marine diesel engine fueled by water biodiesel-diesel emulsion blends with a fuel additive of a cerium oxide nanoparticle," *Energy Conversion and Management*, vol. 169, pp. 194–205, 2018.
- [8] E. Jiaqiang, X. Zhao, L. Xie et al., "Performance enhancement of microwave assisted regeneration in a wall-flow diesel particulate filter based on field synergy theory," *Energy*, vol. 169, pp. 719–729, 2019.
- [9] Z. Zhang, E. Jiaqiang, Y. Deng et al., "Effects of fatty acid methyl esters proportion on combustion and emission characteristics of a biodiesel fueled marine diesel engine," *Energy Conversion and Management*, vol. 159, pp. 244–253, 2018.
- [10] Z. Zhang, E. Jiaqiang, J. Chen et al., "Effects of low-level water addition on spray, combustion and emission characteristics of a medium speed diesel engine fueled with biodiesel fuel," *Fuel*, vol. 239, pp. 245–262, 2019.
- [11] D. Zhao, E. Gutmark, and P. de Goey, "A review of cavity-based trapped vortex, ultra-compact, high-g, inter-turbine combustors," *Progress in Energy and Combustion Science*, vol. 66, pp. 42–82, 2018.
- [12] D. Zhao, C. Ji, X. Li, and S. Li, "Mitigation of premixed flame-sustained thermoacoustic oscillations using an electrical heater," *International Journal of Heat and Mass Transfer*, vol. 86, pp. 309–318, 2015.
- [13] J. Chen, Y. Fan, E. Jiaqiang et al., "Effects analysis on the gasification kinetic characteristics of food waste in supercritical water," *Fuel*, vol. 241, pp. 94–104, 2019.
- [14] E. Jiaqiang, G. Liu, T. Liu et al., "Harmonic response analysis of a large dish solar thermal power generation system with wind-induced vibration," *Solar Energy*, vol. 181, pp. 116–129, 2019.
- [15] Y. Li, W. Tang, Y. Chen, J. Liu, and C.-f. F. Lee, "Potential of acetone-butanol-ethanol (ABE) as a biofuel," *Fuel*, vol. 242, pp. 673–686, 2019.

- [16] H. Khodaei, G. H. Yeoh, F. Guzzomi, and J. Porteiro, "A CFD-based comparative analysis of drying in various single biomass particles," *Applied Thermal Engineering*, vol. 128, pp. 1062–1073, 2018.
- [17] M. Buchmayr, J. Gruber, M. Hargassner, and C. Hochenauer, "A computationally inexpensive CFD approach for small-scale biomass burners equipped with enhanced air staging," *Energy Conversion and Management*, vol. 115, pp. 32–42, 2016.
- [18] M. Farokhi, M. Birouk, and F. Tabet, "A computational study of a small-scale biomass burner: the influence of chemistry, turbulence and combustion sub-models," *Energy Conversion and Management*, vol. 143, pp. 203–217, 2017.
- [19] J. Fagerström, E. Steinvall, D. Boström, and C. Boman, "Alkali transformation during single pellet combustion of soft wood and wheat straw," *Fuel Processing Technology*, vol. 143, pp. 204–212, 2016.
- [20] M. M. Roy, A. Dutta, and K. Corscadden, "An experimental study of combustion and emissions of biomass pellets in a prototype pellet furnace," *Applied Energy*, vol. 108, pp. 298–307, 2013.
- [21] E. D. Vicente and C. A. Alves, "An overview of particulate emissions from residential biomass combustion," *Atmospheric Research*, vol. 199, pp. 159–185, 2018.
- [22] J. E. Henderson, O. Joshi, R. Parajuli, and W. G. Hubbard, "A regional assessment of wood resource sustainability and potential economic impact of the wood pellet market in the U.S. South," *Biomass and Bioenergy*, vol. 105, pp. 421–427, 2017.
- [23] L. J. R. Nunes, J. C. O. Matias, and J. P. S. Catalão, "A review on torrefied biomass pellets as a sustainable alternative to coal in power generation," *Renewable and Sustainable Energy Reviews*, vol. 40, pp. 153–160, 2014.
- [24] M. Mobini, J.-C. Meyer, F. Trippe, T. Sowlati, M. Fröhling, and F. Schultmann, "Assessing the integration of torrefaction into wood pellet production," *Journal of Cleaner Production*, vol. 78, pp. 216–225, 2014.
- [25] S. Proskurina, E. Alakangas, J. Heinimö, M. Mikkilä, and E. Vakkilainen, "A survey analysis of the wood pellet industry in Finland: future perspectives," *Energy*, vol. 118, pp. 692–704, 2017.
- [26] B. Coelho, A. Oliveira, P. Schwarzbözl, and A. Mendes, "Biomass and central receiver system (CRS) hybridization: integration of syngas/biogas on the atmospheric air volumetric CRS heat recovery steam generator duct burner," *Renewable Energy*, vol. 75, pp. 665–674, 2015.
- [27] M. S. Roni, S. Chowdhury, S. Mamun, M. Marufuzzaman, W. Lein, and S. Johnson, "Biomass co-firing technology with policies, challenges, and opportunities: a global review," *Renewable and Sustainable Energy Reviews*, vol. 78, pp. 1089–1101, 2017.
- [28] E. Toklu, "Biomass energy potential and utilization in Turkey," *Renewable Energy*, vol. 107, pp. 235–244, 2017.
- [29] S. Proskurina, J. Heinimö, F. Schipfer, and E. Vakkilainen, "Biomass for industrial applications: the role of torrefaction," *Renewable Energy*, vol. 111, pp. 265–274, 2017.
- [30] M. M. O. Carvalho, M. Cardoso, and E. K. Vakkilainen, "Biomass gasification for natural gas substitution in iron ore pelletizing plants," *Renewable Energy*, vol. 81, pp. 566–577, 2015.
- [31] R. García, C. Pizarro, A. G. Lavín, and J. L. Bueno, "Biomass sources for thermal conversion. Techno-economical overview," *Fuel*, vol. 195, pp. 182–189, 2017.
- [32] C. M. S. D. Silva, A. D. C. O. Carneiro, B. R. Vital et al., "Biomass torrefaction for energy purposes—definitions and an overview of challenges and opportunities in Brazil," *Renewable and Sustainable Energy Reviews*, vol. 82, pp. 2426–2432, 2018.
- [33] Y. Xu, Y. Wang, Y. Chen et al., "Characterization of fine and carbonaceous particles emissions from pelletized biomass-coal blends combustion: implications on residential crop residue utilization in China," *Atmospheric Environment*, vol. 141, pp. 312–319, 2016.
- [34] J. Ahn and J. H. Jang, "Combustion characteristics of a 16 step grate-firing wood pellet boiler," *Renewable Energy*, vol. 129, pp. 678–685, 2018.
- [35] C. Ndibe, J. Maier, and G. Scheffknecht, "Combustion, cofiring and emissions characteristics of torrefied biomass in a drop tube reactor," *Biomass and Bioenergy*, vol. 79, pp. 105–115, 2015.
- [36] A. Kraszkievicz, A. Przywara, M. Kachel-Jakubowska, and E. Lorencowicz, "Combustion of plant biomass pellets on the grate of a low power boiler," *Agriculture and Agricultural Science Procedia*, vol. 7, pp. 131–138, 2015.
- [37] L. Chai and C. M. Saffron, "Comparing pelletization and torrefaction depots: optimization of depot capacity and biomass moisture to determine the minimum production cost," *Applied Energy*, vol. 163, pp. 387–395, 2016.
- [38] H. Chu, L. Xiang, X. Nie, Y. Ya, M. Gu, and E. Jiaqiang, "Laminar burning velocity and pollutant emissions of the gasoline components and its surrogate fuels: a review," *Fuel*, vol. 269, p. 117451, 2020.
- [39] G. Wu, D. Wu, Y. Li, and L. Meng, "Effect of acetone-n-butanol-ethanol (ABE) as an oxygenate on combustion, performance, and emission characteristics of a spark ignition engine," *Journal of Chemistry*, vol. 2020, Article ID 7468651, 11 pages, 2020.
- [40] Q. Zuo, Y. Xie, Q. Guan et al., "Performance enhancement of a gasoline dual-carrier catalytic converter of the gasoline engine in the reaction equilibrium process," *Energy Conversion and Management*, vol. 204, Article ID 112325, 2020.
- [41] Q. Zuo, Y. Xie, E. Jiaqiang et al., "Effect of different exhaust parameters on NO conversion efficiency enhancement of a dual-carrier catalytic converter in the gasoline engine," *Energy*, vol. 191, Article ID 116521, 2020.
- [42] Q. Zuo, Y. Tang, W. Chen, J. Zhang, L. Shi, and Y. Xie, "Effects of exhaust parameters on gasoline soot regeneration performance of a catalytic gasoline particulate filter in equilibrium state," *Fuel*, vol. 265, Article ID 117001, 2020.
- [43] E. Jiaqiang, M. Zhao, Q. Zuo et al., "Effects analysis on diesel soot continuous regeneration performance of a rotary microwave-assisted regeneration diesel particulate filter," *Fuel*, vol. 260, p. 116353, 2020.
- [44] K. Wei, Y. Yang, H. Zuo, and D. Zhong, "A review on ice detection technology and ice elimination technology for wind turbine," *Wind Energy*, vol. 23, no. 3, pp. 433–457, 2020.
- [45] B. Zhang, H. Zuo, Z. Huang, J. Tan, and Q. Zuo, "Endpoint forecast of different diesel-biodiesel soot filtration process in diesel particulate filters considering ash deposition," *Fuel*, vol. 271, Article ID 117678, 2020.
- [46] G. Liao, E. Jiaqiang, F. Zhang, J. Chen, and E. Leng, "Leng. Advanced exergy analysis for optimized ORC-based layout to recover waste heat of flue gas in coal-fired plants," *Applied Energy*, vol. 266, Article ID 114891, 2020.

Research Article

Experimental Study on Spray Characteristics of Gasoline/Hydrogenated Catalytic Biodiesel under GCI Conditions

Wenhua Yuan ¹, Jingjing Liao ¹, Bei Li,² and Wenjun Zhong²

¹Department of Mechanical and Energy Engineering, Shaoyang University, Shaoyang 422000, China

²School of Energy Power Engineering, Jiangsu University, Zhenjiang 212013, China

Correspondence should be addressed to Wenhua Yuan; ywh6308@163.com

Received 6 November 2019; Revised 7 January 2020; Accepted 4 February 2020; Published 11 May 2020

Guest Editor: Dezhi Zhou

Copyright © 2020 Wenhua Yuan et al. This is an open access article distributed under the Creative Commons Attribution License, which permits unrestricted use, distribution, and reproduction in any medium, provided the original work is properly cited.

The new blended fuel (gasoline/hydrogenated catalytic biodiesel) is expected to address the cold start problem under low temperature of gasoline compression ignition due to its excellent ignition performance. Additionally, its spray behavior as the combustion boundary condition could have a direct impact on the characteristics of subsequent combustion. Therefore, the objective of this study is to reveal the effects of hydrogenated catalytic biodiesel/gasoline on the spray characteristics under various ambient conditions. As a significant index of spray characteristics, the spray penetration was achieved by applying Mie scattering methods under nonevaporation and evaporation conditions on a constant volume combustion chamber. In addition, the experimental results were compared against the calculated values of the models. As demonstrated by the results, a better spray performance can be achieved by the blended fuel than diesel and hydrogenated catalytic biodiesel. In respect of spray penetration, there is almost no difference among the three fuels under the ambient temperature of 323 K. Nevertheless, the blended fuel is lower than that of hydrogenated catalytic biodiesel and diesel when the ambient temperature is 434 K and 523 K. Moreover, the blended fuel is the first to reach the stable state, and the hydrogenated catalytic biodiesel is earlier than diesel for the spray penetration. Meanwhile, the spray model is identified as suitable for the blended fuel.

1. Introduction

With the increasingly severe environmental problems and more stringent vehicle emission regulations, energy-efficient and low-emission internal combustion engines have attracted a great deal of attention in the most recent years. In order to achieve high efficiency and low emission for internal combustion engines, it has prompted many researchers to develop a variety of novel combustion modes such as homogeneous compression ignition (HCCI) [1, 2], premixed compression ignition (PCCI) [3, 4], partial premixed compression ignition (PPC) [5, 6], reactive controlled compression ignition (RCCI) [7], and gasoline compression ignition (GCI) [8, 9]. Especially, the GCI, as a direct injection compression ignition technology of gasoline in the cylinder, is able to control the formation of the mixed gas through the fuel injection strategy and to shape an appropriate mixture concentration stratification before ignition, thus exercising

control over ignition time and ignition phase. Compared with the conventional engine technologies, it took advantage of the high octane number and volatility of gasoline to achieve full mixing of fuel before ignition, which could achieve excellent combustion performance and low pollution emission [6, 10]. However, the excessively high octane number would cause difficulties in ignition at low load and high rate of pressure rise at high load. Therefore, it is possible to rely on fuel design to realize GCI combustion mode.

In recent years, plenty of research studies have been conducted on the GCI combustion. A success has been achieved in extending the GCI mode to idle condition with No. 87 antiexplosive gasoline by Kolodziej et al. [11]. Jia et al. [12] performed a study on the combustion emission characteristics of three different alternatives to gasoline fuels in compression ignition mode on a single-cylinder four-stroke diesel engine. As revealed by the results, TRFDIB fuel is an ideal gasoline alternative fuel. Ma et al. [13] investigated

the liquid-phase penetration and flame lift-off length and soot volume fraction distribution using gasoline/diesel fuel with different blending ratios. They determined that the increase of gasoline proportion in gasoline-diesel blends has shown suppression effect in emissions. The experiment was performed by Adams et al. [14] on a single-cylinder high-pressure common rail direct-injection light diesel engine with a compression ratio of 16.6 so as to explore the combustion and emission characteristics of soybean oil methyl ester biodiesel and RON87 gasoline blends under compression ignition mode. As indicated by the results, the ignition performance of gasoline could be affected by the addition of biodiesel with less volatility and higher cetane number. Meanwhile, the difficulty in ignition at low load can be reduced. For gasoline direct injection compression ignition, plenty of experimental studies have been performed [15, 16], which led to the discovery that the direct injection compression ignition of gasoline could achieve a high thermal efficiency while reducing the emission of NO_x and soot.

For GCI combustion mode, despite plenty of studies that have been conducted to evaluate the combustion emission characteristics of gasoline-diesel or biodiesel blends, the density difference between gasoline and diesel fuel remains significant, and the existence of miscible mixing stability problems restricts the development of gasoline direct injection combustion technology. Considering that HCB has different fuel properties compared to diesel such as high cetane number, low density, sulfur content, and no oxygen, it also possesses similar chemical structure to diesel. Therefore, in this paper, the experiment on the spray characteristic of gasoline/hydrogenated catalytic biodiesel mixture was conducted on constant volume based on the analysis conducted of the properties and spray combustion characteristics shown by hydrogenated catalytic biodiesel in the early stage of team.

It is well known that fuel spray and evaporation characteristics have an important effect on combustion process and final engine performance and emission. In this paper, the aim is to gain a further understanding of the mixing process of gasoline/hydrogenated catalytic biodiesel blend fuel and provide experimental evidence of the spray model. The spray characteristics between diesel, hydrogenated catalytic biodiesel, and gasoline/hydrogenated catalytic biodiesel blended fuels were compared and analyzed. Moreover, a detailed spray database was established for modeling validation to provide theoretical support for the application of blended fuel in engine combustion.

2. Experimental System and Test Conditions

2.1. Experimental Setup. A study on fuel sprays was performed in an optically visible constant volume combustion chamber, which was comprised of constant volume combustion chamber, high-pressure common rail fuel injection system, intake and exhaust system, data acquisition system, heating system, etc. The details can be attained in the previous research [17].

2.2. Experimental Methods. In the present study, the liquid phase was measured through the use of the Mie scattering imaging method under inert condition and with the help of the experimental apparatus as illustrated in Figure 1. As the source of lighting to visualize fuel spray, two white LEDs with a 140 W power were placed on both lateral windows, respectively. The high-speed digital camera was a Photron SA-Z with a vertical light source. The lens matching the phase machine was Nikon Micro-NIKKOR, the maximum aperture and focal length of which were 2.8 and 105 mm, respectively. Besides, the imaging speed was set to 40,000 fps with exposure time of 23.39 μ s, and the resolution was 512*1024. The details on the test method can be referenced in the previous study [18, 19].

2.3. Fuels and Test Matrix

2.3.1. Fuel Properties. In this paper, HCB was primarily obtained from waste cooking oil by applying the hydrodeoxygenation technology and the constituents of biodiesel were identified by conducting analysis with the assistance of gas chromatography-mass spectrometer (GC-MS). For the detailed result of hydrogenated catalytic biodiesel by GC-MS, one can refer to Shang et al. [20]. The main components of the biodiesel include n-pentadecane, n-hexadecane, and n-heptadecane with saturated alkane structure, accounting for 8.98%, 23.94%, and 47.38%, respectively. The fuel properties used in this study were supplied by Jiangsu Provincial Institute of Product Quality Supervision and Inspection and were compliant with GB/T20828-2015 and GB19147-2016 as the national standards. The full data are indicated in Table 1, which indicates that the fuel density, dynamic viscosity, and distillation of HCB are significantly lower when compared to pure diesel.

2.3.2. Test Matrix. In view of the previous research [21], this study mainly compared the spray characteristics of 70% gasoline and 30% hydrogenated catalytic biodiesel blend fuel (G70H30), hydrogenated catalytic biodiesel, and diesel oil, where "G" in G70H30 indicates gasoline, "H" denotes hydrogenated catalytic biodiesel, "D100" refers to diesel oil, and "HCB" stands for hydrogenated catalytic biodiesel, with the purpose of identifying whether gasoline/hydrogenated catalytic biodiesel blends can be used in gasoline compression combustion mode. The experimental conditions are presented in Table 2. The spray penetration of three kinds of fuels was analyzed comparatively under nonevaporation and evaporation conditions by changing the ambient temperature. Fuel injection was repeated for 10 times under each working condition for improvement to the reliability of the experimental results, and the interval time between each injection was set as 10 s.

2.4. Image Processing. Image processing represents a crucial part of the analysis of experimental data. In this study, the digital images captured by high-speed camera were processed by using MATLAB software. For the Mie scattering

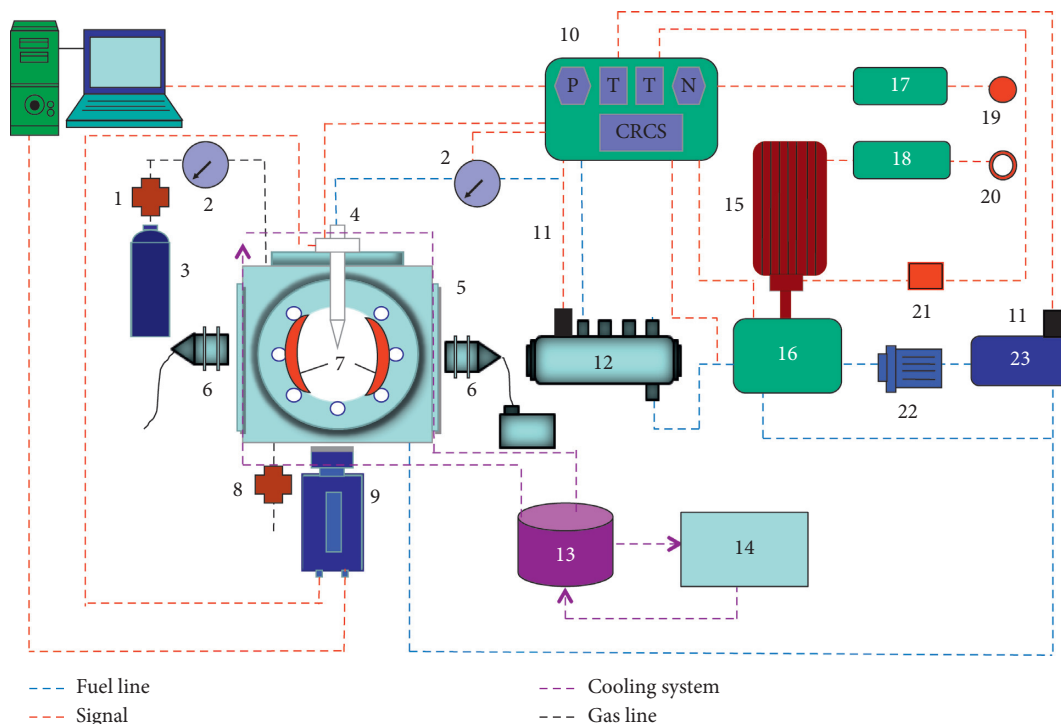


FIGURE 1: Schematic of Mie scatter (1, pressure reducing valve; 2, pressure meter; 3, nitrogen gas; 4, injector; 5, constant volume; 6, LED light source; 7, heating panels; 8, exhaust valve; 9, CCD camera; 10, high-pressure common rail system; 11, thermoelement; 12, common rail; 13, cooling water tank; 14, condenser; 15, electric motor; 16, high-pressure fuel pump; 17, switchboard; 18, transducer; 19, sensor switch; 20, potentiometric control unit; 21, speed sensor; 22, fuel filter; 23, fuel tank).

TABLE 1: Properties of experiment fuels.

Fuel properties	Diesel	HCB	Gasoline
Density (20°C) kg/m ³	832	791	762
Cetane number	49	103	14
Viscosity (40°C) mm ² /s	5.8	3.3	0.62
Oxygen content (m/m)	0	0	<2.7
Sulfur content (mg/kg)	<10	4.3	<10
Boiling point (10%)/°C	—	—	40
Boiling point (50%)/°C	300	303	111
Boiling point (90%)/°C	355	315	162
PAHs content (mg/mg) %	11	0	—
Low heating value (MJ/kg)	38	44	42.7

TABLE 2: Test matrix.

Parameters	Nonevaporation	Evaporation	
Ambient environment T_a (K)	323	423	523
Ambient pressure p_a (MPa)	5	5	5
Ambient density ρ_a (kg/m ³)	51.13	39.80	32.19
Injection pressure p_i (MPa)	100	100	100
Fuels	D100	HCB	D100

image, taking the background as the static, the average value of the first 18 images without fuel injection was taken as the background. Then, each image was removed from the background to get the spray area, and the 30% value of the peak gray value was treated as the threshold to generate a binary image. Subsequently, the spray profile was cleaned

using a filter, as shown in Figure 2. The distance between the injector tip to the farthest axial location of spray boundary was expressed as the spray penetration.

3. Results and Discussion

3.1. Spray Morphology and Spray Penetration. As shown in Figure 3, the influence that ambient temperature has on the tip penetration of the three fuels spray (D100, HCB, and G70H30) is exhibited under fuel injection pressure of 100 MPa and ambient density of 5 MPa. It can be seen from the figure that the three different fuels demonstrate similarly in penetration and dispersion behaviors with values of 323 K and 423 K. When the temperature rises to 523 K, the spray liquid phase of the G70H30 is shown to be shorter, which suggests that the mixed fuel has already undergone a substantial amount of fuel evaporation during this period. In addition, by comparing the spray at the proximal end of the nozzle with that at the lower end of the oil beam, a conclusion can be concluded that wrinkles and shedding disappear at the lower end of the spray oil beam, which is mainly attributed to the liquid fuel in the spray front area that undergoes the evaporation process from liquid to gas, thus leading to the loss of the spray liquid phase. On the other hand, the spray front will be turned into smaller particles with atomization, which would weaken the Mie scattering signal and result in the disappearance of folds.

In order for a deeper understanding as to the spray characteristics of the three fuels, a quantitative analysis was

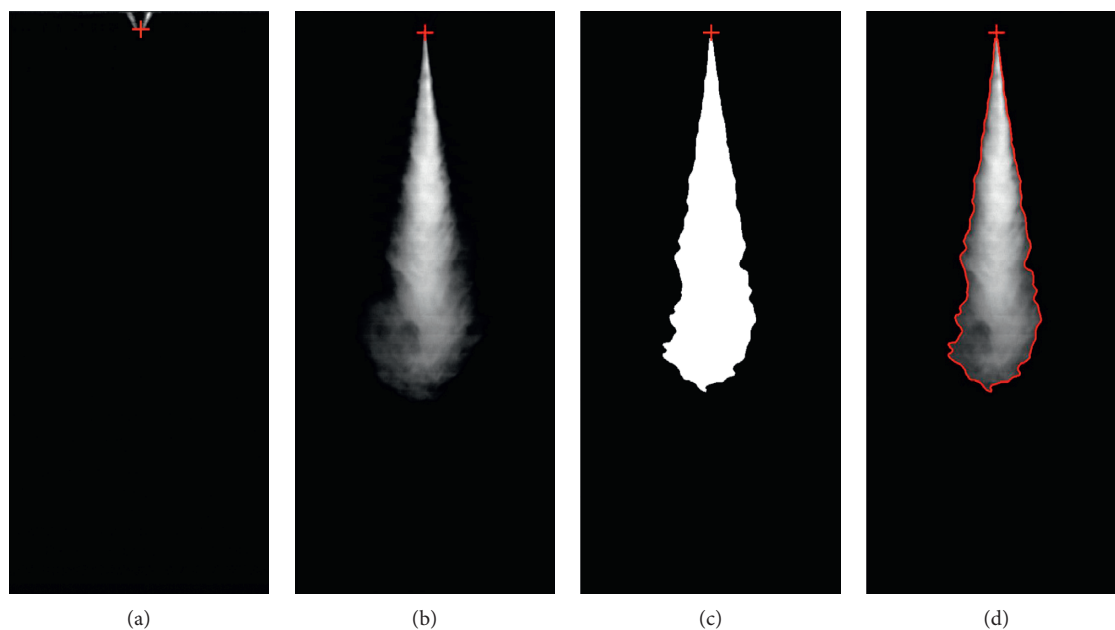


FIGURE 2: Image process for Mie scattering. (a) Average image for background. (b) Raw image subtracting background. (c) Binary image. (d) Filter image.

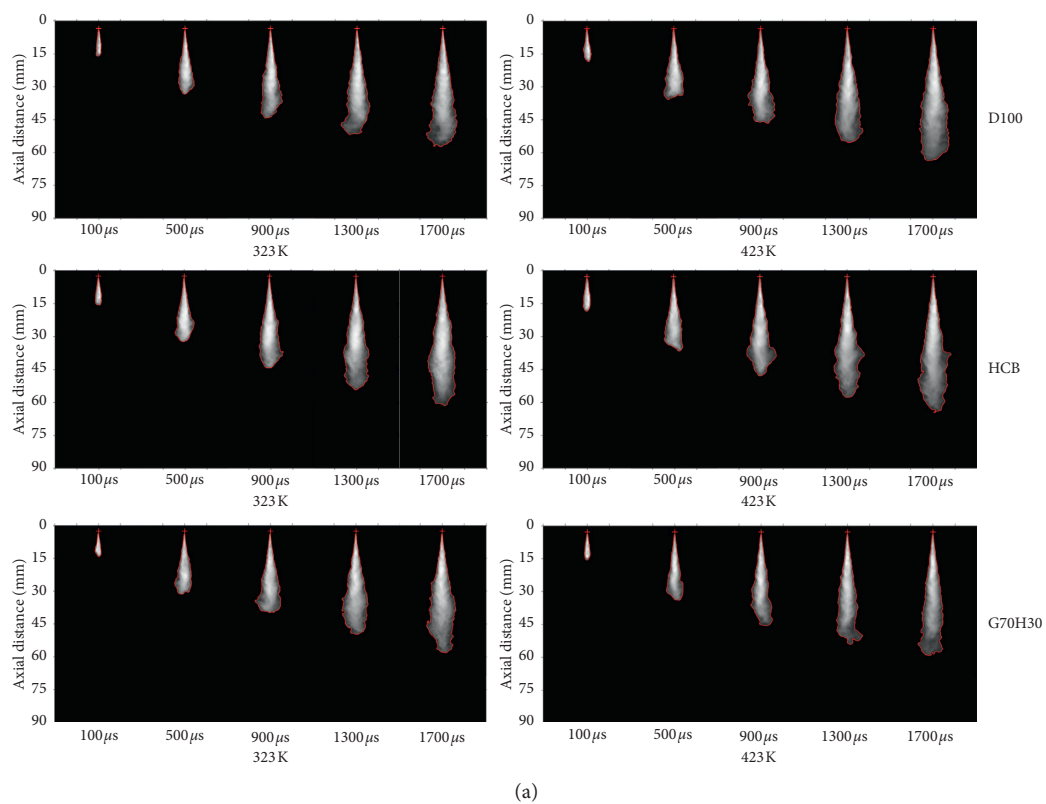


FIGURE 3: Continued.

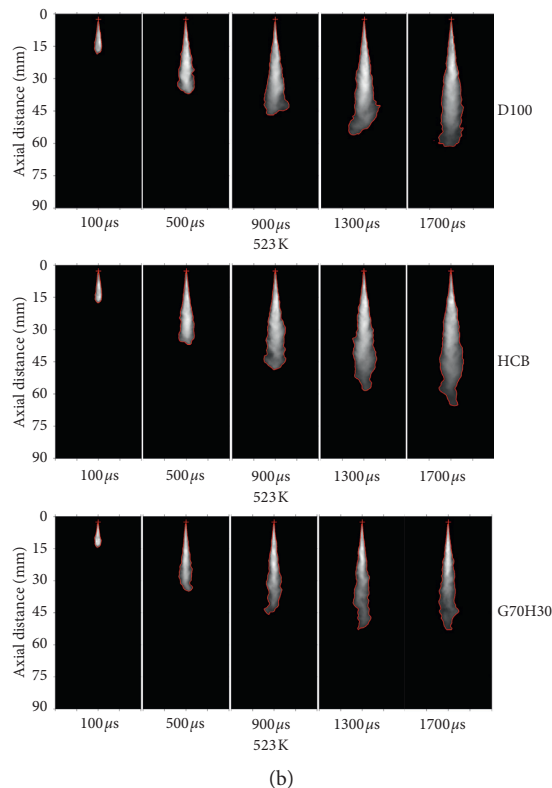


FIGURE 3: Liquid phase development versus time for D100, HCB, and G70H30 fuels under 323 K, 423 K, and 523 K.

conducted for the spray penetration for these fuels at varying ambient temperatures, as indicated in Figure 4. It can be discovered from the figures that there is a faster spray penetration of different fuels in advance of reaching a constant value and little fluctuation, which express a significant influence on the combustion efficiency of the diesel engine wall under the identical working conditions. At 323 K ambient temperature, with the fuels of D100, HCB, and G70H30, there is barely any difference between the spray penetration, and it basically increases over time. Gradually, the spray penetration reaches a certain stable value. Nevertheless, as the ambient temperature is on the rise, there is accordingly a more significant difference of stable value spotted between different fuels. When the ambient temperatures are 423 K and 523 K, respectively, the spray penetration of the three fuels are broadly the same at the first few hundred microseconds, suggesting that the fuel passes through the same path prior to their evaporation. Then, after the passing of a few hundred microseconds, at every ambient temperature, D100 results in a significantly higher spray penetration than the blends, with the values of HCB slightly greater than the mixed fuels.

As revealed by the fuel properties listed in Table 1, due to the lower density, viscosity, and surface tension of gasoline compared to the other two fuels and the higher volatility that leads to faster fuel droplets breaking and evaporation process, G70H30 demonstrates a better spray atomization behavior and a shorter spray penetration. Moreover, when the ambient temperature reaches 523 K, G70H30 is the first to

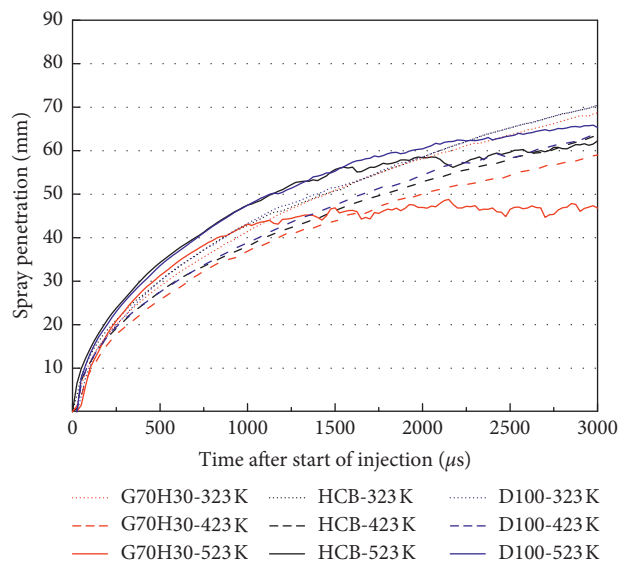


FIGURE 4: Liquid spray penetration versus time for D100, HCB, and G70H30 fuels under different ambient temperatures.

reach a stable state, followed by HCB and D100, respectively, which is closely related to fuel distillation. The higher distillation temperature is followed by the longer time it takes for fuel spray to reach a stable state.

Perfect spray penetration leads to better air-fuel mixing, while too long liquid length leads to fuel wall impingement on the cylinder, which may increase soot emission and

reduce engine efficiency. Therefore, compared with D100 and HCB, G70H30 demonstrates a more desirable spray characteristic, which is conducive to diesel engine gasoline compression ignition.

3.2. Spray Model. In order to follow up with the numerical calculation of spray combustion in gasoline compression ignition mode, the work of model verification was undertaken with consideration given to the experimental results, including model validation of the corresponding model equations under nonevaporation and evaporation conditions at three different temperatures.

3.2.1. Theoretical Model

(1) The Model under Nonevaporation. Plenty of research studies have provided the empirical expressions for the purpose of determining the spray characteristics of liquid jet depending on theoretical study and practical data on various oil fields [22]. As the spray has yet to be fully developed at this stage before the crushing, a peak occurs at the time when the spray starts to rupture. Hiroyasu and Arai [23] proposed a semiempirical formula for the variation of spray penetration over time under nonevaporation conditions combined with experimental data for two different regions before and after crushing.

$$S(t) = K_v \sqrt{\frac{\Delta P}{\rho_f}}, \quad 0 < t < t_{\text{break}}, \quad (1)$$

$$S(t) = K_p \sqrt{d_n} t \left(\frac{\Delta P}{\rho_a} \right)^{0.25}, \quad t > t_{\text{break}}, \quad (2)$$

$$t_{\text{break}} = \frac{K_{\text{bt}} \rho_f d_0}{(\rho_a \Delta P)^{0.5}}, \quad (3)$$

where ρ_f , ρ_a , d_0 , and ΔP are fuel and ambient gas densities, orifice diameter, and the difference between the fuel injection pressure and ambient pressure, respectively; t is the time after start of injection; and K_v , K_p , and K_{bt} are model constants. Specific values are exhibited in Table 3.

For the breaking time of three fuels, the dependent variables at three varieties of temperatures show broadly the same values. So, in this paper, 423 K is exemplified to obtain three fuel breaking times. In this paper, 423 K is exemplified to obtain three fuel breaking times, as indicated in Table 4. It can be observed in the table that Hiroyasu and Arai models differ greatly in respect of breaking time, and Arai models predict a shorter breaking time. In addition, the breaking time predicted by the two models shows that G70H30 is the shortest, followed by HCB, and D100 is the longest, which is largely attributed to the relationship between breakup time and fuel density.

(2) The Model under Evaporation. Based on the semiempirical formula suggested by Siebers [24], Desantes et al. [25] proposed a theoretical model in the terms of the conservation of momentum flux along the spray axis. Additionally,

TABLE 3: Model constants for spray tip penetration.

Model constants	Hiroyasu	Arai
K_v	0.39	0.60
K_p	2.95	3.36
K_{bt}	28.6	15.70

TABLE 4: Break time of experiment fuels.

Fuels	D100	HCB	G70H30
Orifice diameter (mm)	0.12	0.12	0.12
Ambient density (kg/m ³)	39.81	39.81	39.81
Injection pressure (MPa)	100	100	100
Ambient pressure (MPa)	5	5	5
Hiroyasu breaking time (μs)	46.51	44.22	43.06
Arai breaking time (μs)	14.35	13.64	13.29

as the spray penetration was clearly restricted by the geometry of the nozzle orifice as well as environmental and spray conditions, there is a necessity for the spray cone angle to be taken into account [26]. Therefore, based on the formula of Siebers, the spray penetration under evaporation conditions was calculated by applying the following model equation [27]:

$$S(t) \propto \left(\frac{\rho_f}{\rho_a} \right)^{1/4} u_0^{1/2} d_0^{1/2} t^{1/2} \tan \left(\frac{\theta}{2} \right)^{-1/2}, \quad (4)$$

$$u_0 = \frac{2(p_f - p_a)^{1/2}}{\rho_f}. \quad (5)$$

From equations (4) and (5), we can get (6) as model equation:

$$S(t) = \left(\frac{2(p_f - p_a)}{\rho_a} \right)^{1/4} d_0^{1/2} t^{1/2} \tan \left(\frac{\theta}{2} \right)^{-1/2}, \quad (6)$$

where ρ_f and ρ_a are fuel and ambient gas densities, respectively; d_0 is orifice diameter, t is time after start of injection; p_f and p_a are injection and ambient pressure, and θ is the spray angle.

3.2.2. Model Comparative Analysis. In this paper, the experimental data and the calculated values of the model were compared and analyzed by using formulas (2) and (6). Figure 5 shows the details on the comparison. It can be seen that the experimental statistics of D100 and HCB are consistent with the calculation results of model equation (1) under the nonevaporation situation. When G70H30 reaches 323 K, the experimental value coincides with that of the calculated from the model equation (1). Especially, at the temperature of 423 K, the experimental results conform well with the Hiroyasu model and model equation (1) only in the early stage of spray development, and the experimental value of the spray penetration is greater than estimated at the latter stage, which is speculated as associated with the low density and lower viscosity of gasoline.

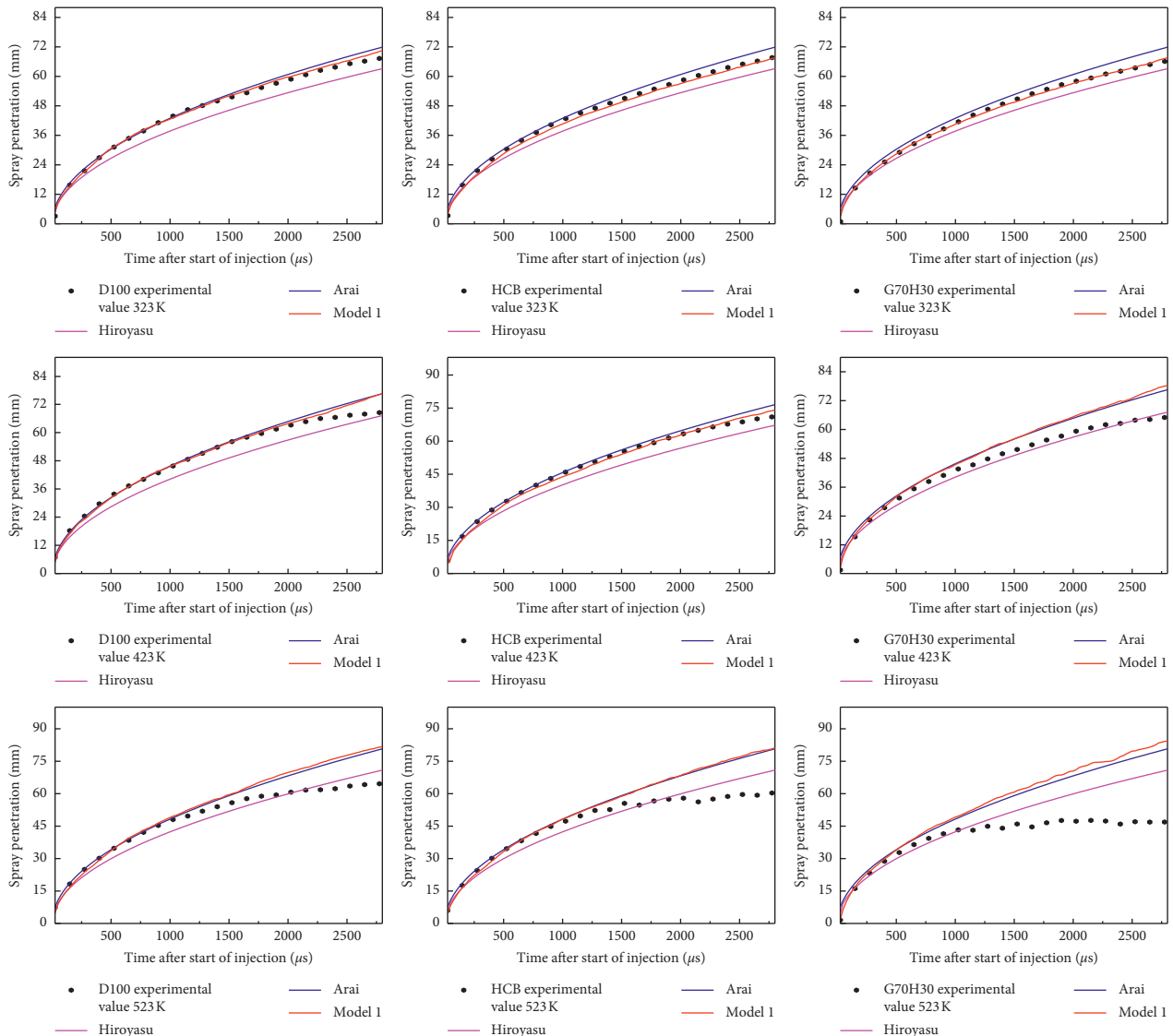


FIGURE 5: Comparison between experimental spray data and models for D100, HCB, and G70H30.

In the evaporation state, the experimental results of the three fuels in the early stage are in accordance with model 1, which is attributed to the spray penetration rate being faster than the evaporation rate. As a result of that, the difference of evaporation rate is yet to be reflected. Then, at the later stage, due to the different evaporation rates and faster evaporation rate than that of penetration, there is a difference of fitting, which suggests that the spray model is also applicable to the blended fuel G70H30. Moreover, in the nonevaporating state, the spray characteristics of three types of fuel can be predicted by applying model equation (1). In the late stage of evaporation, the evaporation model should be taken into consideration for analysis to improve the coincidence.

4. Conclusion

In this study, the Mie scattering technique was applied to study the spray characteristics of diesel, HCB, and G70H30 fuels under different ambient temperatures, the spray

structures and the spray penetration were mainly analyzed and compared, and the model calculation results were obtained to perform validation. The observations can be summarized as follows:

- (1) G70H30 has been successfully applied to the high-pressure common rail system, and the wall impingement phenomenon will not occur in a small-bore engine. Besides, compared with diesel and HCB, G70H30 shows similarity spray characteristics which reveal the blending fuel can be used in the compression ignition combustion model.
- (2) G70H30 is capable of achieving a superior spray performance compared to diesel and HCB and is applicable to compression ignition engine. Meanwhile, the atomization and evaporation are noticeably enhanced after the addition of gasoline, which is effective in facilitating the mixing of oil and gas, thus improving the combustion performance of the engine.

- (3) The spray model equation is also suitable for G70H30. Based on the comparative analysis of experimental data and model calculation values, despite the model constant of model equation (1) as obtained under evaporation conditions, it is also applicable to the spray characteristics of three fuels in nonevaporation state. As for evaporation state, allowing for the evaporation and penetration rate, the evaporation model ought to be considered for a further improvement to the calculation formula in the latter stage of spray.

Nomenclature

HCCI:	Homogeneous charge compression ignition
PCC:	Premixed charge compression ignition
PPC:	Partial premixed compression ignition
RCCI:	Reactive controlled compression ignition
GCI:	Gasoline compression ignition
HCB:	Hydrogenated catalytic biodiesel
G70H30:	70% gasoline and 30% hydrogenated catalytic biodiesel
D100:	Pure diesel
GB:	Gasoline/biodiesel blends
H10:	100% hydrogenated catalytic biodiesel
NO _x :	Nitrogen oxides
ρ_f :	Fuel density (kg/m ³)
ρ_a :	Ambient gas density (kg/m ³)
d_o :	Orifice diameter (mm)
Δp :	The difference between the fuel injection pressure and ambient pressure (MPa)
t :	The time after start of injection (μ s)
K_v, K_p :	Model constants
K_{bi} :	
p :	Ambient pressure (MPa)
p_f :	Injection pressure (MPa)
θ :	Spray angle (°)
Ta:	Ambient environment (K).

Data Availability

The data used to support the findings of this study are available from the corresponding author upon request.

Conflicts of Interest

The authors declare that they have no conflicts of interest.

Acknowledgments

This research was supported by the National Natural Science Foundation of China (no. 91541121) and the Postgraduate Innovative Research Project of Hunan Province (CX2018B814).

References

- [1] A. Uyumaz, "An experimental investigation into combustion and performance characteristics of an HCCI gasoline engine fueled with n-heptane, isopropanol and n-butanol fuel blends at different inlet air temperatures," *Energy Conversion and Management*, vol. 98, pp. 199–207, 2015.
- [2] B.-Q. He, J. Yuan, M.-B. Liu, and H. Zhao, "Combustion and emission characteristics of a n-butanol HCCI engine," *Fuel*, vol. 115, no. 1, pp. 758–764, 2014.
- [3] R. Kiplimo, E. Tomita, N. Kawahara, and S. Yokobe, "Effects of spray impingement, injection parameters, and EGR on the combustion and emission characteristics of a PCCI diesel engine," *Applied Thermal Engineering*, vol. 37, pp. 165–175, 2012.
- [4] A. J. Torregrosa, A. Broatch, A. García, and L. F. Mónico, "Sensitivity of combustion noise and NO_x and soot emissions to pilot injection in PCCI Diesel engines," *Applied Energy*, vol. 104, pp. 149–157, 2013.
- [5] Y. An, M. Jaasim, V. Raman et al., "Homogeneous charge compression ignition (HCCI) and partially premixed combustion (PPC) in compression Ignition engine with low octane gasoline," *Energy*, vol. 158, 2018.
- [6] D. Han, A. M. Ickes, S. V. Bohac, Z. Huang, and D. N. Assanis, "Premixed low-temperature combustion of blends of diesel and gasoline in a high speed compression ignition engine," *Proceedings of the Combustion Institute*, vol. 33, no. 2, pp. 3039–3046, 2011.
- [7] R. D. Reitz and G. Duraisamy, "Review of high efficiency and clean reactivity controlled compression ignition (RCCI) combustion in internal combustion engines," *Progress in Energy and Combustion Science*, vol. 46, pp. 12–71, 2015.
- [8] C. Kavuri, J. Paz, and S. L. Kokjohn, "A comparison of Reactivity Controlled Compression Ignition (RCCI) and Gasoline Compression Ignition (GCI) strategies at high load, low speed conditions," *Energy Conversion and Management*, vol. 127, pp. 324–341, 2016.
- [9] G. T. Kalghatgi, P. Risberg, and H. Ångström, "Partially premixed auto-ignition of gasoline to attain low smoke and low NO_x at high load in a compression ignition engine and comparison with a diesel fuel," in *Proceedings of theSAE Technical Paper Series*, January 2007.
- [10] M. Tuner, T. Johansson, H. Aulin et al., "Multi cylinder partially premixed combustion performance using commercial light-duty engine hardware," in *Proceedings of the SAE 2014 International Powertrain, Fuels & Lubricants Meeting*, October 2014.
- [11] C. Kolodziej, J. Kodavasal, S. Ciatti et al., "Achieving stable engine operation of gasoline compression ignition using 87 AKI gasoline down to idle," in *Proceedings of the SAE 2015 World Congress & Exhibition, SAE International, Detroit, Michigan, USA*, April 2015.
- [12] G. Jia, H. Wang, L. Tong, X. Wang, Z. Zheng, and M. Yao, "Experimental and numerical studies on three gasoline surrogates applied in gasoline compression ignition (GCI) mode," *Applied Energy*, vol. 192, pp. 59–70, 2017.
- [13] X. Ma, L. Zheng, Z. Wang, and J. Wang, "An optical study on liquid-phase penetration, flame lift-off location and soot volume fraction distribution of gasoline-diesel blends in a constant volume vessel," *Fuel*, vol. 139, pp. 365–373, 2015.
- [14] C. A. Adams, P. Loeper, R. Krieger, M. J. Andrie, and D. E. Foster, "Effects of biodiesel-gasoline blends on gasoline direct-injection compression ignition (GCI) combustion," *Fuel*, vol. 111, pp. 784–790, 2013.
- [15] A. J. Torregrosa, A. Broatch, R. Novella, J. Gomez-Soriano, and L. F. Mónico, "Impact of gasoline and Diesel blends on combustion noise and pollutant emissions in Premixed Charge Compression Ignition engines," *Energy*, vol. 137, pp. 58–68, 2017.
- [16] Y. Putrasari and O. Lim, "A study on combustion and emission of GCI engines fueled with gasoline-biodiesel blends," *Fuel*, vol. 189, pp. 141–154, 2017.

- [17] D. Li, Z. He, T. Xuan et al., "Simultaneous capture of liquid length of spray and flame lift-off length for second-generation biodiesel/diesel blended fuel in a constant volume combustion chamber," *Fuel*, vol. 189, pp. 260–269, 2017.
- [18] W. Zhong, P. Tamilselvan, Q. Wang et al., "Experimental study of spray characteristics of diesel/hydrogenated catalytic biodiesel blended fuels under inert and reacting conditions," *Energy*, vol. 153, pp. 349–358, 2018.
- [19] P. Tamilselvan, W. Zhong, T. Xuan et al., "Simultaneous study on spray liquid length, ignition and combustion characteristics of diesel and hydrogenated catalytic biodiesel in a constant volume combustion chamber," *Renewable Energy*, vol. 140, pp. 761–771, 2019.
- [20] W. Shang, Z. He, Q. Wang et al., "Experimental and analytical study on capture spray liquid penetration and combustion characteristics simultaneously with Hydrogenated Catalytic Biodiesel/Diesel blended fuel," *Applied Energy*, vol. 226, pp. 947–956, 2018.
- [21] W. Zhong, T. Pachiannan, Z. Li et al., "Combustion and emission characteristics of gasoline/hydrogenated catalytic biodiesel blends in gasoline compression ignition engines under different loads of double injection strategies," *Applied Energy*, vol. 251, p. 113296, 2019.
- [22] M. Xu, Y. Cui, and K. Deng, "One-dimensional model on liquid-phase fuel penetration in diesel sprays," *Journal of the Energy Institute*, vol. 89, no. 1, pp. 138–149, 2015.
- [23] H. Hiroyasu and M. Arai, "Structures of fuel sprays in diesel engines," in *Proceedings of the International Congress & Exposition, SAE Paper, Detroit, MI, USA*, February 1990.
- [24] D. L. Siebers, "Scaling liquid-phase fuel penetration in diesel sprays based on mixing-limited vaporization," in *Proceedings of the International Congress & Exposition, SAE Paper, Michigan, Detroit, USA*, March 1999.
- [25] J. M. Desantes, R. Payri, F. J. Salvador et al., "Development and validation of a theoretical model for diesel spray penetration," *Fuel*, vol. 85, no. 7-8, pp. 910–917, 2006.
- [26] F. Payri, J. V. Pastor, J. M. Pastor, and J. E. Juliá, "Diesel spray analysis by means of planar laser-induced exciplex fluorescence," *International Journal of Engine Research*, vol. 7, no. 1, pp. 77–89, 2006.
- [27] X. Wang, Z. Huang, O. A. Kuti, W. Zhang, and K. Nishida, "Experimental and analytical study on biodiesel and diesel spray characteristics under ultra-high injection pressure," *International Journal of Heat and Fluid Flow*, vol. 31, no. 4, pp. 659–666, 2010.

Research Article

Effects of Ethanol Blending on the Formation of Soot in *n*-Heptane/Air Coflow Diffusion Flame

Yuchen Ya,¹ Xiaokang Nie,¹ Licheng Peng,² Longkai Xiang,¹ Jialong Hu,¹ Wenlong Dong,¹ and Huaqiang Chu ¹

¹School of Energy and Environment, Anhui University of Technology, Ma'anshan 243002, Anhui, China

²College of Ecology and Environment, Hainan University, Haikou 570228, Hainan, China

Correspondence should be addressed to Huaqiang Chu; hqchust@163.com

Received 17 November 2019; Revised 20 January 2020; Accepted 29 January 2020; Published 26 March 2020

Guest Editor: Yaojie Tu

Copyright © 2020 Yuchen Ya et al. This is an open access article distributed under the Creative Commons Attribution License, which permits unrestricted use, distribution, and reproduction in any medium, provided the original work is properly cited.

Laminar diffusion flame was used to study the effect of ethanol on *n*-heptane flame in terms of the morphology and microstructure of soot under atomization combustion. For the same carbon mass flux at the outlet of the burner, the ratio of ethanol doping in *n*-heptane was changed, and the soot was collected from the axial positions of the flame at different heights using the thermophoresis probe method. The results showed that the flame height increased significantly with the increasing ratio of ethanol doping. When the ratio of ethanol and *n*-heptane (C_E/C_N) was 1.5, the flame height increased by 10 mm compared with that of pure *n*-heptane flame. Besides, the temperature in the center of the flame decreased with the increasing ratio of ethanol doping, but the temperature in the low position was higher than that in the pure *n*-heptane flame, and the temperature in the high position was lower than that in the pure *n*-heptane flame. However, the flame temperature was the highest when the proportion of ethanol in the mixture was greater than that of *n*-heptane. The temperature at the flame center decreased with the increasing ratio of ethanol doping, while the temperature at the flame edge increased with the ratio. The primary particle size of soot (soot size hereafter) in all working conditions increased with the increase of flame height, which was in line with the general growth law of soot. Moreover, the soot size at the same height decreased with the increasing ratio of ethanol doping, and this trend was most obvious at the flame height of 20 mm and 30 mm. Compared with pure *n*-heptane, when C_E/C_N was 1.5, the soot size at 20 mm and 30 mm decreased by an average of 34.83%, indicating that ethanol could inhibit the surface growth of soot particle. Furthermore, the density of soot particles collected by a single copper net decreased significantly, indicating that ethanol could reduce the production amount of soot.

1. Introduction

The problem of air pollution has plagued humans for many years. Currently, soot particles are generally considered to be the main cause of atmospheric particulate pollution. They usually come from incomplete combustion of hydrocarbon fuels, which can generate energy waste, resulting in global warming, environmental pollution, and diseases [1–4]. Thus, how to improve the fuel combustion efficiency and reduce the emission of pollutants is a hot issue. Alcohols, as the important liquid fuels, are composed of hydrocarbyl and hydroxyl (OH), which are readily available biomass liquid fuels in

industry, and it is known that the hydroxyl can promote the combustion process and reduce the emission of soot particle. Moreover, the high vaporization latent heat of alcohols can reduce the maximal combustion temperature and inhibit the formation of NO_x. Under such circumstances, methanol and ethanol are often used as fuel additives [5]. Extensive research has demonstrated that oxygen-containing fuel is an effective technique to reduce the carbon emission of diesel engine. For instance, ethanol has been successfully used in gasoline engines by blending with other fuels [6, 7]. Hamdam and Jubran [8] investigated the effect of ethanol addition on the gasoline combustion performance in engine. The results showed

that the optimal engine performance was reached when 5% ethanol was mixed with gasoline, and the fuel thermal efficiency was improved by 4% at low speed and 20% at high speed. Aharon et al. [9] conducted a weight reduction combustion experiment on droplet forming of *n*-heptane when being mixed with methanol or ethanol. They found that the combustion rate decreased dramatically with the increase of the initial droplet diameter in the air, and the effect of methanol and ethanol addition on combustion rate is not obvious. Moreover, Fan et al. [10] measured the ignition delay time of *n*-heptane/iso-octane/ethanol mixture and established a calculation model. Their results showed that the low temperature chemical inertness of ethanol extended the range of octane sensitivity. In the combustion process, the oxygen part of ethanol replaces O₂, and eventually the mole fraction of O₂ increases with the increasing ratio of ethanol [11]. Other studies demonstrated two ethanol/*n*-heptane mixture oxidation schemes through experiments and simulations [12] and modeled the chemical kinetics of the detailed scheme [13] and its simplified version [14].

In addition to the importance of increasing acetaldehyde yield through CH₃CHOH oxidation in ethanol/*n*-heptane mixtures of different proportions, a very similar oxidation pathway was found. Ergut et al. [15] investigated the generation of polycyclic aromatic hydrocarbons (PAHs) in ethylbenzene and ethanol flame at atmosphere pressure and pointed out that the generation rate of PAHs of ethanol was low even under lean oxygen combustion. Previous studies investigated the influence of ethanol doping ratio on the flame structure of *n*-heptane/ethanol and the formation rate of soot precursor [16]. It was found that the dehydrogenation rate of *n*-heptane was faster than that of ethanol, while ethanol promotes the reaction by providing active free radicals.

Oxygen-containing fuels with different structures would play different role in reducing soot emission, even in the same oxygen content [17]. Three methods are applied in the reduction of soot emission from alcohol: dilution, that is, reducing the aromatic hydrocarbon content of the fuel; oxygenation, through reducing the equivalence ratio and the number of carbon atoms that can be used to generate PAHs and soot; promotion of mixing effect, to lower the cetane number and prolong the stagnation period. It is an interesting finding that the presence of methanol and ethanol in ethylene diffusion flames had opposite effects on PAHs and soot formation in nonpremixed ethylene flame [18]. The dilution effect of methanol and the increased concentration of H₂ from the decomposition of methanol inhibit the formation of the initial benzene ring and the subsequent growth of PAHs and soot. On the contrary, the addition of a small amount of ethanol will promote the formation of soot. Zhang et al. [19] studied the effects of addition of dimethyl ether and ethanol on the formation of polycyclic aromatic hydrocarbons (PAHs) in premixed ethylene flame, and they found that C₂H₂ plays a key role in the formation of new aromatic rings. In addition, the nanostructure of soot particles is also a key to understand the properties of soot; not only is it related to the reactivity of soot [20] and the

aromatic structure characteristics of soot surface [21–25], but also it has a certain relationship with carbon nano-materials [26, 27].

Currently, there are quite limited studies regarding the effects of ethanol on the combustion flame of macromolecular hydrocarbon fuels, the growth process of soot in flames, and the change of soot morphology. The single component or mixture of *n*-heptane is often studied as an alternative to fuel oil [28]. The primary pyrolysis products of *n*-heptane are mainly methane, ethane, ethylene, propane, propylene, *n*-butane, 1-butene, 1-hexene, etc. [29]. With the increase of flame temperature, the secondary reaction of pyrolysis products increases, resulting in the increase of soot precursors and the final generation of a large amount of soot [30]. It is generally considered that cycloalkanes, cycloalkenes, and aromatic hydrocarbons are the main soot precursors [31]. The reaction becomes more complicated when ethanol is added, and this would change the groups of substances in the flame. Ethanol molecules contain hydroxyl groups, which are more likely to form active oxygen-containing intermediates during combustion, such as HCCO, CHO, and active OH radicals [32]. The increasing concentration of these components is beneficial to the reduction of the concentration of CH₃ and C₂H₂, for example, reducing the probability of the formation of PAHs through methylation cyclization and dehydrogenation plus acetylene and reducing the peak production of PAHs such as benzopyrene and naphthalene. Thus, soot particles cannot absorb more PAHs to form large diameter soot particles, which can inhibit the surface growth of soot, reduce the production of soot, promote the oxidation of basic carbon particles, and reduce the production of soot as well [33]. In this paper, the effects of ethanol on the change of soot particle size and nanostructure of *n*-heptane atomized flame and soot formation process were studied by mixing ethanol with *n*-heptane in different proportions.

2. Experimental Setup and Methods

The coaxial jet diffused flame experimental setup was used in this study, as shown in Figure 1, which mainly includes burner, flow control device, thermoprobe sampling system, and temperature detection system. In addition, liquid atomizer and insulation belt are also equipped for liquid fuel atomization. Glder burner is widely used for the study of hydrocarbon fuel coaxial jet diffusion flame. More details about the burner can be found in our previous works [34, 35].

The mixed fuel is vaporized through an evaporator, and a stable laminar diffusion flame is formed when the oxidizer (air) is 60 L/min. High purity (>99%) *n*-heptane and ethanol were used for experiments, which were bought from Shanghai Aladdin Biochemical Technology Co., Ltd. The well-mixed fuel passes through the liquid flow controller and then through the evaporator, which has a liquid inlet and a diluent gas inlet. With nitrogen being a carrier of liquid fuel, the liquid dispersed and diluted, and then the mixture would

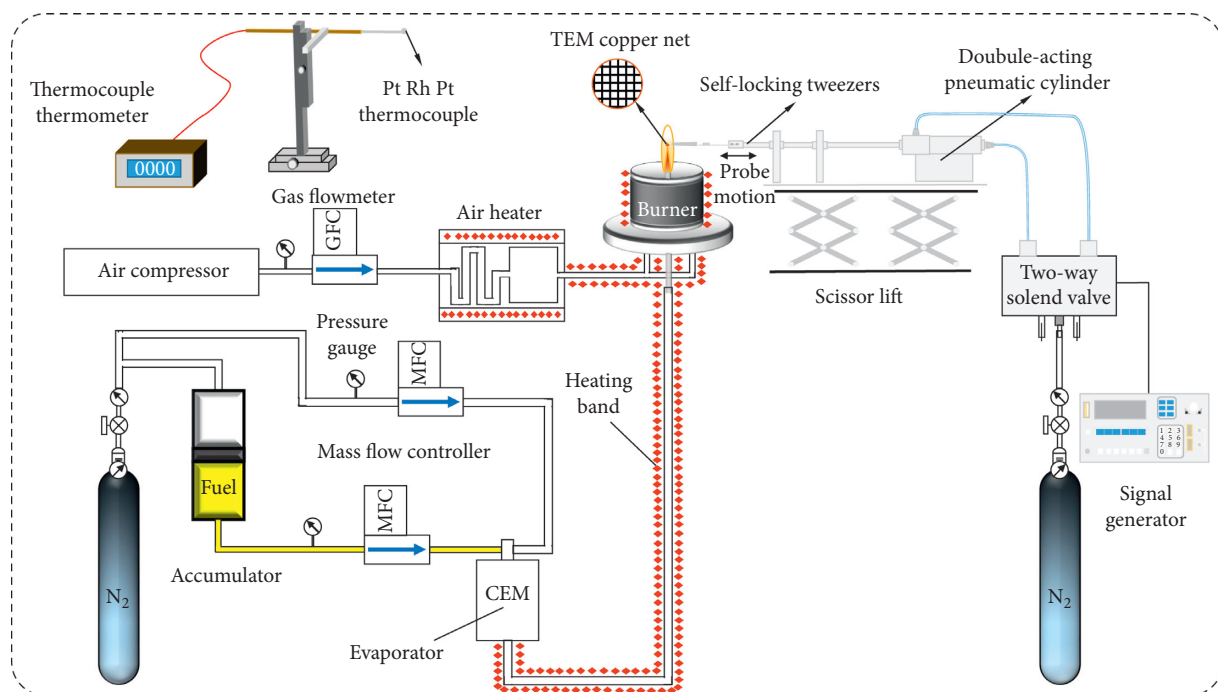


FIGURE 1: Schematic diagram of liquid fuel evaporative atomization combustion experiment system.

be vaporized in the evaporator. In this experiment, the evaporation temperature is 423.5 K, and the fuel is controlled by liquid flowmeter in the liquid atomizer. Finally, it passes through the insulated pipe, and then the laminar diffusion flame is formed in the nozzle. Besides, compressed dry air was used as the oxidizer (air) in this experiment.

In this paper, a CCD camera was used to record the shape of the flame. The soot samples were collected using a thermophoresis probe in the center of the flame, at different positions and heights. High resolution transmission electron microscopy (HRTEM, JEM-2100F) was used for detection, and the primary particle morphology and nanostructure of the soot were obtained by software statistics. The experimental conditions are shown in Table 1, ethanol and *n*-heptane mixed by volume fraction.

3. Results and Discussion

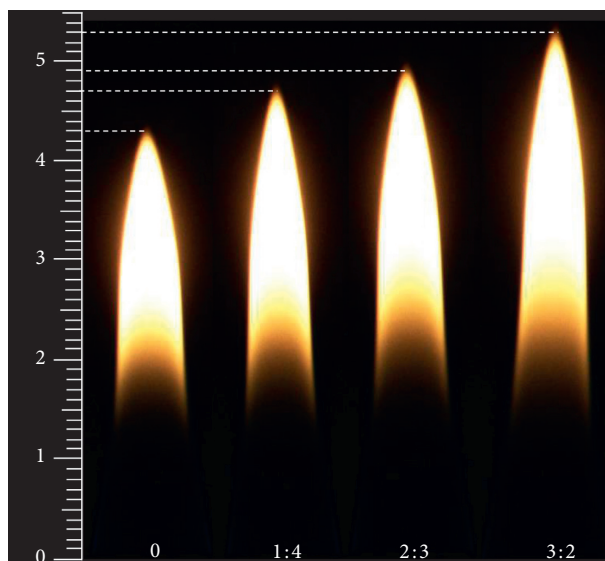
3.1. Comparison of Height for the Different Flames. The laminar diffusion flames of different ethanol addition on *n*-heptane are shown in Figure 2. The results showed that the flame extended distance in the air increased with the increasing proportion of ethanol in the fuel and mixed gas flow rate in the nozzle. For instance, the flame height increases with the increase of ethanol blending ratio, and the corresponding flame height reached up to 43 mm, 47 mm, 49 mm, and 53 mm when the ratio of C_E/C_N was maintained at 0, 1/4, 2/3, and 3/2, respectively. Additionally, the particle size of the droplet increases with the total liquid flow rate if a stable nitrogen flow rate is maintained; the combustion will require longer cracking time, and therefore, the combustion speed would be delayed. The results conform to the previous study [9].

The range of the low-temperature area (darker part) of the flame becomes wider with increasing ethanol doping ratio, and this may be attributed to the fact that the ethanol has high vaporization latent heat which can reduce the maximum combustion temperature. Since the hexadecane value of ethanol is low (8–10), mixing ethanol with *n*-heptane results in longer ignition delay and longer preparation time for ignition experience [36, 37]. Then, the fuel does not oxidized sufficiently at the initial position of the flame; while the cold zone widens in the flame, and the contour inside the flame becomes blurred through the flame image, and the edge between the low temperature area and the high temperature area becomes not obvious. This can be explained as follows. On the one hand, the increase in the amount of ethanol doping ratio requires that the pyrolysis of the fuel needs to absorb more heat and lower the temperature. On the other hand, the increase in the amount of ethanol doping ratio complicates the components in the flame. Ethanol pyrolysis and combustion increase the concentration of CH_2O , $\text{C}_2\text{H}_4\text{O}$, CO_2 , H_2O , HCCO , CHO , and active OH radicals in the flames [38]. Moreover, the specific heat capacity of CO_2 and H_2O is relatively large, and this would cause the decrease of temperature below the flame and result in insignificant heat radiation [39].

Figure 3 shows the temperature comparison diagram of different flames at different heights (high above the burner, HAB). The distribution of flame temperature distribution under different working conditions was measured using the three-dimensional thermocouple temperature measuring device. The temperature of flame center increases with flame height. The temperature at the same height of flame firstly increases and then decreases along the flame center to the edge. Furthermore, the temperature at the flame edge at the

TABLE 1: Experimental conditions under different equivalence ratios of ethanol/*n*-heptane.

Cases	Ethanol: <i>n</i> -heptane (C_E/C_N)	Liquid flow (mg/min)	Nitrogen gas flow (mL/min)	Flame height (mm)
Case 1	0:1	150	250	43
Case 2	1:4	175	250	47
Case 3	2:3	210	250	49
Case 4	3:2	260	250	53

FIGURE 2: Still pictures of *n*-heptane mixed with different amounts of ethanol.

same height increases moderately with the increase of ethanol doping ratio. There are three reasons accounting for this: (1) The *n*-hexadecane value of ethanol is much lower than that of *n*-heptane, and the fuel has a longer lag period, so the initial flame temperature at the lower and center of the flame will be lower than that of the pure *n*-heptane flame. (2) The latent heat of ethanol vaporization is high, and meanwhile ethanol vaporization will absorb more heat at the lower and center part of the flame, so the temperature of the flame center will be lower. At a higher and the edge position of the flame, the full combustion of the fuel makes the ethanol completely vaporized and the temperature of the flame increases consequently. (3) The blending of ethanol increases the oxygen concentration and the amount of CO_2 and H_2O , resulting in a higher temperature at the edge of the flame and a lower highest temperature.

3.2. Comparison of Soot in the Different Flames. Figure 4 shows the HRTEM image of pure heptane and $C_E/C_N = 1.5$ at the center of the flame at different heights, with a magnification of 4×10^4 times. At the initial stage of combustion (HAB = 20 mm), some single carbon nuclei appear in the pure *n*-heptane diffusion flame, and their number density is very low. Single carbon nuclei collided as flame height increased to HAB = 30 mm, the surface growth of soot particles intensified, and PAHs cluster condensation was observed [40]. The soot particles gradually become regular spherical,

the contour is clear, the particle size keeps increasing, and the flame height increases. The change in the particle size is mainly caused by the deposition and growth of PAHs on the surface of particles based on the dehydrogenation and carbonization mechanism, as well as the condensation and agglomeration between particles [41]. The carbonization degree of the soot particles was further strengthened with the increasing temperature in the flame center, and the particles continued to grow and condensate on the surface. Moreover, the oxidation was gradually strengthened, and the aggregates of particles in the soot increased, with an increase in overall size. At HAB = 40 mm, oxidation was further enhanced.

Under the action of Van der Waals force and Brownian force, the aggregates were further agglomerated to form chain shaped aggregate particles, the overall structure became loose, and the particle size of soot became smaller. Oxidation reaction exists in various development stages of nucleation, growth, coagulation, agglomeration, and oxidation of soot particles [42, 43]. In the lower position of the flame, the diffusion effect of oxygen is weak, and the surface growth of the soot particles is dominant, with increasing amount and size of soot particles. Furthermore, oxidation reaction gradually becomes the dominant factor with the continuous rise of the flame height, and the diameter of the soot particles gradually decreases. Near the flame tip, the oxidation reaction is very intense due to the high temperature in the flame center, and then the soot agglomerates would be quickly depleted and consumed accordingly. The

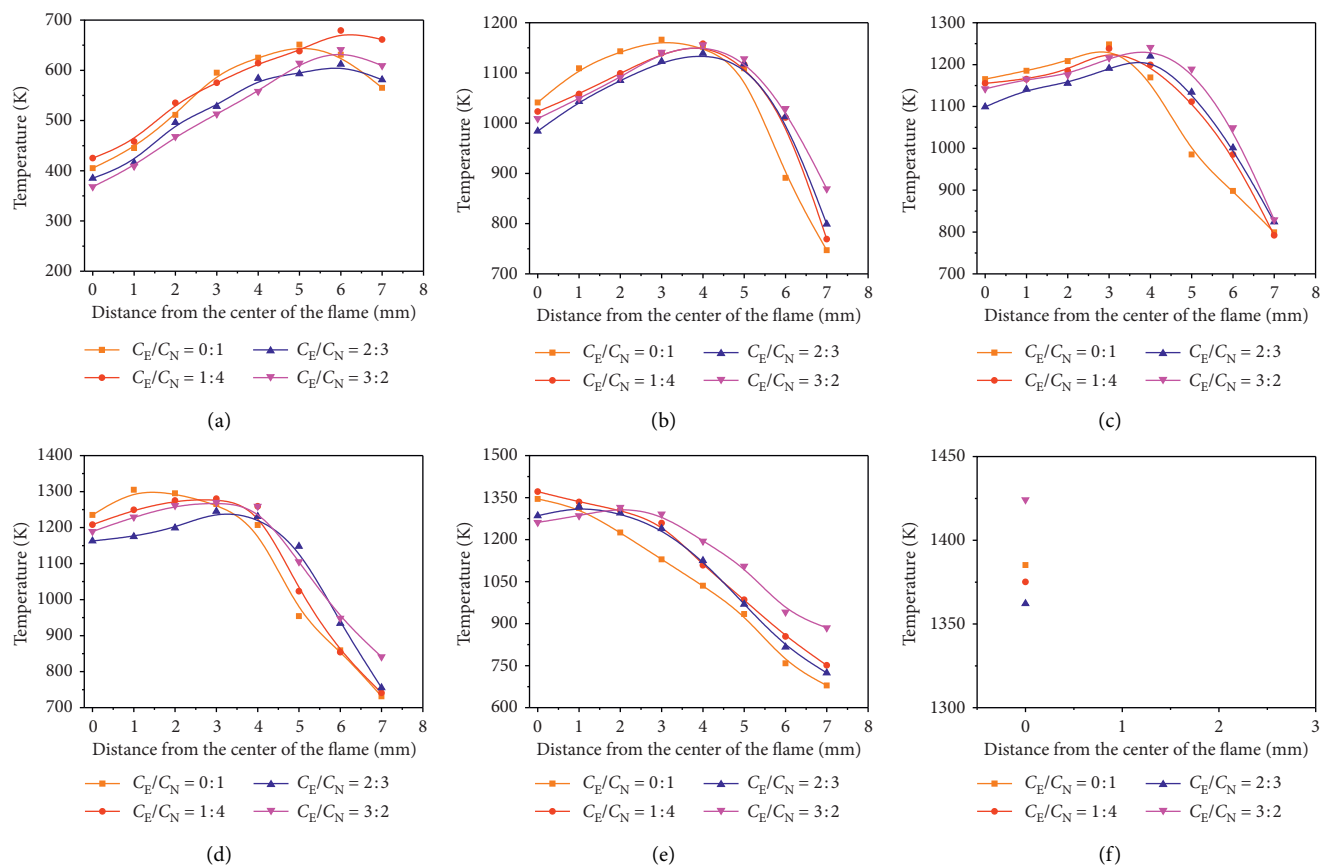


FIGURE 3: Temperature distribution of flame under different experimental conditions at the same height. (a) $HAB = 0$ cm. (b) $HAB = 1$ cm. (c) $HAB = 2$ cm. (d) $HAB = 3$ cm. (e) $HAB = 4$ cm. (f) Highest flame position.

fitting results indicated that the size of soot particles at different heights meets normal distribution, which was similar to the soot size range (e.g. 10~40 nm) of *n*-heptane in the previous studies [44, 45].

The growth process of soot along the axial height at the center of the diffused flame when C_E/C_N is 1/4 and 2/3, respectively, as shown in Figure 5, which is similar to pure *n*-heptane ($C_E/C_N = 0$). In other words, the development of soot particles has gone through five stages of nucleation, growth, condensation, agglomeration, and oxidation. The difference is that with the addition of ethanol, the surface of the soot at the same height growth is inhibited, the soot size becomes smaller, the agglomeration is delayed, and the oxidation reaction is advanced. Thus, the distribution of the initial soot particles in the sampled copper net at the lower position of the flame disperses. In other words, the gas-phase reaction area generated by soot in the flame is expanded, and the particle agglomeration oxidation area is decreased.

3.3. Analysis of the Distribution of Soot Sizes. The HRTEM images of soot particles in a laminar diffusion flame of *n*-heptane blended with ethanol are shown in Figure 6. The size of primary soot particles was measured using nanometer

analysis software. Various images were taken at various flame heights for statistical calculation. The number of statistical particles was about 100, and the particle diameter distribution was nonlinearly fitted using LogNormal. Figure 7 gave the soot size under experimental conditions.

According to the statistical results of particle size, the soot size increases with the flame height. The soot particles varied dramatically with the flame height; e.g., HAB values of 20 mm, 30 mm, and 40 mm are given in Table 2. It can be seen that the soot size has a good regularity with the blending ratio of ethanol; i.e., the particle size obviously decreases with the ethanol doping ratio, except for $C_E/C_N = 0$ at $HAB = 40$ mm. The reason may be that the soot particles at the tip of the pure *n*-heptane flame were oxidized, resulting in a smaller particle size.

Compared with the soot size at $C_E/C_N = 0$ and $C_E/C_N = 3/2$, the flame height at $HAB = 20$ mm and $HAB = 30$ mm decreases by 33.16% and 36.47%. The trend was not obvious at $HAB = 40$ mm, and the soot size in the pure *n*-heptane flame was smaller than that in the flame with ethanol. This may be explained as follows: The soot particles matured along the radial position of the flame and were finally oxidized at the flame edge and tip with higher temperature. However, the blending of ethanol will

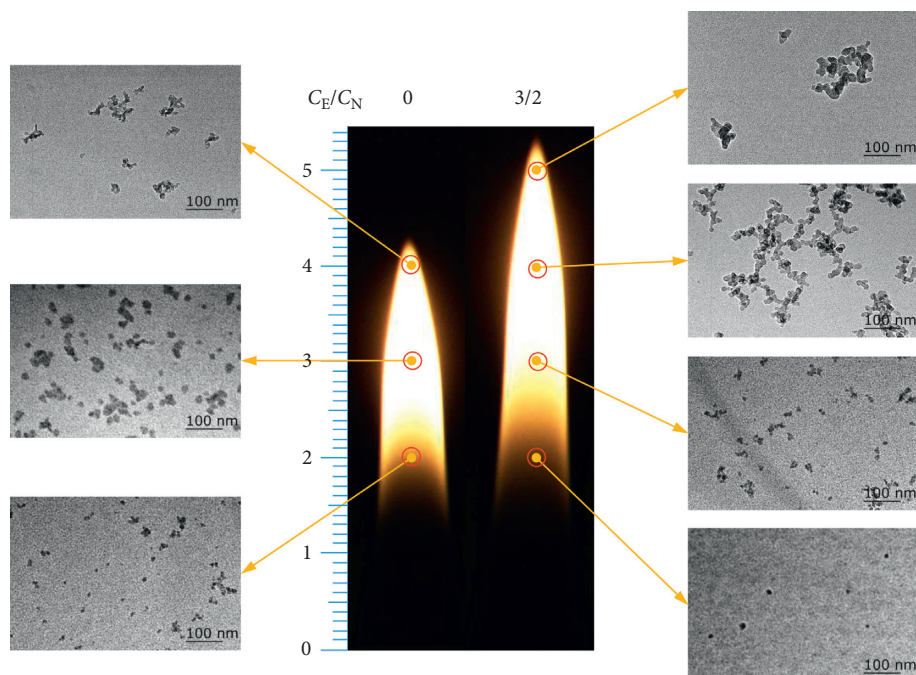


FIGURE 4: Comparison of soot morphology evolution of pure *n*-heptane and $C_E/C_N = 1.5$ in the laminar diffusion flame.

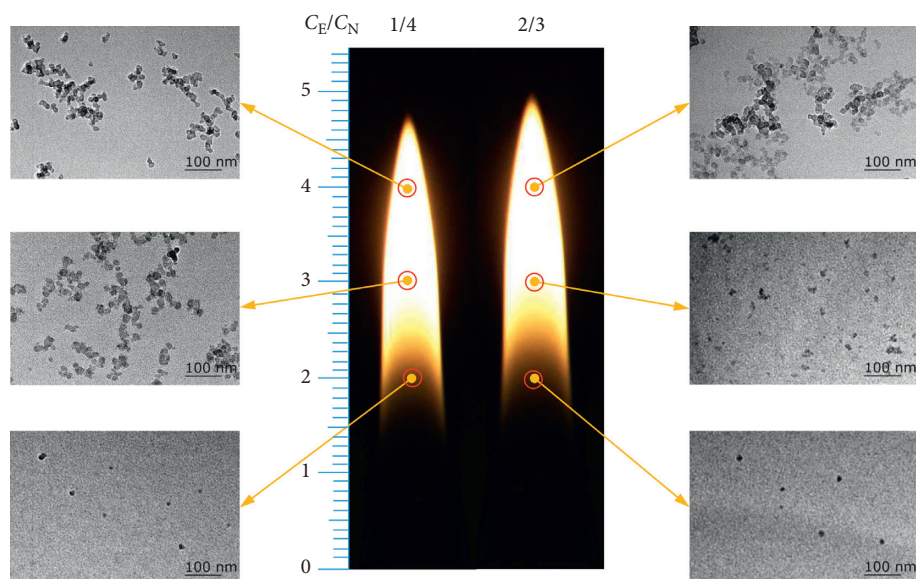


FIGURE 5: Comparison of soot morphology evolution of $C_E/C_N = 1/4$ and $2/3$ in the laminar diffusion flame.

increase the flame height and decrease the maximum flame temperature, thus delaying the oxidation of soot. On the whole, the mechanism explaining the fact that soot particles decrease with the blending of ethanol is that ethanol molecules contain hydroxyl groups while ethanol contains 34.8% oxygen. Thus, some oxygen-containing intermediate radicals may be evolved in the combustion, which further promoted the oxidation of basic carbon particles. In addition, particle size is also affected by fuel and the flow rate of oxidizer, since the change in their initial velocity will affect the combustion reaction and the time of the soot particles staying in the flame [16]. Increasing the velocity of the oxidizer can

suppress the energy transfer from the annular region producing soot to the flame axis. As the initial air velocity increases, it takes longer for soot to form at the flame axis, and the particle size of soot decreases with the increase of oxidizer velocity, which is the result of coagulation, surface growth reaction, and shorter residence time of fuel pyrolysis products [46]. As the increasing ratio of ethanol doping, the effects of ethanol on fuel dilution, oxidation, retardation of combustion period, and radiation of decomposition products would be enhanced, the size of the basic carbon particles moves toward the small particle diameter direction, and therefore the distribution range becomes narrow.

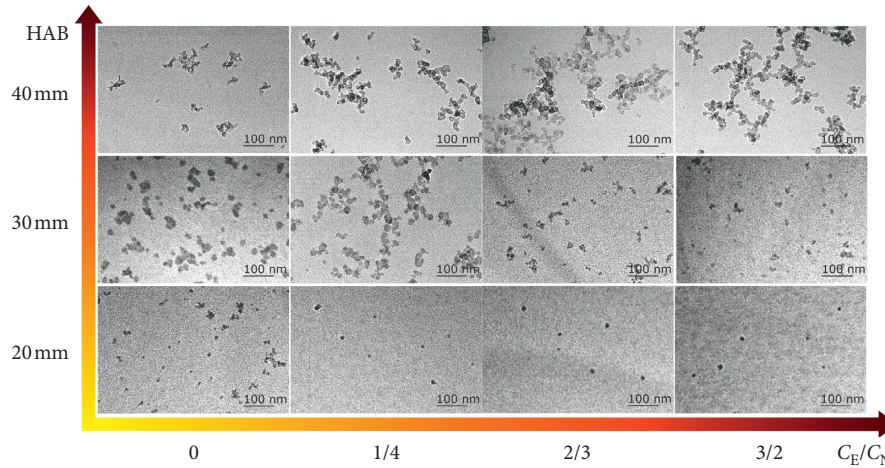


FIGURE 6: HRTEM image of soot particles in a laminar diffusion flame with *n*-heptane mixed with ethanol.

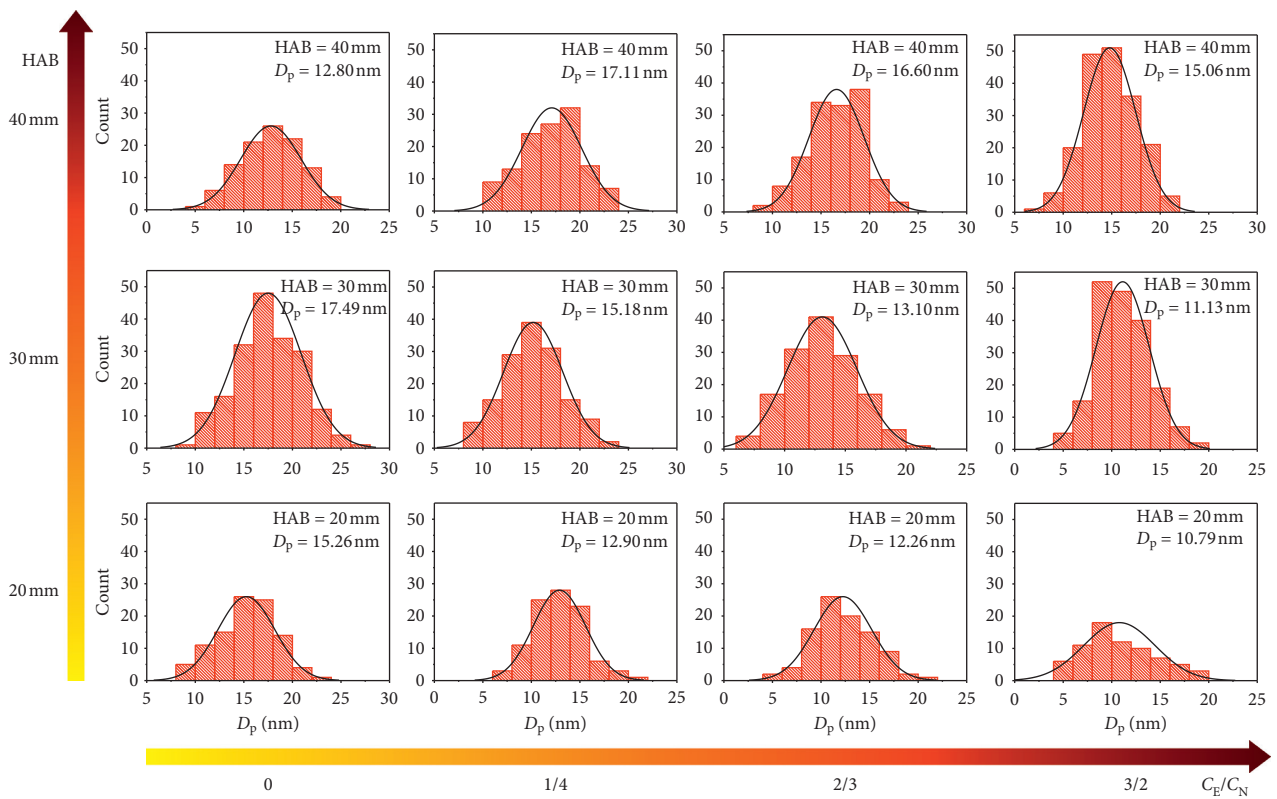


FIGURE 7: Statistical results of soot particle size in a laminar diffusion flame with *n*-heptane mixed with ethanol.

TABLE 2: The average particle size of the primary soot at different heights.

HAB (mm)	C_E/C_N			
	0	1/4	2/3	3/2
20	15.26 nm	12.9 nm	12.26 nm	10.79 nm
30	17.49 nm	15.18 nm	13.1 nm	11.13 nm
40	12.8 nm	17.11 nm	16.6 nm	15.06 nm

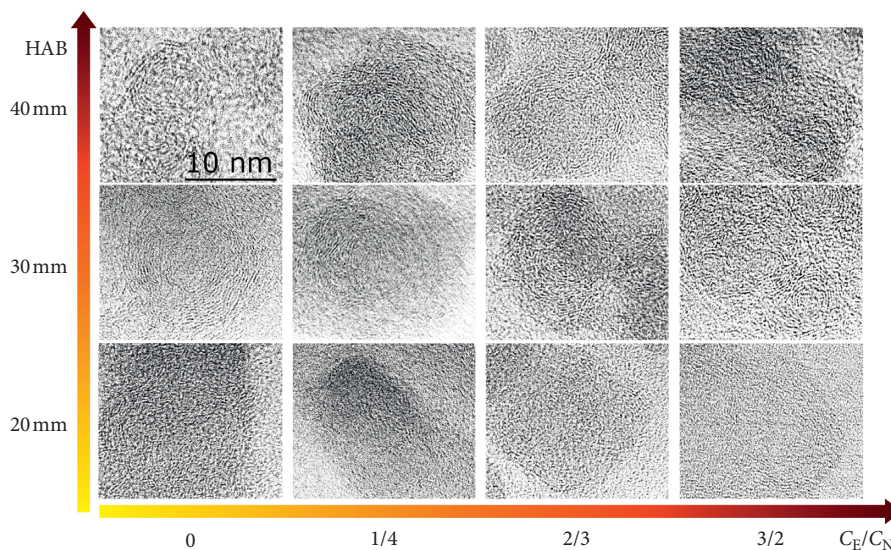


FIGURE 8: Nanostructure of soot particle in laminar coflow diffusion flames with *n*-heptane mixed with ethanol.

Figure 8 shows HRTEM images of soot magnified by 4×10^5 times along the center of flame at different heights in the ethanol/*n*-heptane flames. From Figure 8, it can be found that the shell structure of soot becomes obvious with the increase of flame height. The addition of ethanol can reduce the aging degree of soot and increase the soot oxidation activity in the high temperature area of the flame (edge and tip location), as the results in [18–20].

4. Conclusions

In this study, the morphological evolution and nanostructure of soot emission in coflow laminar diffusion flames of *n*-heptane blended with ethanol were experimentally studied using thermal swimming probe sampling and HRTEM technology. The main conclusions are as follows:

- (1) Under the condition of the same total carbon content, the height of *n*-heptane increased with the increasing ratio of ethanol.
- (2) The temperature of the flame center position decreased with the ratio of ethanol blended, while it increased with the ratio at flame edge.
- (3) The formation process of soot particles in laminar diffusion flame of *n*-heptane and *n*-heptane/ethanol is similar. However, the soot size at the same height decreases significantly as ethanol increases in the mixed fuels.

Data Availability

All data used to support the findings of this study are included within the article.

Conflicts of Interest

The authors declare that there are no conflicts of interest regarding the publication of this paper.

Acknowledgments

The authors would like to thank the National Natural Science Foundation of China (Grant Nos. 5187827808 and 51676002), Project of Support Program for Outstanding Young People in Colleges and Universities (Grant No. gxyqZD201830) and National Training Program of Innovation and Entrepreneurship for Undergraduates (Grant No. 201910360082) for their financial support of this study.

References

- [1] A. P. Rutter, D. C. Snyder, J. J. Schauer, J. DeMinter, and B. Shelton, "Sensitivity and bias of molecular marker-based aerosol source apportionment models to small contributions of coal combustion soot," *Environmental Science & Technology*, vol. 43, no. 20, pp. 7770–7777, 2009.
- [2] L. A. Sgro, A. Simonelli, L. Pasarella et al., "Toxicological properties of nanoparticles of organic compounds (NOC) from flames and vehicle exhausts," *Environmental Science & Technology*, vol. 43, no. 7, pp. 2608–2613, 2009.
- [3] Z. Lu, D. G. Streets, E. Winijkul et al., "Light absorption properties and radiative effects of primary organic aerosol emissions," *Environmental Science & Technology*, vol. 49, no. 8, pp. 4868–4877, 2015.
- [4] M. Brauer, G. Hoek, H. A. Smit et al., "Air pollution and development of asthma, allergy and infections in a birth cohort," *European Respiratory Journal*, vol. 29, no. 5, pp. 879–888, 2007.
- [5] R. Lemaire, E. Therssen, and P. Desgroux, "Effect of ethanol addition in gasoline and gasoline-surrogate on soot formation in turbulent spray flames," *Fuel*, vol. 89, no. 12, pp. 3952–3959, 2010.
- [6] S. M. Sarathy, P. Oßwald, N. Hansen, and K. Kohse-Höinghaus, "Alcohol combustion chemistry," *Progress in Energy and Combustion Science*, vol. 44, pp. 40–102, 2014.
- [7] C. Jin, M. Yao, H. Liu, F. Chia-fon, and J. Ji, "Progress in the production and application of *n*-butanol as a biofuel," *Renewable and Sustainable Energy Reviews*, vol. 15, no. 8, pp. 4080–4106, 2018.

- [8] M. Hamdan and B. Jubran, "The effect of ethanol addition on the performance of diesel and gasoline engines," *Dirarst*, vol. 13, no. 10, pp. 229–244, 1985.
- [9] I. Aharon, V. Tam, and B. Shaw, "Combustion of submillimeter heptane/methanol and heptane/ethanol droplets in reduced gravity," *Journal of Combustion*, vol. 2013, Article ID 154202, 6 pages, 2013.
- [10] Q. Fan, Z. Wang, Y. Qi, and Y. Wang, "Investigating auto-ignition behavior of *n*-heptane/iso-octane/ethanol mixtures for gasoline surrogates through rapid compression machine measurement and chemical kinetics analysis," *Fuel*, vol. 241, pp. 1095–1108, 2019.
- [11] M. D. Li, Z. Wang, Y. Zhao, R. N. Li, and S. Liu, "Experiment study on major and intermediate species of ethanol/*n*-heptane premixed flames," *Combustion Science and Technology*, vol. 185, no. 12, pp. 1786–1798, 2013.
- [12] P. Dagaut and C. Togbé, "Experimental and modeling study of the kinetics of oxidation of ethanol-*n*-heptane mixtures in a jet-stirred reactor," *Fuel*, vol. 89, no. 2, pp. 280–286, 2010.
- [13] H. J. Curran, P. Gaffuri, W. J. Pitz, and C. K. Westbrook, "A comprehensive modeling study of *n*-heptane oxidation," *Combustion and Flame*, vol. 114, no. 1-2, pp. 149–177, 1998.
- [14] R. Seiser, H. Pitsch, K. Seshadri, W. J. Pitz, and H. J. Curran, "Extinction and autoignition of *n*-heptane in counterflow configuration," *Proceedings of the Combustion Institute*, vol. 28, no. 2, pp. 2029–2037, 2000.
- [15] A. Ergut, S. Granata, J. Jordan et al., "PAH formation in one-dimensional premixed fuel-rich atmospheric pressure ethylbenzene and ethyl alcohol flames," *Combustion and Flame*, vol. 144, no. 4, pp. 757–772, 2006.
- [16] R. Li, Z. Liu, Y. Han et al., "Investigation into the influence of the ethanol concentration on the flame structure and soot precursor formation of the *n*-heptane/ethanol premixed laminar flame," *Energy & Fuels*, vol. 32, no. 4, pp. 4732–4746, 2018.
- [17] T. C. Zannis and D. T. Hountalas, "DI diesel engine performance and emissions from the oxygen enrichment of fuels with various aromatic content," *Energy & Fuels*, vol. 18, no. 3, pp. 659–666, 2004.
- [18] F. Yan, L. Xu, Y. Wang, S. Park, S. M. Sarathy, and S. H. Chung, "On the opposing effects of methanol and ethanol addition on PAH and soot formation in ethylene counterflow diffusion flames," *Combustion and Flame*, vol. 202, pp. 228–242, 2019.
- [19] Y. Zhang, Y. Li, P. Liu, R. Zhan, Z. Huang, and H. Lin, "Investigation on the chemical effects of dimethyl ether and ethanol additions on PAH formation in laminar premixed ethylene flames," *Fuel*, vol. 256, p. 115809, 2019.
- [20] J. H. Stephen and M. W. Anita, "Chemical kinetics of soot particle growth," *Annual Review of Physical Chemistry*, vol. 36, no. 1, pp. 31–52, 1985.
- [21] M. L. Botero, D. Chen, S. González-Calera, D. Jefferson, and M. Kraft, "HRTEM evaluation of soot particles produced by the non-premixed combustion of liquid fuels," *Carbon*, vol. 96, pp. 459–473, 2016.
- [22] Y. Ying and D. Liu, "Effects of butanol isomers additions on soot nanostructure and reactivity in normal and inverse ethylene diffusion flames," *Fuel*, vol. 205, pp. 109–129, 2017.
- [23] Y. Ying and D. Liu, "Nanostructure evolution and reactivity of nascent soot from inverse diffusion flames in CO₂, N₂, and He atmospheres," *Carbon*, vol. 139, pp. 172–180, 2018.
- [24] J. Duan, Y. Ying, and D. Liu, "Novel nanoscale control on soot formation by local CO₂ micro-injection in ethylene inverse diffusion flames," *Energy*, vol. 179, pp. 697–708, 2019.
- [25] Y. Ying and D. Liu, "Effects of water addition on soot properties in ethylene inverse diffusion flames," *Fuel*, vol. 247, pp. 187–197, 2019.
- [26] N. K. Memon, S. D. Tse, J. F. Al-Sharab et al., "Flame synthesis of graphene films in open environments," *Carbon*, vol. 49, no. 15, pp. 5064–5070, 2011.
- [27] P. Minutolo, M. Commodo, A. Santamaria, G. De Falco, and A. D'Anna, "Characterization of flame-generated 2-D carbon nano-disks," *Carbon*, vol. 68, pp. 138–148, 2014.
- [28] G. Vishwanathan and R. D. Reitz, "Application of a semi-detailed soot modeling approach for conventional and low temperature diesel combustion-part I: model performance," *Fuel*, vol. 139, pp. 757–770, 2015.
- [29] P. Lindstedt and L. Maurice, "Detailed kinetic modelling of *n*-heptane combustion," *Combustion Science & Technology*, vol. 107, no. 4–6, pp. 317–353, 1995.
- [30] D. Zhou, W. Yang, J. Li, and K. L. Tay, "Simplified fuel cracking process in reduced mechanism development: PRF-PAH kinetic models for combustion and soot prediction," *Fuel*, vol. 182, pp. 831–841, 2016.
- [31] H. Wang, R. Deneys Reitz, M. Yao, B. Yang, Q. Jiao, and L. Qiu, "Development of an *n*-heptane-*n*-butanol-PAH mechanism and its application for combustion and soot prediction," *Combustion and Flame*, vol. 160, no. 3, pp. 504–519, 2013.
- [32] N. M. Marinov, "A detailed chemical kinetic model for high temperature ethanol oxidation," *International Journal of Chemical Kinetics*, vol. 31, no. 3, pp. 183–220, 2015.
- [33] A. Frassoldati, A. Cuoci, T. Faravelli, and E. Rani, "Kinetic modeling of the oxidation of ethanol and gasoline surrogate mixtures," *Combustion Science & Technology*, vol. 182, no. 4–6, pp. 653–667, 2010.
- [34] H. Chu, W. Han, W. Cao, M. Gu, and G. Xu, "Effect of methane addition to ethylene on the morphology and size distribution of soot in a laminar co-flow diffusion flame," *Energy*, vol. 166, pp. 392–400, 2019.
- [35] W. Han, H. Chu, Y. Ya, S. Dong, and C. Zhang, "Effect of fuel structure on synthesis of carbon nanotubes in diffusion flames," *Fullerenes, Nanotubes and Carbon Nanostructures*, vol. 27, no. 3, pp. 265–272, 2019.
- [36] A. Imran, M. Varman, H. H. Masjuki, and M. A. Kalam, "Review on alcohol fumigation on diesel engine: a viable alternative dual fuel technology for satisfactory engine performance and reduction of environment concerning emission," *Renewable and Sustainable Energy Reviews*, vol. 26, pp. 739–751, 2013.
- [37] J. Campos-Fernández, J. M. Arnal, J. Gómez, and M. P. Dorado, "A comparison of performance of higher alcohols/diesel fuel blends in a diesel engine," *Applied Energy*, vol. 95, pp. 267–275, 2012.
- [38] P. Dagaut, J. Boettner, and M. Cathonnet, "Kinetic modeling of ethanol pyrolysis and combustion," *Journal de Chimie Physique*, vol. 89, pp. 867–884, 1992.
- [39] F. Liu, H. Guo, J. Smallwood, and Ö. Gülder, "The chemical effects of carbon dioxide as an additive in an ethylene diffusion flame: implications for soot and NO_x formation," *Combustion and Flame*, vol. 125, no. 1-2, pp. 778–787, 2001.
- [40] H. Wang, "Formation of nascent soot and other condensed-phase materials in flames," *Proceedings of the Combustion Institute*, vol. 33, no. 1, pp. 41–67, 2011.
- [41] A. Raj, M. Sander, V. Janardhanan, and M. Kraft, "A study on the coagulation of polycyclic aromatic hydrocarbon clusters to determine their collision efficiency," *Combustion and Flame*, vol. 157, no. 3, pp. 523–534, 2010.

- [42] H. Chu, W. Han, W. Cao, C. Tao, M. Raza, and L. Chen, "Experimental investigation of soot morphology and primary particle size along axial and radial direction of an ethylene diffusion flame via electron microscopy," *Journal of the Energy Institute*, vol. 92, no. 5, pp. 1294–1302, 2019.
- [43] B. Guan, Z. Li, D. Han, Z. Huang, and H. Lin, "Size distribution of soot particles in premixed *n*-heptane and methylcyclohexane flames," *Energy & Fuels*, vol. 32, no. 3, pp. 3883–3890, 2018.
- [44] M. L. Botero, S. Mosbach, and M. Kraft, "Sooting tendency and particle size distributions of *n*-heptane/toluene mixtures burned in a wick-fed diffusion flame," *Fuel*, vol. 169, pp. 111–119, 2016.
- [45] D. Zhang, J. Fang, J. f. Guan et al., "Laminar jet methane/air diffusion flame shapes and radiation of low air velocity coflow in microgravity," *Fuel*, vol. 130, pp. 25–33, 2014.
- [46] H. A. K. Shahad and Y. K. A. Mohammed, "Investigation of soot formation and temperature field in laminar diffusion flames of LPG-air mixture," *Energy Conversion and Management*, vol. 41, no. 17, pp. 1897–1916, 2000.

Research Article

Exploring the Benefits of Annular Rectangular Rib for Enhancing Thermal Efficiency of Nonpremixed Micro-Combustor

Hongcai Wang,¹ Hongru Fang,¹ Bingqian Lou,¹ Shitu Abubakar ,² Yuqiang Li ,¹ and Lei Meng ³

¹School of Energy Science and Engineering, Central South University, Changsha 410083, China

²College of Mechanical and Electrical Engineering, Central South University, Changsha 410083, China

³School of Automation, Wuhan University of Technology, Wuhan 430070, China

Correspondence should be addressed to Yuqiang Li; csulyq@csu.edu.cn and Lei Meng; menglei1986@gmail.com

Received 5 October 2019; Revised 8 December 2019; Accepted 20 January 2020; Published 13 February 2020

Guest Editor: Yaojie Tu

Copyright © 2020 Hongcai Wang et al. This is an open access article distributed under the Creative Commons Attribution License, which permits unrestricted use, distribution, and reproduction in any medium, provided the original work is properly cited.

Micro-combustor can provide the required thermal energy of micro-thermal photovoltaic (MTPV) systems. The performance of MTPV is greatly affected by the effectiveness of a micro-combustor. In this study, a numerical simulation was conducted to explore the benefits of annular rectangular rib for enhancing the thermal performance of a nonpremixed micro-combustor. Based on the investigations under various rib heights, rib positions, and inlet mass flow rates, it is found that the addition of annular rectangular ribs in the micro-combustor creates a turbulent zone in the combustion chamber, thereby enhancing the heat transfer efficiency between the inner wall of the combustion chamber and the burned gas. The micro-combustor with annular rectangular rib shows a higher and more uniform wall temperature. When the H_2 mass flow is 7.438×10^{-8} kg/s and the air mass flow is 2.576×10^{-6} kg/s, the optimum dimensionless rib position is at $l = 6/9$ and $r = 0.4$. At this condition, the micro-combustor has the most effective and uniform heat transfer performance and shows significant decreases in entropy generation and exergy destruction. However, the optimum l and r significantly depend on the inlet mass flow of H_2 /air mixture.

1. Introduction

The micro-power system has the characteristics of small capacity, high heat loss, unstable combustion, etc. and is more unstable than macroscopic combustion. Some prototypes of micro-power devices have been extensively developed and studied, like micro-combustion batteries, micro-turbines, and micro-thermal photovoltaic (MTPV) systems. In recent years, micro-thermal photovoltaic (MTPV) systems have been receiving much attention due to their potential application as reliable energy sources. In MTPV system, the heat energy is generated after the combustion of fuel, the radiation wall of micro burner can convert the heat energy into radiation photons with a certain amount of energy through its radiation characteristics, and some of the radiation photons are received by the evenly distributed photocell elements on the wall of micro burner and then converted into electrical energy and output to the

outside. Conventionally, micro-combustor often uses hydrogen and hydrocarbon compounds as fuel and has some advantages such as high energy conversion efficiency, simple physical structure, and substantial energy output per unit volume. To enhance the energy conversion efficiency of micro-combustor, a lot of methods have been investigated and reported in the literature. The micro-combustor is designed to achieve improved heat transfer performance, and the improved combustor presents higher and more uniform wall temperature, which is the yardstick for its performance appraisal.

Numerous scholars have established novel micro-combustion chambers by adopting various methods for realizing high and uniform wall temperature. Chou et al. [1] have successfully used porous media. Pan et al. [2] and Li et al. [3–5] improved flame stability in the microchannel by enhancing heat transfer. Catalytic combustion can be used to improve fuel conversion efficiency [6–11]. The Swiss roll

combustor's combustion characteristics have been extensively studied by Vijayan and Gupta [12, 13], Shirsat and Gupta [14], and Wierzbicki et al. [15]. It can be seen from the results that Swiss roll combustor extremely improves the combustion stability and also extends the extinction limit. Bagheri and Hosseini [16] investigated two different thermal cycling combustors and compared their heat loss, flame propagation, flame thickness, excess enthalpy, velocity, and emitter efficiency. Hosseini and Wahid [17] investigated the characteristics of two different flameless states of CH_4/air . Their findings show that micro-flameless combustion is smoother with using bluff-body. Wan et al. [18, 19] proposed a micro cavity-combustor. It can be concluded from their findings that, with the increase of equivalent ratio, the flame limit is extended. Another method which is also considered effective is heat recirculating [20, 21]. The irreversible energy loss caused by combustion of the fuel cannot be neglected. Jejurkar and Mishra [22] carried out related research about the relationship between micro-combustor performance and thermal conductivity of the wall, and the findings of the study show that, at higher thermal conductivities, the wall heat losses unfavorably influenced the exergetic property of micro-combustor. Moreover, the thermal conductivity of the wall in the range of 0.1–1.75 W/m·K was discovered to be appropriate for obtaining high exergetic efficiency and uniform wall temperature. Briones et al. [23] examined the propagation of a layered H_2 -rich CH_4 air flame by numerical method. The results show that as the H_2 content in the fuel increases, both heat transfer and chemical reactivity increase, leading to an increase in entropy.

Moreover, MTPV system also has the problem of low total energy conversion efficiency [24–27]. Research has indicated that the uniformity of combustion chamber wall temperature influences the energy conversion efficiency of MTPV system [28]. In addition, [4, 23] Li et al. [4, 29, 30] established that the use of porous media contributed immensely to the wall temperature rise, which translates into the efficiency of the combustor. Yang et al. conducted experiments by adding heat recuperator [30] or a block [31] insert in micro-combustors. The results show that both methods can effectively improve the uniformity of wall temperature distribution. Jiang et al. [32, 33] researched the effect of block inserts (baffles) on combustor efficiency. The effective position of the baffles was ascertained, which significantly improved the uniformity of the wall temperature distribution. Tang [34] and Su et al. [35] established a multichannel micro-combustors for micro-thermal photovoltaic systems. Under various conditions, the premixed H_2/air mixture combustion behavior was researched. The results show that the outer wall temperature of the multichannel micro-combustor is significantly enhanced compared to the single-channel micro-combustor. Chen et al. [36–38] used the lattice Boltzmann model to solve the governing equations of the premixed and nonpremixed reverse jet H_2 -air combustion process and found different entropy generation analysis features from previous studies. Moreover, Emadi and Emami [39] investigated the exergy loss and the local entropy generation of CH_4 -air bluff-body flame burning in the combustor under turbulent nonpremixed H_2 -enriched.

It was shown that exergy loss and entropy generation are reduced by adding H_2 . Datta [40] investigated diffusion flames in constrained geometries at different gravity levels to analyze the effect of gravity on the second law efficiency and entropy production rate. The results showed that, under normal gravity, the entropy production rate caused by heat transfer was significantly increased compared to zero gravity and, at all gravity levels, the entropy production rate caused by chemical reactions and mass transfer was almost constant.

These experimental studies reveal the importance of flame stability and thermal characteristics to the combustor performance and introduce several effective combustion chamber structural designs and methods. Ban et al. [41] studied the effect of buoyancy on different flames by examining the flame shape for horizontally oriented combustors. However, they did not study the effect of extended surfaces for better heat transfer. Resende et al. [42] summarized the pertinent investigations revolved around nonpremixed diffusion combustion regime, which is commonly employed in practical systems. The review has pinpointed important factors for realizing improved burner performance such as the burner configuration. Research is still relevant to nonpremixed H_2/air combustion by considering some influential geometric parameters that promote the efficiency of the combustion process. This study is aimed at finding a suitable combustion structure that provides elevated outer wall temperature and exhibits effective and uniform heat transfer distribution for the nonpremixed micro-combustor. A nonpremixed micro-combustor with annular rectangular rib was proposed, and the effect of annular rectangular ribs on the heat transfer performance of the nonpremixed micro-combustor was numerically investigated under varying air and H_2 mass flow rate, rib position, and rib height.

2. Numerical Model

2.1. Physical Model of Micro-Combustor. Figure 1 shows the schematic of a micro-combustor combining a backward step and a cavity [43]. The micro-combustor has an overall maximum outer diameter of 1.6 mm and a length of 12 mm. The front end and the rear end of the micro-combustor have dissimilar internal contours. The front end is contoured into four tubes: the suction pipe A, the mixing pipe B, the diffusion pipe C, and the shrink pipe D. Hydrogen and air simultaneously enter into the micro burner through the inlet side; the hydrogen inlet is a circular shape with a diameter of 0.2 mm, and the air inlet is an annular passage with the outer diameter of 0.862 mm and the inner diameter of 0.6 mm.

Hydrogen and air enter the micro-combustor through the central circular passage and the outer annular passage of the suction pipe A, respectively. The shrinking shape of the straw A enables the air and hydrogen to obtain oblique velocities toward the centerline. In the mixing pipe B, air and H_2 are mixing. Furthermore, the arrangement of the diffuser tube C enables the dynamic pressure portion to be converted into static pressure, thereby increasing the pressure difference, while the suction efficiency is also enhanced by the

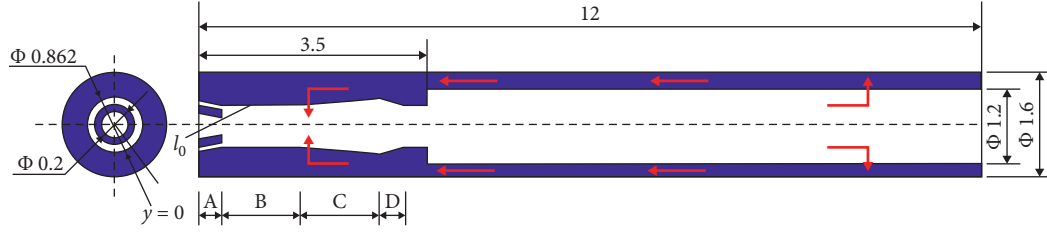


FIGURE 1: Schematic of the micro-combustor (units in mm).

action of the diffuser pipe C. The shrinkage pipe D is provided to prevent tampering [44].

As shown in Figure 2, the model shown in Figure 1 is modified by adding an annular rectangular rib at a certain distance from combustor inlet, and the channel is divided into two parts. The fixed width of the annular rectangular rib is 1.0 mm, and the position ($L3$) and height (H) of the annular rectangular ribs are variable geometric parameters. By setting the height and position of the dimensionless annular rectangular ribs to $r=2H/d3$ and $l=L3/L1$, respectively, the effect of the annular rectangular ribs on the outer wall temperature of the micro-combustor can be investigated.

In nonpremixed micro-combustor, to better study the influence of ribs on the combustion characteristics, as shown in Table 1, the optimum rib positions and rib heights that are suitable for higher efficiency of a micro-combustor were determined. The model parameters of four different rib heights and different rib positions are set in this study to conduct a thorough parameter comparison study. The combustors shown in Figures 1 and 2 are both made of steel material with good thermal conductivity and good corrosion resistance.

2.2. Mathematical Model. In combustion simulation of micro-combustor, assuming hydrogen with light weight, small volume, long life, and high-efficiency density, in the reactants, gaseous substances can be considered as a continuous medium, expressed by the Navier–Stokes equation. Owing to the mass flow of H_2 and the low rate of air, the effects of dissipative forces and fluid volume are ignored. The modeling considers various equations. These equations are defined as follows:

Conservation equation of mass:

$$\frac{\partial}{\partial x}(\rho u) + \frac{1}{r} \frac{\partial}{\partial r}(\rho v r) = 0. \quad (1)$$

Momentum conservation equation:

$$\frac{\partial}{\partial x_j}(\rho u_i u_j - \tau_{ij}) = -\frac{\partial p}{\partial x_{ij}}. \quad (2)$$

Energy conservation equation:

$$\frac{\partial}{\partial x_j}(\rho u_j h + F_{i,j}) = u_j \frac{\partial p}{\partial x_j} + \tau_{ij} \frac{\partial u_i}{\partial x_j}. \quad (3)$$

Species equation:

$$\frac{\partial}{\partial x_j}(\rho u_j m_i + J_{i,j}) = R_i. \quad (4)$$

Wall energy conservation equation:

$$\frac{\partial(\lambda_w \partial T)}{\partial x_i^2} = 0. \quad (5)$$

Ideal gas equation:

$$P = \rho RT \sum \frac{m_i}{M_i}. \quad (6)$$

For the sake of acquiring the optimum annular rectangular ribs settings to enhance the temperature and its uniformity of the outer wall, the positions of the ribs and the rib heights geometry were varied and studied using numerical simulation. In the analysis, the outer wall temperature difference is adopted in expressing the uniformity of heat transfer of the micro-combustor, and its outer wall temperature difference can be expressed as follows:

$$\nabla T = T_{\text{outwall,max}} - T_{\text{outwall,min}}. \quad (7)$$

Entropy transport equation:

$$T ds = du + p d\left(\frac{1}{\rho}\right) - \sum_{j=1}^n d\left(\frac{n_j}{\rho}\right). \quad (8)$$

Consequently, the total entropy generation S_{gen} is written as follows:

$$S_{\text{gen}} = ms. \quad (9)$$

In a combustion process, because the exergy destruction E_{des} and the total entropy generation are in the direct ratio, it is expressed as follows:

$$E_{\text{des}} = S_{\text{gen}} T_0. \quad (10)$$

2.3. Computational Mesh and Boundary. Due to the complexity of the geometric model, which consisted of a backward-facing step and four pipes, numerical simulation of 2D models using CFD Fluent 19.0 was carried out. Some researches [43, 45, 46] have suggested that the turbulent model can accurately predict combustion behaviors at the inlet flow $Re > 500$. As a result, standard $k-\epsilon$ model is chosen in this work. The combustion reaction only involves the combustion of hydrogen; the chemical kinetic mechanism of Fluent was adopted. This mechanism comprises 11

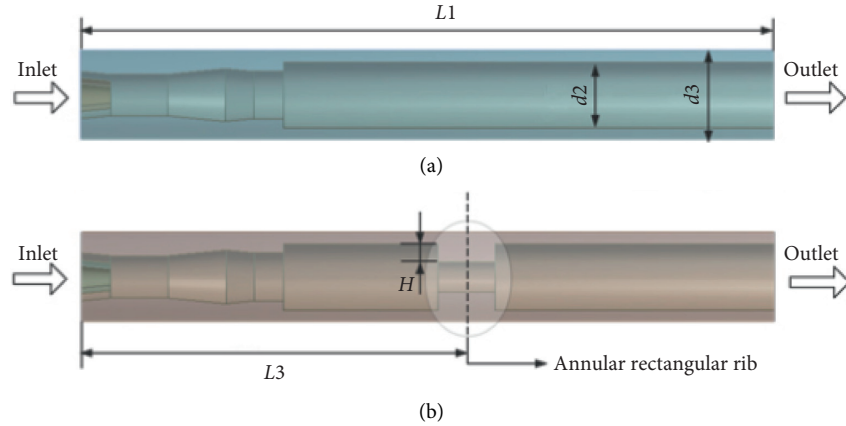


FIGURE 2: Schematic diagram of nonpremixed micro column burners: (a) without annular rectangular ribs and (b) with annular rectangular ribs.

TABLE 1: Dimensionless rib height and rib position.

Rib height	Rib position		
4/9	0.25	0.325	0.4
5/9	0.25	0.325	0.4
6/9	0.25	0.325	0.4
7/9	0.25	0.325	0.4

elementary species, and the detailed chemical reaction mechanism is shown in Table 2.

In the research, the simulated combustion of micro-combustor uses standard $k-\epsilon$ model. The H_2 and air mass flow rates are both considered as the inlet boundary conditions, while the outlet pressure was used as the outlet boundary condition. The ambient temperature is 298 K and the ambient pressure is 1.01×10^5 Pa. At the same time, the no-slip boundary condition is adopted. Both convective and radiative heat transfer of the environment are considered in the outer wall of the combustion chamber. For the convergence criterion, it is also necessary to set the residual value; the residuals for velocity and continuity are set as 1×10^{-3} , and the residuals for do-intensity and energy are set as 1×10^{-6} . The equations involved are all set to second-order upwind scheme discretization.

This study presents the nonpremixed micro column combustor, with an annular rectangular shape rib. Therefore, in order to expedite the calculation process, the analysis was simplified to a two-dimensional numerical analysis at the center of a section.

Table 3 provides the model boundary condition; mass-flow-rate boundary condition was adopted for inlet, and the pressure-outlet boundary was employed for the outlet. In both boundaries the gauge pressure is set to 0 MPa.

A unified 2D grid is built to calculate the heat transfer and the combustion in the micro-combustor. A model grid of micro-combustor is generated as presented in Figure 3. For the case where the value of equivalence ratio is 1.0, the air and H_2 mass flow rates are maintained at 4.632×10^{-6} and 1.347×10^{-7} kg/s, respectively. Grid-independent testing was performed by modifying the number of elements to a finer

TABLE 2: Chemical reaction mechanism of H/air combustion.

Reactions	A_k ($m^3/(kmol s)$)	β_k	E_k (J/kmol)
1. $O_2 + H = O + OH$	3.55×10^{12}	-0.4	6.945×10^7
2. $O + H_2 = H + OH$	50.8	2.7	2.632×10^7
3. $H_2 + OH = H_2O + H$	2.16×10^5	1.5	1.435×10^7
4. $O + H_2O = 2OH$	2970	2	5.607×10^7
5. $H_2 = 2H$	4.58×10^{16}	-1.4	4.351×10^8
6. $2O = O_2$	6.16×10^9	-0.5	0
7. $O + H = OH$	4.71×10^{12}	-1	0
8. $H + OH = H_2O$	3.8×10^{16}	-2	0
9. $H + O_2 = HO_2$	1.48×10^9	0.6	0
10. $HO_2 + H = H_2 + O_2$	1.66×10^{10}	0	3.443×10^6
11. $HO_2 + H = 2OH$	7.08×10^{10}	0	1.234×10^6
12. $HO_2 + O = O_2 + OH$	3.25×10^{10}	0	0
13. $HO_2 + OH = H_2O + O_2$	2.89×10^{10}	0	-2.08×10^6
14. $2HO_2 = H_2O_2 + O_2$	4.2×10^{11}	0	5.021×10^7
15. $H_2O_2 = 2OH$	2.95×10^{14}	0	2.025×10^8
16. $H_2O_2 + H = H_2O + OH$	2.41×10^{10}	0	1.661×10^7
17. $H_2O_2 + H = HO_2 + H_2$	4.82×10^{10}	0	3.326×10^7
18. $H_2O_2 + O = OH + HO_2$	9550	2	1.661×10^7
19. $H_2O_2 + OH = HO_2 + H_2O$	1×10^9	0	0

Note: A_k is the preexponential factor of reaction rate, β_k is the temperature exponent, and E_k is the activation energy of the reaction.

TABLE 3: Model boundary condition.

H_2 inlet	H_2 mass flow (kg/s)	7.483×10^{-8}
	Turbulence intensity	5%
	Hydraulic diameter	0.0004
Air inlet	Air mass flow (kg/s)	2.573×10^{-6}
	Turbulence intensity	5%
	Hydraulic diameter	0.001
Pressure outlet	Turbulence intensity	5%
	Hydraulic diameter (m)	0.0012
Outer wall	Heat transfer coefficient	10
	Emissivity	0.85

one and is presented in Figure 4. By observing and comparing three different grids, the three grids have 15719, 19061, and 23987 cells, respectively. The mesh with 15719

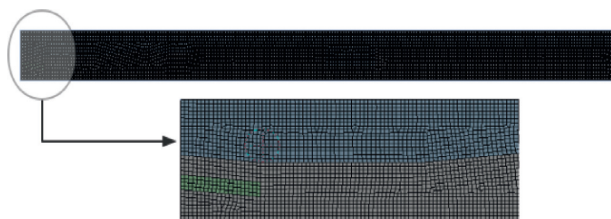


FIGURE 3: Computational mesh of nonpremixed micro-combustor.

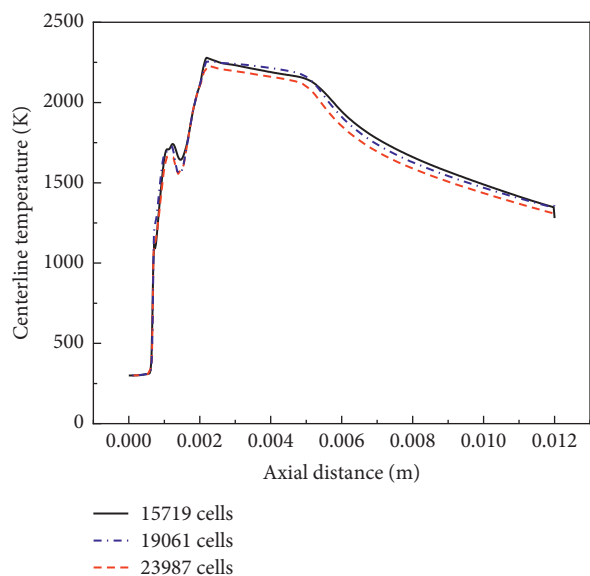


FIGURE 4: Axial temperature profile of simulation.

cells and the mesh with 23987 cells are of the highest and lowest temperature on centerline, respectively. Moreover, temperature difference of the resulting centerline temperature profile is diminutive under three different numbers of grids. Therefore, the mesh with 19061 cells has better accuracy and less computation time, making it more suitable for numerical investigation.

2.4. Model Validation. The simulated results were compared with the experimental results to confirm the validation of the model. And the experimental results are obtained from the group of E. In the experiments in a silicon material micro-combustor, the H_2 and the air mass flow are maintained at 1.347×10^{-7} kg/s and 4.632×10^{-6} kg/s, respectively. The measurement points of the experiment are situated at 2, 5, 8, and 10 mm in the axial length of the micro-combustor.

Experimental outer wall temperature at varying combustor lengths [43] and the numerical prediction are compared as represented in Figure 5. The temperature data of the corresponding position is calculated by simulating the hydrogen inlet mass flow of 1.347×10^{-7} kg/s and the equivalence ratio of 1.0. In order to obtain a viable model, the deviation of the experimental results and the numerical results should be as small as possible. As can be seen from Figure 5, the deviation is less than 4.72%. Therefore, it is feasible to analyze the performance of the micro-combustor by simulation.

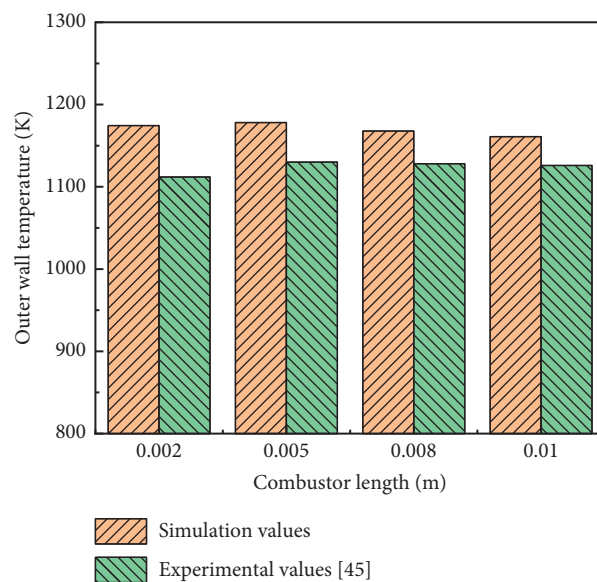


FIGURE 5: Comparison between simulated and experimental values.

3. Results and Discussions

3.1. Effects of Annular Rectangular Rib on Outer Wall Temperature. Figure 6 shows the temperature cloud diagram of different r and l . From the figure, it can be observed that the change in rib positions and rib heights of the annular rectangular ribs in the micro-combustor is proportional to the temperature distribution of flow field. Figure 7 presents the temperature distribution of the outer wall that the micro-combustor has under different l and r . The inlet H_2 and the air rates of mass flow were maintained at 7.383×10^{-8} kg/s and 2.573×10^{-6} kg/s with an H_2 /air equivalent ratio of 1.0. It can be seen from the figure that when the l of the micro-combustor is a fixed constant, the temperature at outer wall increases as the r increases. This can be explained by the fact that, by the raise of the dimensionless rib heights, the turbulence zone becomes wider, and the turbulence area at the rear of the annular rectangular rib expands in proportion to the dimensionless rib heights, effectively improving the heat transmission capability of the micro-combustor. However, it is worth noting in Figure 8 that the optimum settings for the maximum outer wall temperature are at $l = 5/9$ and $r = 0.325$. The good performance obtained is a result of the ribs being very close to the center of the flame, reducing the positive impact of expanding the turbulence area and weakening the negative influence of the annular rectangular ribs on the heat transmission of the micro-combustor.

It can be seen from Figure 8(a) that the l of micro-combustor is a fixed constant, and the mean outer wall temperature increases proportionally with the r . The changing trend of Figure 8(a) is the same as the change of the temperature distribution of outer wall in Figure 7. Figure 8(b) shows the temperature difference of the outer wall temperature at different rib positions and heights. The uniformity of the heat transfer of the combustor is manifested by the magnitude of the outer wall temperature difference. The smaller the difference of temperature, the

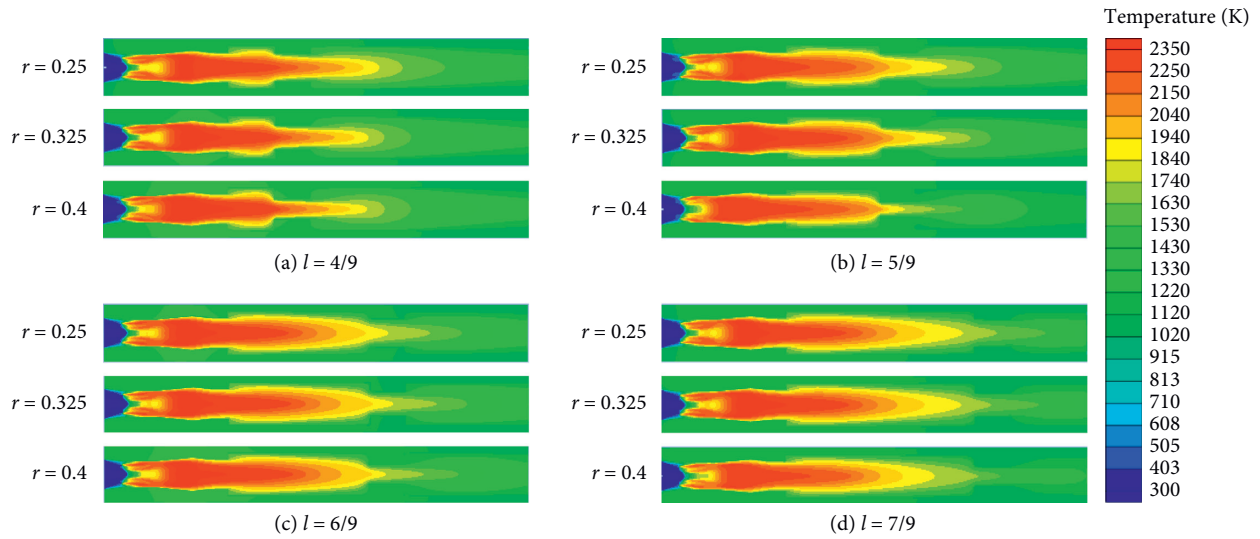
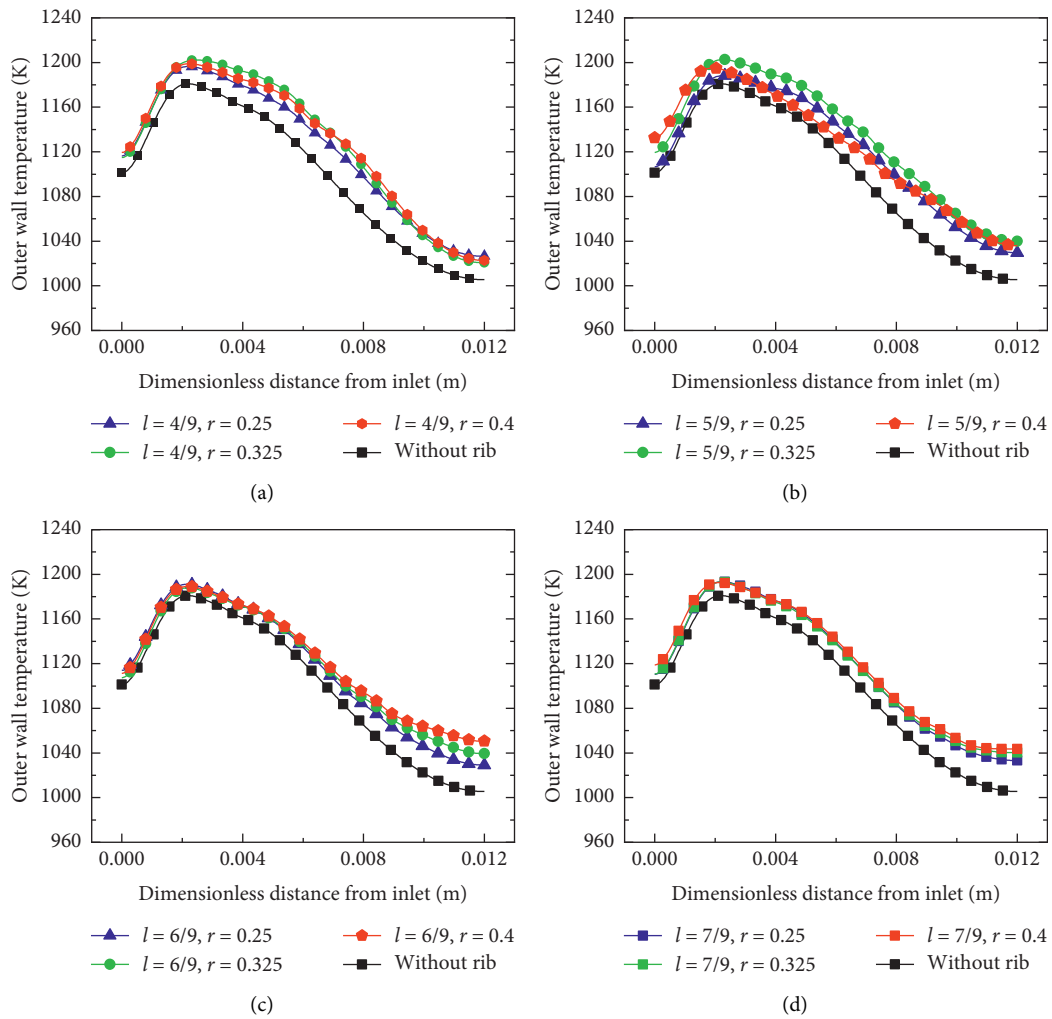
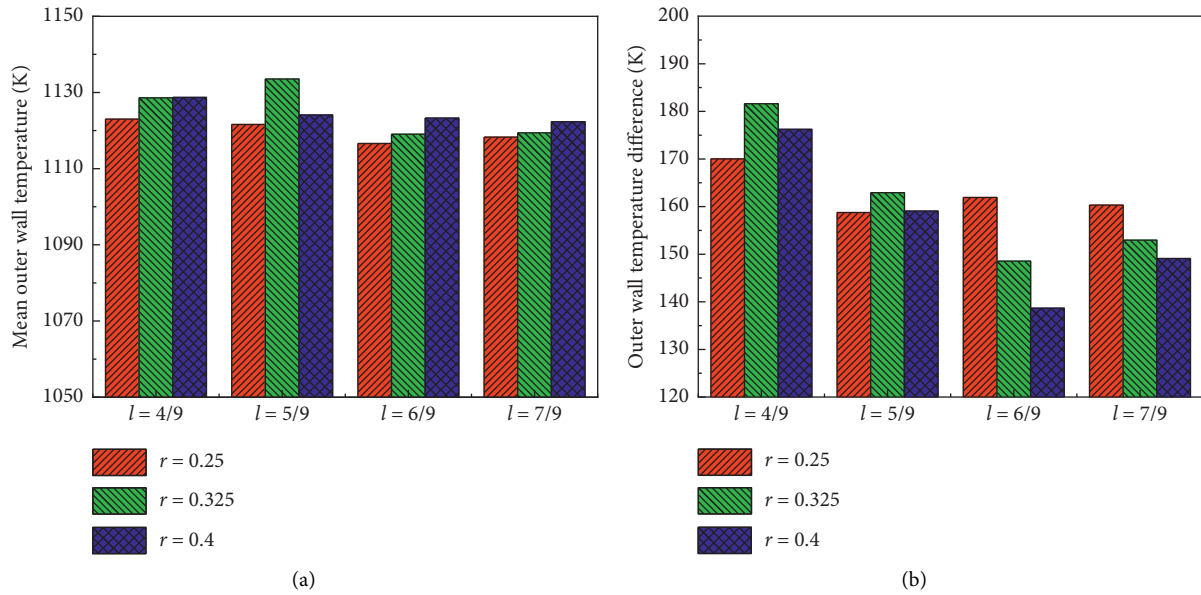
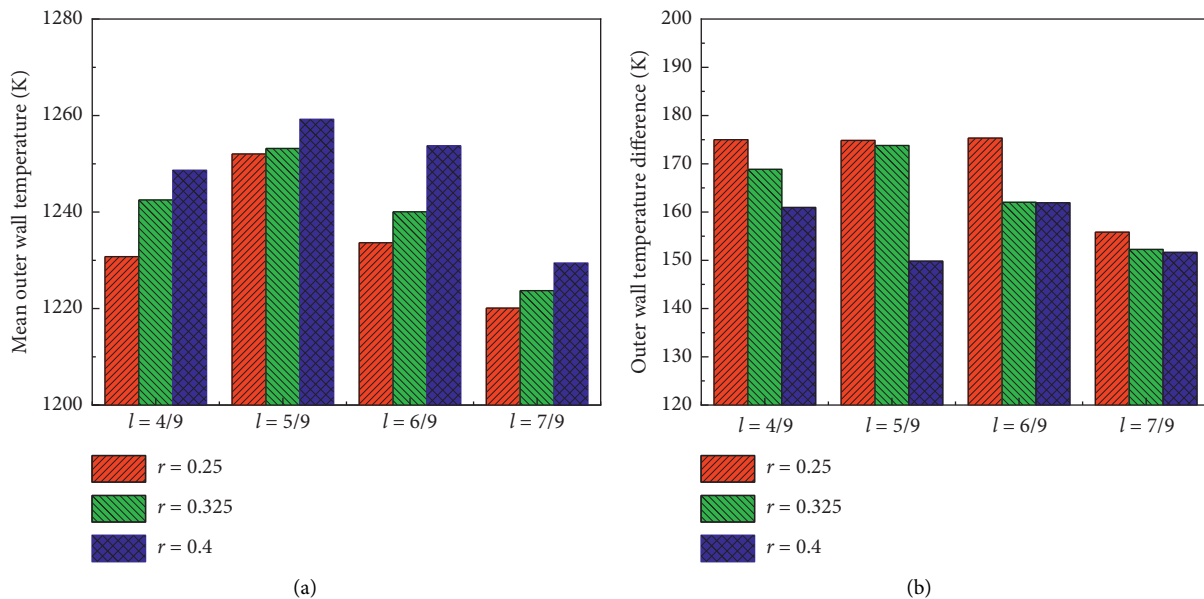
FIGURE 6: Spatial distribution of temperature at $l = 4/9$.

FIGURE 7: Outer wall temperature at different rib positions and heights.

FIGURE 8: Mean outer wall temperature and outer wall temperature at various l and r .FIGURE 9: Mean outer wall temperature and outer wall temperature at different l and r .

more uniform the heat transfer. Also, the temperature difference is maximum at $l = 5/9$ and $r = 0.325$; the temperature difference is minimum at $l = 6/9$ and $r = 0.4$, and more effective uniform heat transfer is realized.

By varying the inlet mass flow rate and repeating the above simulation experiment procedure, the results shown in Figures 9 and 10 were obtained. The inlet H_2 and the air mass flow rate were maintained at 1.347×10^{-7} kg/s and 4.632×10^{-6} kg/s, respectively, leading to the results obtained in Figure 9. Similarly, the inlet H_2 and the air mass flow rates were maintained at 1.646×10^{-7} kg/s and 5.661×10^{-6} kg/s, respectively, producing the results obtained in Figure 10. Both results were obtained at equivalence ratio of 1.0. It was

observed that the position and height of the ribs with the minimum and maximum outer wall temperature are affected. This is because the increase in inlet mass flow speeds up the mass flow rate of the inlet, causing the center of the flame to move toward the rear of the micro-combustor. It can be seen from the result that the positions and heights of the rib with the best heat transfer efficiency are influenced by inlet mass flow rate and vary as the inlet flow rate changes.

3.2. Effects of Annular Rectangular Rib on Field Entropy Destruction. Exergy destruction is energy that cannot be converted into useful work in a reversible process. To further

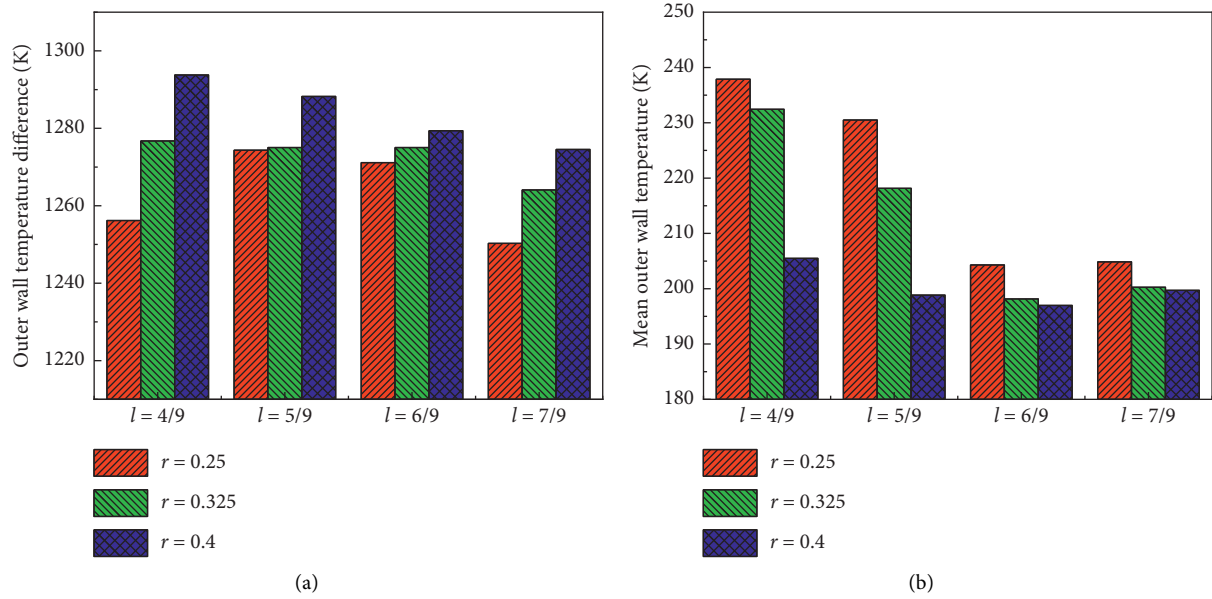


FIGURE 10: Mean outer wall temperature and outer wall temperature at different l and r .

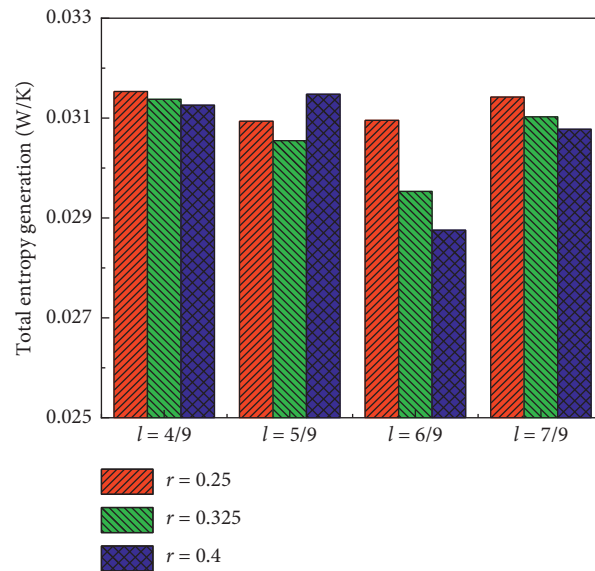


FIGURE 11: Total entropy generation under various l and r .

demonstrate the combustion characteristics of the ribbed micro-combustor, it can be analyzed by entropy generation and exergy destruction.

Figure 11 shows the change of total entropy generation at various rib positions l and heights r . The different rib positions and heights have an important influence on the entropy field. It is shown that at $l = 6/9$ and $r = 0.4$, the total entropy generation decreases significantly. This is due to the potential to lose more available energy at high gas temperatures. Equation (10) was used to generate the exergy destruction results under various rib positions and heights, as presented in Figure 12. It is easy to see that the exergy destruction decreases drastically at $l = 6/9$ and $r = 0.4$. The results presented in Figures 10 and 13 are both obtained at

H_2 and air mass flow rates maintained at 1.347×10^{-7} kg/s and 4.632×10^{-6} kg/s, respectively, and H_2 /air equivalent ratio of 1.0. The change trend is the same as the outer wall temperature change trend.

3.3. Effects of Annular Rectangular Rib on Field Synergy Angle.

The field synergy principle is an important factor to be considered to further demonstrate and analyze the problem of heat transfer enhancement of micro-combustors. Thus, the field synergy equation of the thermal boundary layer is integrated to prove that reducing the angle between the temperature gradient and the velocity vector is an effective measure to enhance the convective heat transfer. The

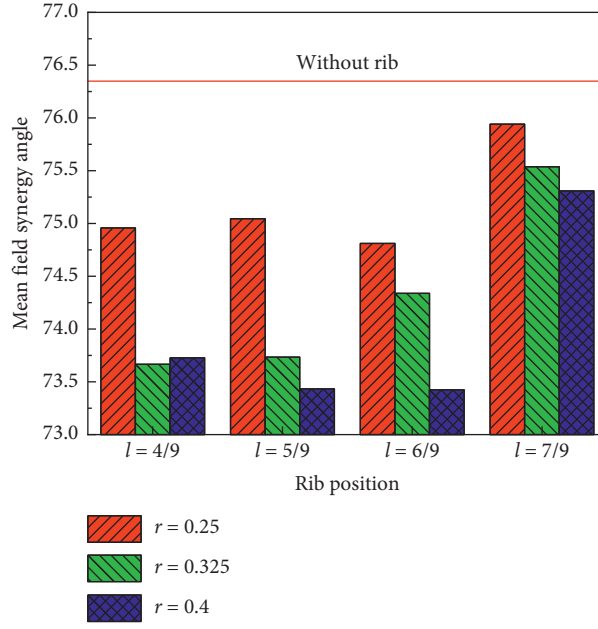
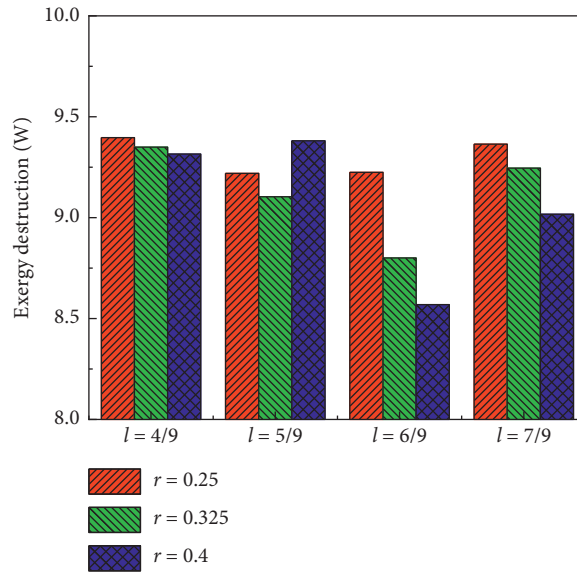


FIGURE 12: Mean field synergy angle at different rib positions and heights.

FIGURE 13: Exergy destruction under various l and r .

intensity of heat transfer in the micro-combustor can be more intuitively represented by the field synergy angle.

The nonpremixed micro column combustor was analyzed by the concept of field synergy principle. This principle shows that heat transfer is affected by the characteristics of the temperature field, the velocity field, and also the angle of synergy between the velocity vector and the temperature gradient:

$$\iiint_{\Omega} \rho C_p (\nabla T \cdot \vec{u}) dV = \iiint_{\Omega} (\lambda_f \cdot \nabla T) dV. \quad (11)$$

The dot product of the temperature gradient and the velocity vector can be written as follows:

$$\vec{u} \cdot \nabla T = |\vec{u}| |\nabla T| \cos \theta. \quad (12)$$

Since this study established a 2D axisymmetric model, the synergy angle between the velocity vector and the temperature gradient is expressed as the following equation:

$$\cos \theta = \frac{(\partial T / \partial x) \cdot u + (\partial T / \partial r) \cdot v}{\sqrt{(\partial T / \partial x)^2 + (\partial T / \partial r)^2} \cdot \sqrt{u^2 + v^2}}. \quad (13)$$

Figure 14 shows the temperature cloud diagram of different rib positions l and rib heights r . After adding the ribs on the micro-combustor, to see the change of the field synergy angle more clearly and intuitively, the cosine value is

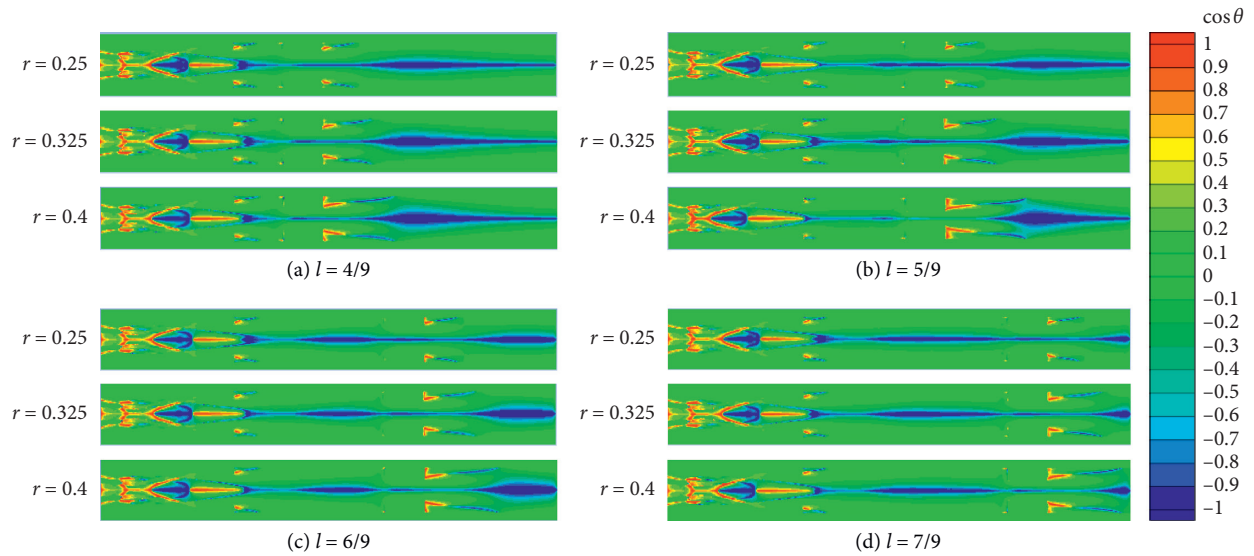
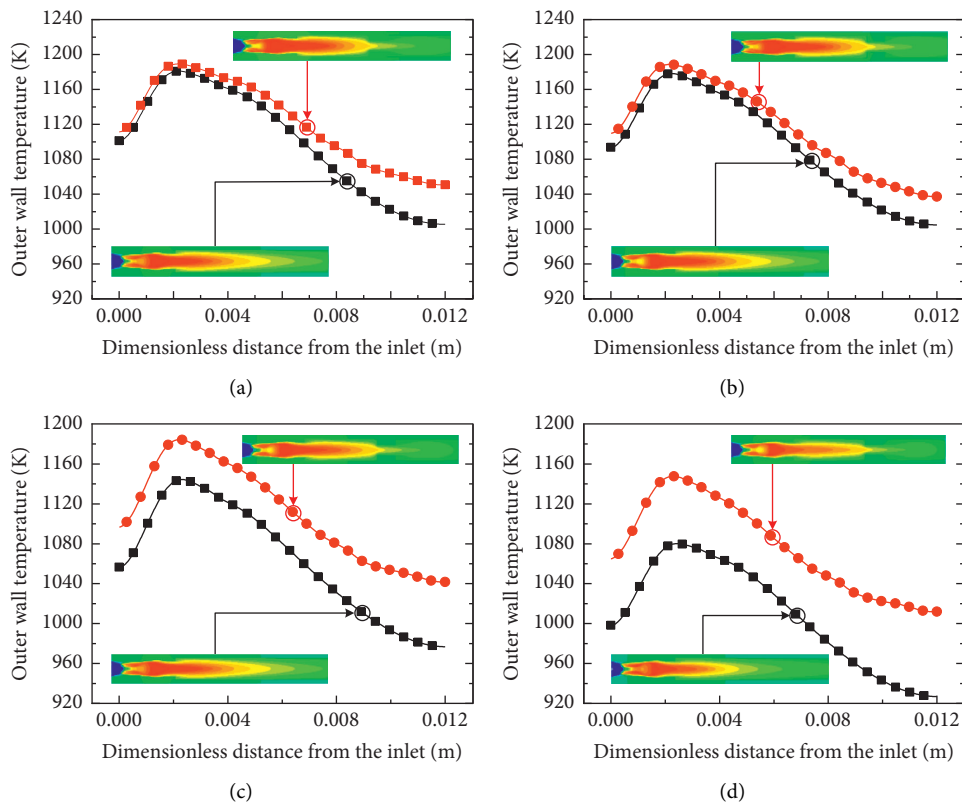
FIGURE 14: Cosine of field synergy angle at $l=4/9$.

FIGURE 15: Comparison of outer wall temperature distribution at various equivalent ratios.

converted into an angle and the angle is treated as a range of 0° – 90° ; that is, the angle of 90° – 180° takes its complement angle.

A conclusion can be drawn from Figure 12 that the field synergy angle of a nonpremixed micro-combustor having annular rectangular ribs is lower than the field synergy angle of a micro-combustor without ribs. It has been proved again

that after the ribs are added, the heat transfer of the micro-combustor is enhanced. Similarly, it was established that when the inlet H_2 and the air mass flow rates are maintained at 7.438×10^{-8} kg/s and 2.573×10^{-6} kg/s, respectively, at H_2 /air equivalent ratio of 1.0, $l=6/9$, and $r=0.4$, the field synergy angle is minimum, and the best heat transfer performance is obtained.

TABLE 4: Results of two types of micro-combustors under different equivalence ratios.

Heat transfer properties		Equivalence ratios		
		0.9	0.8	0.7
Mean outer wall temperature (K)	Without rib	1096.773	1064.245	1009.532
	With rib	1116.656	1111.187	1077.419
Outer wall temperature difference (K)	Without rib	173.4	167.679	153.287
	With rib	151.56	142.83	135.75

3.4. *Effect of Annular Rectangular Ribs on Micro-Combustors at Various H_2 /Air Equivalent Ratios.* As shown in Figure 15, when H_2 mass flow is maintained at 7.438×10^{-8} kg/s, the micro-combustor with annular rectangular ribs ($l=6/9$, $r=0.4$) has a higher outer wall temperature at different equivalence ratios ($u=1.0, 0.9, 0.8$, and 0.7). Moreover, the mean temperature of outer wall and its temperature difference were also compared to better analyze the difference in heat transfer performance between the two combustors at various equivalent ratios. As can be seen from Table 4, the micro-combustor with annular rectangular ribs ($l=6/9$, $r=0.4$) is compared to those without ribs under varying equivalence ratios. Better performance can be obtained by adding annular rectangular ribs to the micro-combustor, and the outer wall temperature of the improved combustor is higher and more uniform at different equivalent ratios.

4. Conclusions

The combustion characteristics of nonpremixed H_2 /air micro-combustors with and without annular rectangular rib are analyzed by numerical investigation on the temperature distribution, heat transfer uniformity, and field synergy angle in combustion chamber. The combustion characteristics of micro-combustors under various rib positions, rib heights, and equivalent ratios were analyzed. Some specific conclusions can be summarized as follows:

- (1) The use of annular rectangular ribs can create a turbulent zone in the micro-combustor, which enhances the heat transfer efficiency between the inner wall of the combustion chamber and the burned fuel.
- (2) As the annular rectangular ribs approach the flame center, the positive effect of turbulent zone will be weakened, and the temperature will not increase with the increase of fin height. Also, as the rib height increases, the turbulence zone becomes wider and increases; consequently, the heat transfer performance is enhanced.
- (3) When the H_2 mass flow rate is 7.438×10^{-8} kg/s and the air mass flow rate is 2.576×10^{-6} kg/s, the most uniform heat transfer and a minimum field synergy angle are obtained at $l=6/9$ and $r=0.4$. Meanwhile, the entropy generation and exergy destruction are significantly decreased. However, the optimum l and r greatly depend on the inlet mass flow of H_2 /air mixture.
- (4) Based on the comparisons between both combustors performance under various equivalence ratios, it was established that the micro-combustor with annular

rectangular ribs contributes significantly to a higher and more uniform outer wall temperature.

Nomenclature

u, v :	Velocity component in the x, r -direction, m/s
ρ :	Gas density, kg/m^3
P :	Fluid pressure, Pa
τ_{ij} :	Stress tensor, N
u_j :	Velocity component in the x_j direction, m/s ($j=1, 2, 3$)
H :	Enthalpy of the gas, J/kg
F_{ij} :	Energy flux in the x_i direction, W
m_i :	Mass fraction of species, J/kg
$J_{l,j}$:	Diffusion flux of species l in the x_j direction, $\text{kmol}/(\text{m}^2\cdot\text{s})$
R_i :	Chemical reaction product rate, $\text{kmol}/(\text{m}^3\cdot\text{s})$
λ_w :	Wall thermal conductivity, $\text{W}/\text{m}\cdot\text{K}$
R :	Universal gas constant, $\text{J}/\text{Kmol}\cdot\text{K}$
M_i :	Molar mass of species
$T_{\text{outwall,max}}$:	Maximum outer wall temperature, K
$T_{\text{outwall,min}}$:	Minimum outer wall temperature, K
S :	Specific entropy
U :	Specific internal energy
u_j :	Chemical potential of species j
n_j :	Number density of species j
S_{gen} :	Total entropy generation
M :	Flow rate of gas
E_{des} :	Exergy destruction
T_0 :	Ambient temperature, 298 K
C_p :	Specific heat capacity
\vec{u} :	Speed vector
∇T :	Temperature gradient
Θ :	Synergy angle
dT/dx :	Axial temperature gradient
dT/dr :	Radial temperature gradient.

Data Availability

The data used to support the findings of this study are included within the article.

Conflicts of Interest

The authors declare that they have no conflicts of interest.

Acknowledgments

This work was supported by the National Natural Science Foundation of China (Grant nos. 51806250 and 61903287).

The authors are also thankful for the support by the Natural Science Foundation of Hunan Province, China (Grant no. 2019JJ50836).

References

- [1] S. K. Chou, W. M. Yang, J. Li, and Z. W. Li, "Porous media combustion for micro thermophotovoltaic system applications," *Applied Energy*, vol. 87, no. 9, pp. 2862–2867, 2010.
- [2] J. F. Pan, D. Wu, Y. X. Liu, H. F. Zhang, A. K. Tang, and H. Xue, "Hydrogen/oxygen premixed combustion characteristics in micro porous media combustor," *Energy Procedia*, vol. 61, pp. 1279–1285, 2014.
- [3] J. Li, H. Cui, and Y. Tian, "Nonlinearity analysis of measurement model for vision-based optical navigation system," *Acta Astronautica*, vol. 107, pp. 70–78, 2015.
- [4] J. Li, Q. Li, Y. Wang, Z. Guo, and X. Liu, "Fundamental flame characteristics of premixed H₂-air combustion in a planar porous micro-combustor," *Chemical Engineering Journal*, vol. 283, pp. 1187–1196, 2016.
- [5] J. Li, Y. Wang, J. Chen, J. Shi, and X. Liu, "Experimental study on standing wave regimes of premixed H₂-air combustion in planar micro-combustors partially filled with porous medium," *Fuel*, vol. 167, pp. 98–105, 2016.
- [6] C.-H. Leu, S.-C. King, J.-M. Huang et al., "Visible images of the catalytic combustion of methanol in a micro-channel reactor," *Chemical Engineering Journal*, vol. 226, pp. 201–208, 2013.
- [7] Y.-H. Li, G.-B. Chen, T.-S. Cheng, Y.-L. Yeh, and Y.-C. Chao, "Combustion characteristics of a small-scale combustor with a percolated platinum emitter tube for thermophotovoltaics," *Energy*, vol. 61, no. 4, pp. 150–157, 2013.
- [8] J. Ran, L. Li, X. Du, R. Wang, W. Pan, and W. Tang, "Numerical investigations on characteristics of methane catalytic combustion in micro-channels with a concave or convex wall cavity," *Energy Conversion and Management*, vol. 97, pp. 188–195, 2015.
- [9] S. A. Smyth and D. C. Kyritsis, "Experimental determination of the structure of catalytic micro-combustion flows over small-scale flat plates for methane and propane fuel," *Combustion and Flame*, vol. 159, no. 2, pp. 802–816, 2012.
- [10] T. A. Wierzbicki, I. C. Lee, and A. K. Gupta, "Combustion of propane with Pt and Rh catalysts in a meso-scale heat recirculating combustor," *Applied Energy*, vol. 130, no. 130, pp. 350–356, 2014.
- [11] T. A. Wierzbicki, I. C. Lee, and A. K. Gupta, "Rh assisted catalytic oxidation of jet fuel surrogates in a meso-scale combustor," *Applied Energy*, vol. 145, pp. 1–7, 2015.
- [12] V. Vijayan and A. K. Gupta, "Combustion and heat transfer at meso-scale with thermal recuperation," *Applied Energy*, vol. 87, no. 8, pp. 2628–2639, 2010.
- [13] V. Vijayan and A. K. Gupta, "Flame dynamics of a meso-scale heat recirculating combustor," *Applied Energy*, vol. 87, no. 12, pp. 3718–3728, 2010.
- [14] V. Shirsat and A. K. Gupta, "Performance characteristics of methanol and kerosene fuelled meso-scale heat-recirculating combustors," *Applied Energy*, vol. 88, no. 12, pp. 5069–5082, 2011.
- [15] T. A. Wierzbicki, I. C. Lee, and A. K. Gupta, "Performance of synthetic jet fuels in a meso-scale heat recirculating combustor," *Applied Energy*, vol. 118, no. 1, pp. 41–47, 2014.
- [16] G. Bagheri and S. E. Hosseini, "Impacts of inner/outer reactor heat recirculation on the characteristic of micro-scale combustion system," *Energy Conversion and Management*, vol. 105, pp. 45–53, 2015.
- [17] S. E. Hosseini and M. A. Wahid, "Investigation of bluff-body micro-flameless combustion," *Energy Conversion and Management*, vol. 88, pp. 120–128, 2014.
- [18] J. Wan, A. Fan, H. Yao, and W. Liu, "Flame-anchoring mechanisms of a micro cavity-combustor for premixed H₂/air flame," *Chemical Engineering Journal*, vol. 275, pp. 17–26, 2015.
- [19] J. Wan, W. Yang, A. Fan et al., "A numerical investigation on combustion characteristics of H₂/air mixture in a micro-combustor with wall cavities," *International Journal of Hydrogen Energy*, vol. 39, no. 15, pp. 8138–8146, 2014.
- [20] G. Wu, Z. Lu, W. Pan, Y. Guan, and C. Z. Ji, "Numerical and experimental demonstration of actively passive mitigating self-sustained thermoacoustic oscillations," *Applied Energy*, vol. 222, pp. 257–266, 2018.
- [21] G. Wu, Z. Lu, X. Xu et al., "Numerical investigation of aeroacoustics damping performance of a Helmholtz resonator: effects of geometry, grazing and bias flow," *Aerospace Science and Technology*, vol. 86, pp. 191–203, 2019.
- [22] S. Y. Jejurkar and D. P. Mishra, "Effects of wall thermal conductivity on entropy generation and exergy losses in a H₂-air premixed flame microcombustor," *International Journal of Hydrogen Energy*, vol. 36, no. 24, pp. 15851–15859, 2011.
- [23] A. Briones, A. Mukhopadhyay, and S. Aggarwal, "Analysis of entropy generation in hydrogen-enriched methane-air propagating triple flames," *International Journal of Hydrogen Energy*, vol. 34, no. 2, pp. 1074–1083, 2009.
- [24] G. Wu, D. Wu, Y. Li, and Li Meng, "Effect of acetone-n-butanol-ethanol (ABE) as an oxygenate on combustion, performance, and emission characteristics of a spark ignition engine," *Journal of Chemistry*, vol. 2020, Article ID 7468651, 11 pages, 2020.
- [25] Y. Li, W. Tang, Y. Chen, J. Liu, and C.-f. F. Lee, "Potential of acetone-butanol-ethanol (ABE) as a biofuel," *Fuel*, vol. 242, pp. 673–686, 2019.
- [26] K. Wei, Y. Yang, H. Zuo, and D. Zhong, "A review on ice detection technology and ice elimination technology for wind turbine," *Wind Energy*, 2019.
- [27] X. Zhao, J. E. Z. Zhang et al., "A review on heat enhancement in thermal energy conversion and management using field synergy principle," *Applied Energy*, vol. 257, Article ID 113995, 2020.
- [28] S. Akhtar, J. C. Kurnia, and T. Shamim, "A three-dimensional computational model of H₂-air premixed combustion in non-circular micro-channels for a thermo-photovoltaic (TPV) application," *Applied Energy*, vol. 152, no. 1, pp. 47–57, 2015.
- [29] W. M. Yang, S. K. Chou, K. J. Chua, J. Li, and X. Zhao, "Research on modular micro combustor-radiator with and without porous media," *Chemical Engineering Journal*, vol. 168, no. 2, pp. 799–802, 2011.
- [30] W. M. Yang, K. J. Chua, J. F. Pan, D. Y. Jiang, and H. An, "Development of micro-thermophotovoltaic power generator with heat recuperation," *Energy Conversion and Management*, vol. 78, no. 78, pp. 81–87, 2014.
- [31] W. Yang, D. Jiang, C. K. Y. Kenny, Z. Dan, and J. Pan, "Combustion process and entropy generation in a novel microcombustor with a block insert," *Chemical Engineering Journal*, vol. 274, no. 3, pp. 231–237, 2015.
- [32] D. Jiang, W. Yang, K. J. Chua, and J. Ouyang, "Thermal performance of micro-combustors with baffles for thermophotovoltaic system," *Applied Thermal Engineering*, vol. 61, no. 2, pp. 670–677, 2013.

- [33] D. Jiang, W. Yang, and A. Tang, "Development of a high-temperature and high-uniformity micro planar combustor for thermophotovoltaics application," *Energy Conversion and Management*, vol. 103, pp. 359–365, 2015.
- [34] A. Tang, J. Pan, W. Yang, Y. Xu, and Z. Hou, "Numerical study of premixed hydrogen/air combustion in a micro planar combustor with parallel separating plates," *International Journal of Hydrogen Energy*, vol. 40, no. 5, pp. 2396–2403, 2015.
- [35] Y. Su, Q. Cheng, J. Song, and M. Si, "Numerical study on a multiple-channel micro combustor for a micro-thermophotovoltaic system," *Energy Conversion & Management*, vol. 120, pp. 197–205, 2016.
- [36] S. Chen, "Analysis of entropy generation in counter-flow premixed hydrogen-air combustion," *International Journal of Hydrogen Energy*, vol. 35, no. 3, pp. 1401–1411, 2010.
- [37] S. Chen, H. Han, Z. Liu, J. Li, and C. Zheng, "Analysis of entropy generation in non-premixed hydrogen versus heated air counter-flow combustion," *International Journal of Hydrogen Energy*, vol. 35, no. 10, pp. 4736–4746, 2010.
- [38] S. Chen, Z. Liu, J. Liu, J. Li, L. Wang, and C. Zheng, "Analysis of entropy generation in hydrogen-enriched ultra-lean counter-flow methane-air non-premixed combustion," *International Journal of Hydrogen Energy*, vol. 35, no. 22, pp. 12491–12501, 2010.
- [39] A. Emadi and M. D. Emami, "Analysis of entropy generation in a hydrogen-enriched turbulent non-premixed flame," *International Journal of Hydrogen Energy*, vol. 38, no. 14, pp. 5961–5973, 2013.
- [40] A. Datta, "Effects of gravity on structure and entropy generation of confined laminar diffusion flames," *International Journal of Thermal Sciences*, vol. 44, no. 5, pp. 429–440, 2005.
- [41] H. Ban, S. Venkatesh, and K. Saito, "Convection-diffusion controlled laminar micro flames," *Journal of Heat Transfer*, vol. 116, no. 4, pp. 954–959, 1994.
- [42] P. R. Resende, M. Ayoobi, and A. M. Afonso, "Numerical investigations of micro-scale diffusion combustion: a brief review," *Applied Sciences*, vol. 9, no. 16, p. 3356, 2019.
- [43] J. E. X. Zhao, W. Zuo, Z. Zhang, and M. Pham, "Numerical investigation on the combustion characteristics of non-premixed hydrogen-air in a novel micro-combustor," *Applied Thermal Engineering*, vol. 110, pp. 665–677, 2017.
- [44] J. E. M. Zhao, Q. Zuo, B. Zhang, Z. Zhang, Q. Peng et al., "Effects analysis on diesel soot continuous regeneration performance of a rotary microwave-assisted regeneration diesel particulate filter," *Fuel*, vol. 260, pp. 116–353, 2019.
- [45] J. E. X. Zhao, G. Liu, B. Zhang, Q. Zuo, K. Wei et al., "Effects analysis on optimal microwave energy consumption in the heating process of composite regeneration for the diesel particulate filter," *Applied Energy*, vol. 254, pp. 113–736, 2019.
- [46] C. H. Kuo and P. D. Ronney, "Numerical modeling of non-adiabatic heat-recirculating combustors," *Proceedings of the Combustion Institute*, vol. 31, no. 2, pp. 3277–3284, 2007.

Research Article

Effect of Acetone-*n*-Butanol-Ethanol (ABE) as an Oxygenate on Combustion, Performance, and Emission Characteristics of a Spark Ignition Engine

Gang Wu,¹ Deng Wu,¹ Yuelin Li,¹ and Lei Meng^{1,2} 

¹College of Automotive and Mechanical Engineering, Changsha University of Science and Technology, Changsha 410114, China

²School of Automation, Wuhan University of Technology, Wuhan 430070, China

Correspondence should be addressed to Lei Meng; menglei1986@gmail.com

Received 25 September 2019; Accepted 11 December 2019; Published 6 January 2020

Guest Editor: Dezhi Zhou

Copyright © 2020 Gang Wu et al. This is an open access article distributed under the Creative Commons Attribution License, which permits unrestricted use, distribution, and reproduction in any medium, provided the original work is properly cited.

Ethanol is the most extensively used oxygenate for spark ignition (SI) engines. In comparison with ethanol, *n*-butanol exhibits a number of desirable properties for use in SI engines, which has proved to be a very promising oxygenated alternative fuel in recent years. However, the dehydration and recovery of bio-*n*-butanol consume extra money and energy in the acetone-*n*-butanol-ethanol (ABE) fermentation process. Hence, we focus on the research of ABE as a potential oxygenated alternative fuel in SI engines. The combustion, performance, and emission characteristics of B30, E30, ABE30 (i.e., 30 vol.% *n*-butanol, ethanol, and ABE blended with 70 vol.% gasoline), and G100 (pure gasoline) were compared in this study. The comparison results between B30, E30, and ABE30 at stoichiometric conditions show that ABE30 presents retarded combustion phasing, higher brake thermal efficiency, lower CO emissions, higher UHC emissions, and similar NO_x emissions. In comparison with G100 under various engine loads and equivalence ratios, for the most part, ABE30 exhibits 1.4% higher brake thermal efficiency, 14% lower carbon monoxide, 9.7% lower unburned hydrocarbons, and 23.4% lower nitrogen oxides. It is indicated that ABE could be served as the oxygenate in spark ignition engine due to its capability to improve energy efficiency and reduce pollutant emissions.

1. Introduction

Depleting fuel resources and increasing environmental problems have driven the use of alternative fuel in engine [1–4]. Meanwhile, due to the demand of increasing gasoline octane, oxygenated alternative fuel including methyl tertiary butyl ether (MTBE), methanol, ethanol, and *n*-butanol have been investigated in spark ignition (SI) engines [5, 6]. Pouloupoulos and Philippopoulos [7] tested the effects of MTBE-gasoline blends on the performance and emissions of a four-cylinder OPEL 1.6l SI engine. Based on the emissions before and after three-way catalytic converter (TWC), it was found that the addition of MTBE decreased the emissions of hazardous exhaust gases, carbon monoxide (CO) and hydrocarbon (HC), only at high engine loading. Liu et al. [8] performed a study of SI engine fueled with methanol-gasoline fuel blends. Results showed that CO, HC, and nitrogen oxide (NO_x) emissions

changed little before the TWC, and the conversion efficiencies of HC, CO, and NO_x emissions after the TWC are improved.

Ethanol is proposed as a replacement of MTBE and methanol in order to avoid gas station leakage and ground water pollution [9]. Hsieh et al. [10] conducted an experimental research on the performance and emission of an SI engine fueled with ethanol-gasoline blends based on the test of ethanol-gasoline blends with various blended ratios (0 vol.%, 5 vol.%, 10 vol.%, 20 vol.%, and 30 vol.%). When using ethanol, torque output and energy resource consumption increase and CO and HC emissions decrease dramatically, while the change of NO_x emission does not depend on the ethanol content. Celik [11] investigated the suitable blend ratio of ethanol in gasoline with high compression rate for SI engine. It was seen that engine power increased by 29%, and the specific fuel consumption rate, and CO, carbon dioxide (CO₂), NO_x, and HC combustion gas effluents were

decreased by 3%, 53%, 10%, 19%, and 12%, respectively, when using 50 vol.% blend ratio compared with pure gasoline.

Compared with ethanol, *n*-butanol has numbers of desirable properties as a fuel substitute of SI engines. Butanol is less prone to water contamination, and thus it could be distributed using the same infrastructure used to transport gasoline. Additionally, butanol also has lower latent heat, vapor pressure, higher heating value, octane, etc. [12]. The emission characteristics of an SI engine fueled with *n*-butanol-gasoline blends in combination with EGR were investigated by Gu et al. [13]. The addition of butanol to gasoline resulted in the decreasing engine's specific CO, HC, and NO_x combustion gas effluents. A study on the combustion characteristics of *n*-butanol in an SI engine was carried out by Szwaja and Naber [14]. The parameters of mass fraction burned (MFB), 0–10% MFB combustion duration, 10–90% MFB combustion duration, and 50% MFB location were calculated to quantitatively analyze the combustion properties. *n*-Butanol showed a shorter 0–10% MFB combustion duration, causing the shift of 50% MFB location towards top dead center (TDC). Meanwhile, *n*-butanol presented a higher combustion stability compared with gasoline from the viewpoint of coefficient of variation (COV).

n-Butanol belongs to the second-generation biofuels since it can be extracted from renewable sources, such as core fiber, wheat straw, distillers dry grains, corn stover, switchgrass, barely straw, and other plant materials [15–17]. *n*-Butanol is generally derived from acetone-*n*-butanol-ethanol (ABE) fermentation. However, due to low production efficiency, high hydration, and recovery cost during the fermentation process, *n*-butanol is currently less competitive in cost. Therefore, it is proposed that the intermediate fermentation outcome, i.e., ABE, is used for alternative fuel.

The combustion and emissions performance of water-containing ABE-diesel blends were studied by Chang et al. [18]. When using the blend of 20 vol.% ABE, 0.5 vol.% water, and 79.5 vol.% diesel (referred to as ABE20W0.5), brake thermal efficiency (BTE) was not only improved, but discharge of particular matter (PM), NO_x, polycyclic aromatic hydrocarbons (PAHs), and toxic equivalent of PAH (BaP_{eq}) were also reduced. Water-containing ABE-biodiesel-diesel blends were used to solve the problem of the increase of NO_x due to the use of biodiesel [19]. The addition of water-containing ABE in biodiesel-diesel blend synchronously reduced PM and NO_x emissions by 4.30–30.7% and 10.9–63.1%, respectively. Lee's group did a lot of research experiments on ABE-diesel blends to test their spray and combustion properties [20–24]. The combustion duration of ABE-diesel blends is shorter, and the natural flame luminosity is lower in comparison with diesel, which indicated ABE-diesel blends had potential advantages of improving energy efficiency and reducing soot emission in engine. His group also tested the impacts of factors such as blend ratio, mixture formulation, and water addition on ABE-gasoline blends performance and emissions [25–27]. A phenomenological soot model considering the oxidation effect on soot

density was proposed for ABE by Zhao et al. [28]. Luo et al. [29] used a wick-fed burner to evaluate soot tendency of ABE-diesel blends according to three parameters including flame height, threshold sooting index (TSI), and oxygen-extended sooting index (OESI). Results showed that the high H/C ratio and oxygen content of ethanol and *n*-butanol had a positive effect on reducing soot emission, while unsaturation degree of acetone had a negative effect. A multi-component evaporation model was built to accurately predict the evaporation evolution of ABE-diesel blends, and the model was validated by the experimental results of droplet fiber suspension evaporation [30]. Van Geem et al. [31] proposed mechanisms of action involving 350 species and over 10,000 reactions, which explained the pyrolysis and oxidation processes of ABE in detail. The mechanism is proved to be feasible and valid based on the comparison between calculated and experimental laminar flame speed. Zhang et al. [32] based on the analysis of chemical kinetics, stretch effect, and laminar flame speed under various component ratios and equivalence ratios. It was seen the laminar flame speed followed the order of ABE (6:3:1) < ABE (3:6:1) < ABE (1:6:3), and ethanol or *n*-butanol had a positive effect on burning velocity enhancement of ABE, while acetone had a negative effect.

As mentioned above, the previous research indicates ABE could be a potential substitute for engine fuel. However, there are few reports on the investigation of SI engine fueled by ABE-gasoline blends. Therefore, the experimental comparisons of the combustion, performance, and emission characteristics between E30, B30, ABE30 (i.e., 30 vol.% ethanol, butanol and ABE blended with gasoline, respectively), and G100 (pure gasoline) were conducted in this study.

2. Experimental Methods

2.1. Fuel Preparation. The commercial gasoline with a research octane number (RON) of 92 was chosen as baseline fuel in the study. The ABE mixture was generated by stirring analytical grade acetone (99.5%), *n*-butanol (99.5%), and ethanol (99.8%) using a temperature-controlled magnetic stirrer. The volume ratio of the mixture was set as A : B : E of 3 : 6 : 1 which is the representative composition proportion of ABE fermentation products. The various parameters of each component in the mixture are listed in Table 1 [33–36]. The stability of the mixture was examined through a gravity test, where the mixture was stored in tubes for 14 days at 25°C and 1 atm. The fuels showed a distinct single phase during the whole stability measurement process.

2.2. Engine Setup. Figure 1 shows the schematic diagram of the engine setup for the experiment. A port fuel-injected single cylinder SI engine is combined with a GE type TLC-15 class 4-35-1700 dynamometer, which can absorb loads up to 26 kW at speeds of 4500 rpm. The engine specifications are shown in Table 2. A Kistler-type 6125B pressure sensor was used to detect cylinder pressure, which was recorded by a LabVIEW code. The average in-cylinder pressures from 50

TABLE 1: Properties of test fuels [33–36].

Parameters	Gasoline	Acetone	Butanol	Ethanol
Chemical formula	$C_4 \sim C_{12}$	C_3H_6O	C_4H_9OH	C_2H_5OH
Lower heating value (MJ/kg)	43.4	29.6	33.1	26.8
Density (kg/m^3)	715~765	790	810	790
Energy density (kJ/m^3)	32.20	23.38	26.81	21.17
Octane number	90	—	87	100
Oxygen content (wt.%)	—	27.6	21.6	34.8
Boiling temperature ($^{\circ}C$)	25–215	56.2	118	78
Latent heat of vaporation ($25^{\circ}C$) (kJ/kg)	380~500	518	716	904
Self-ignition temperature ($^{\circ}C$)	~300	465	343	420
Stoichiometric AFR	14.7	9.0	11.2	9.0
Saturation pressure at $38^{\circ}C$ (kPa)	62~90	53.4	2.27	13.8
Laminar flame speed (cm/s)	~33 ^A	~34 ^B	~48 ^C	~48 ^C

Note: ^A $p = 1 \text{ atm}$, $T = 325 \text{ K}$; ^B $p = 1 \text{ atm}$, $T = 298 \text{ K}$; ^C $p = 1 \text{ atm}$, $T = 343 \text{ K}$.

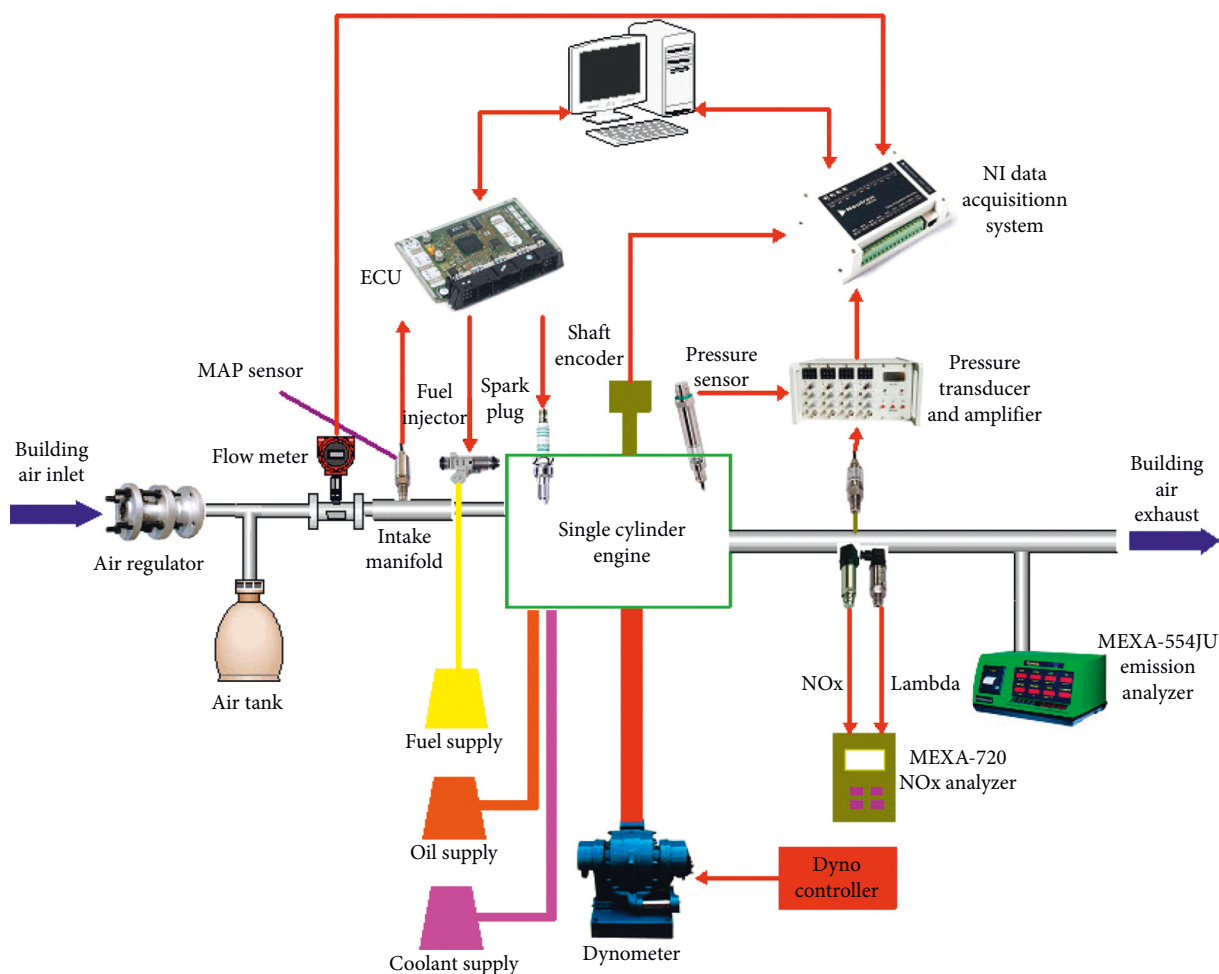


FIGURE 1: Engine setup.

cycles were calculated at each test point. BEI XH25D shaft encoder was used to measure the crank angle location. The Megasquirt V3.0 Engine Control Unit (ECU) was used for engine control. The dynamometer is dominated by a DYN-LOC controller. The engine throttle location was adjusted by DyneSystems DTC-1 digital throttle controller. Air/fuel ratio (AFR) and NO_x emission were detected by Horiba MEXA-720 analyzer. UHC and CO emissions were detected

by Horiba MEXA-554JU analyzer. The intake air system provided compressed, filtered air from the building to the engine. The flow of air from the building supply system was controlled by an electronic regulator which provided pressure control; from which the air flowed through a surge tank and then into the intake manifold. An intake air temperature sensor and a manifold absolute pressure (MAP) sensor were mounted at the intake manifold directly to

TABLE 2: Engine specifications.

Engine type	SI engine
Displaced volume (cm ³)	575
Stroke (mm)	90.1
Bore (mm)	90.3
Connecting rod length (mm)	150.7
Compression ratio	9.6:1
Number of valves	4
Number of cylinders	1

measure intake air temperature and pressure. The air then flowed through a throttle body where the throttle valve was controlled with a throttle position sensor. From there, the air was mixed with the injected fuel and flowed into the engine via the intake valves. A Bosch fuel injector rated at 440 cm³/min was used at a fuel pressure of 3 bar. The measuring range, accuracy and resolution of experimental apparatus are shown in Table 3.

2.3. Test Conditions. The engine rotational velocity was set at a fixed value of 1200 rpm in this research. The throttle plate was adjusted to be fully open and the intake manifold pressure was fixed at 60 kPa and 90 kPa by regulating the compressed air supply, which corresponded to engine loads of 3 bar BMEP (brake mean effective pressure) and 5 bar BMEP. The intake air pressure was controlled using an electronic regulator which provides precise control. Meanwhile, the equivalence ratio was varied over a range of lean, stoichiometric and rich conditions, i.e., lambda varying from 1.2 to 0.8. In a practical SI engine operating condition, equivalence ratio is not uniform and varies in each individual cylinder on a cycle-by-cycle basis. For example, it is advantageous to use lean condition for best efficiency at part-load operation and rich condition for maximum power at full-load operation. Therefore, the equivalence ratio in this study was varied over a range of lean, stoichiometric, and rich conditions, i.e., Φ ranging from 0.83 to 1.25. In this study, the maximum brake torque (MBT) timing of gasoline was chosen as spark timing. The measured UHC, CO, and pollution gas temperature were directly recorded from the emissions analyzer, while the measured values of engine torque, lambda, and NO_x were averaged within 60-second period. The experiments were conducted three times, and each group of data was collected for one day. The average of these datasets was then calculated. The tests were performed on three consecutive days in a temperature-controlled laboratory, so the effects of humidity were assumed to be negligible. Furthermore, the engine was allowed to run at every operating condition for an extended period of time to ensure steady state measurements. The test conditions mentioned above are summarized in Table 4.

3. Results and Discussion

3.1. Comparison between E30, B30, and ABE30 under Stoichiometric Condition. Figure 2 compares the combustion characteristics of E30, B30, and ABE30 at $\Phi = 1$ and 3 bar BMEP. It can be seen from Figure 2(a) that E30 showed a

TABLE 3: Measuring range, accuracy, and resolution of the experimental apparatus.

Apparatus	Measuring range	Accuracy (\pm)	Resolution
Engine speed	1–5000 rpm	0.2%	1 rpm
Torque	0–300 Nm	0.5%	0.1 Nm
Exhaust gas temperature	0–900°C	1°C	0.1°C
CO emission	0–10% vol	0.06%	0.01% vol
HC emission	0–10000 ppm-vol	12 ppm-vol	1 ppm-vol
CO ₂ emission	0–20% vol	0.5%	0.01% vol
NO _x emission	0–3000 ppm	3%	1 ppm
Lambda	0.65–13.7	0.3%	0.01
Mass flow meter	0–1000 slpm	1%	0.1 slpm

TABLE 4: Test conditions.

Throttle position (%)	100
Engine speed (rpm)	1200
Load (bar BMEP)	3 and 5
Lambda	0.8–1.2
Fuel pressure (bar)	3
Spark timing	Gasoline's MBT at $\Phi = 1$

more advanced combustion phasing, resulting in the highest peak cylinder pressure. To further evaluate the combustion phasing of different fuels, normalized mass fraction burnt (MFB) shown in Figure 2(b) was calculated from pressure trace using Rassweiler and Withrow method [37, 38]. Based on MFB profiles, initial combustion duration (ICD) given by 0–10% MFB, major combustion duration (MCD) given by 10–90% MFB, and 50% MFB location were obtained as shown in Figure 2(c). During the ICD, the combustion rate was mainly impacted by laminar flame speed (LFS) [14, 39]. Based on the highest LFS, E30 obtained the 2.0% and 4.1% shorter ICD compared with B30 and ABE30. In addition, it should be noted that ethanol had the same LFS with butanol (see Table 1), but got the shorter ICD probably due to fuel volatility. It was known that the latent heat of vaporization and vapor pressure were two important thermodynamic properties that affect fuel volatility [40]. Vapor pressure was an important property affecting the volatility of a fuel. The vapor pressure of butanol was much lower than that of ethanol, which meant that butanol needed a higher temperature or longer time to get completely vaporized [41]. Moreover, the higher oxygen content of ethanol was beneficial to improve combustion rate due to chemical affect. The MCD of the fuels followed a similar sequence with the ICD. The higher pressure built during the period of ICD promoted the mixing of fuel and air due to the increase in turbulence and improved the combustion rate in the following flame propagation. Based on the shorter ICD and MCD, E30 got the 0.5 CA and 0.81 CA advanced 50% MFB location when compared to B30 and ABE30.

Figure 3 compares the engine performance of E30, B30, and ABE30, including BTE and BSFC at $\Phi = 1$ and 3 bar BMEP. The BTE indicates how well an engine can convert the heat in fuel to mechanical energy. From Figure 3(a), the

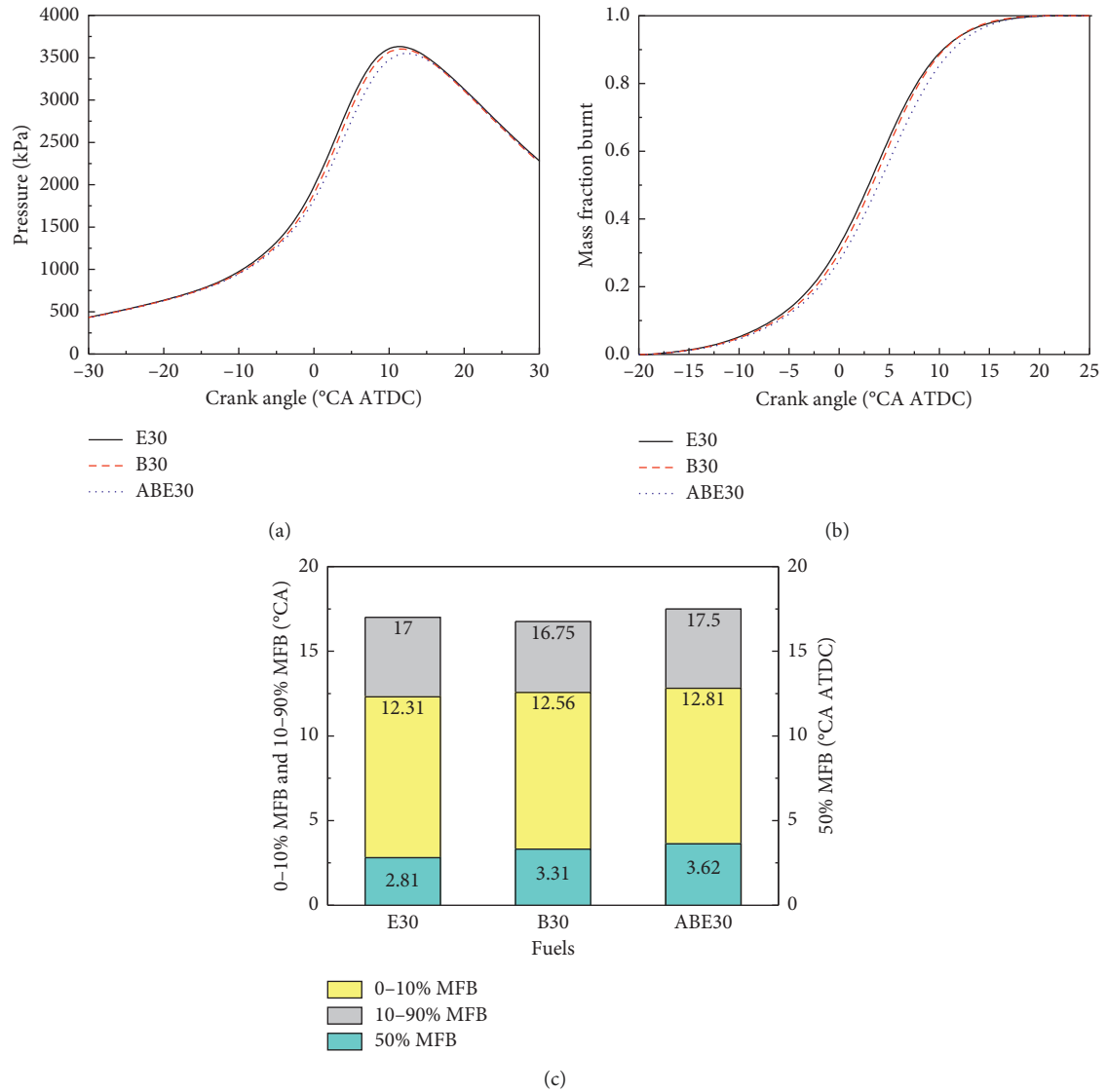


FIGURE 2: Combustion characteristics of E30, B30, and ABE30 at 3 bar BMEP under stoichiometric condition.

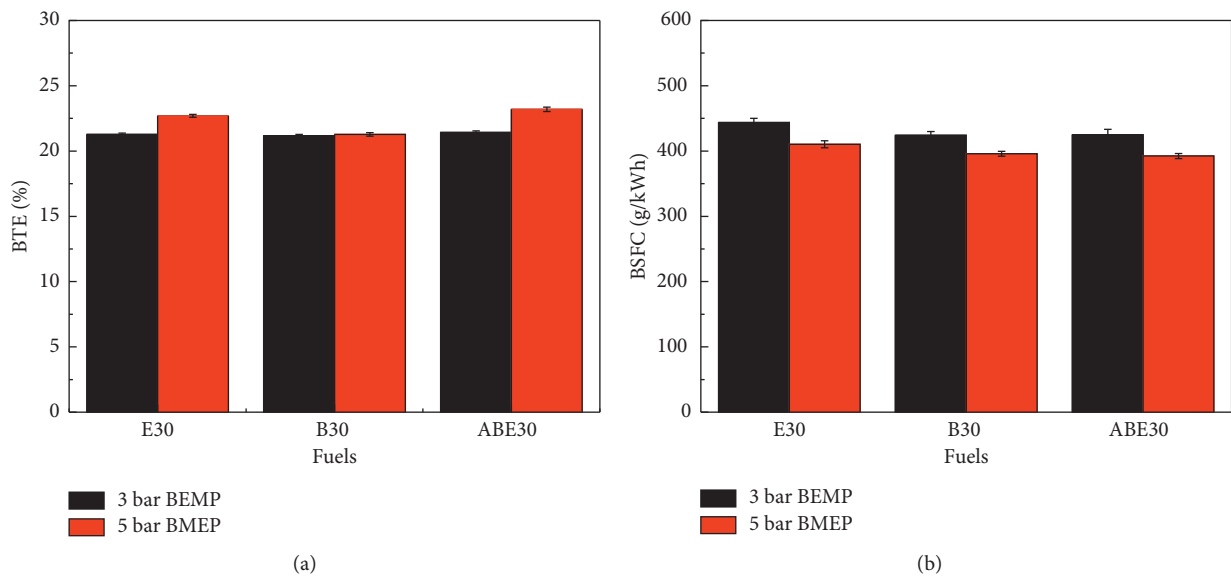


FIGURE 3: Engine performance of E30, B30, and ABE30 at 3 and 5 bar BMEP under stoichiometric condition.

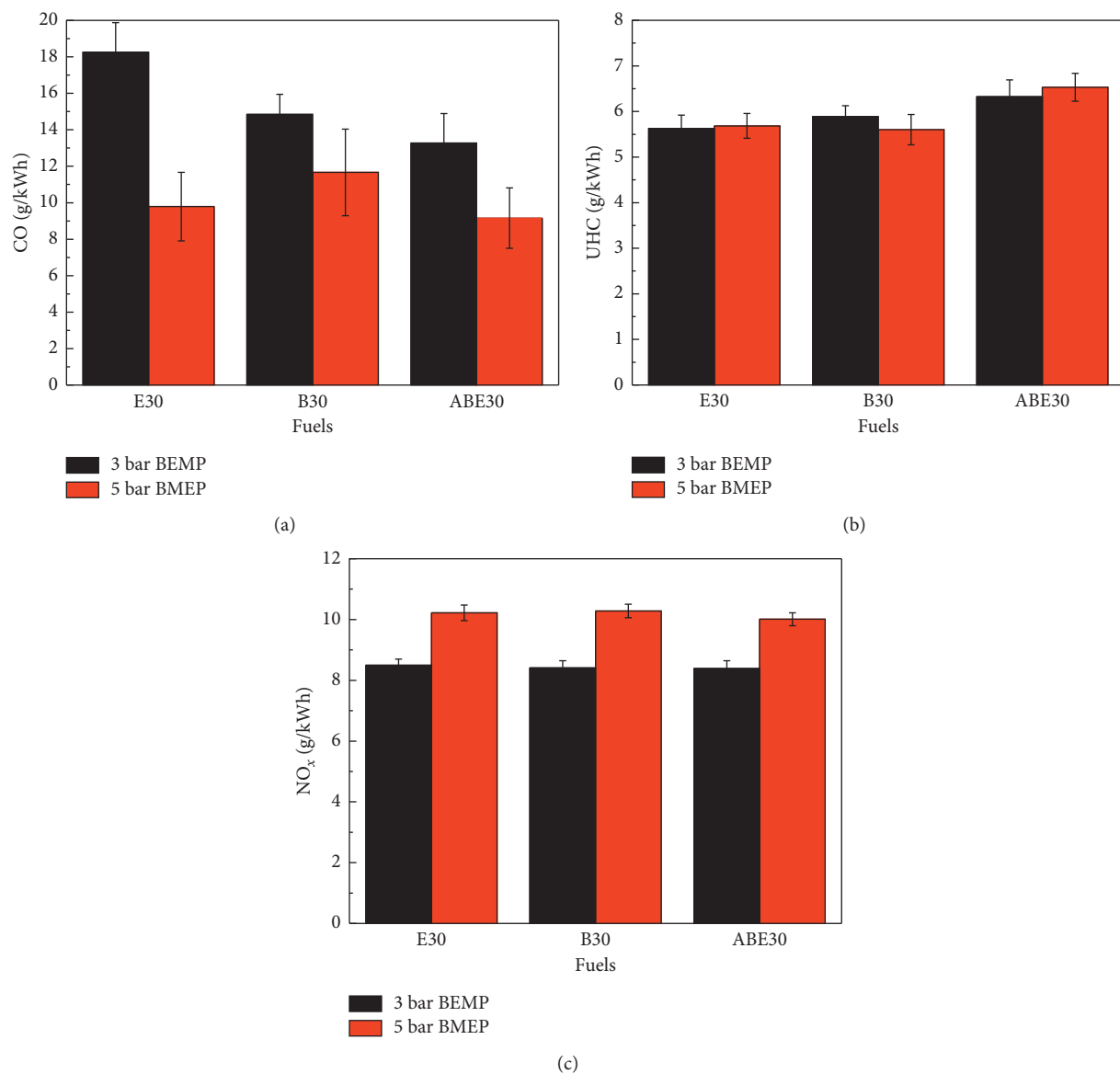


FIGURE 4: Engine emissions of E30, B30, and ABE30 at 3 and 5 bar BMEP under stoichiometric condition.

results showed that ABE30 had 0.7% and 1.1% higher BTE than that of E30 and B30, respectively. This can be explained that the advanced combustion phasing after adding ethanol and butanol led to the subsequent increase of work lost in compression process and decrease of net useful work when spark timing was set to gasoline's MBT [42, 43]. For the BSFC, ethanol showed the maximum value due to its lower energy density. In addition, it can be seen that the engine had a relatively high fuel consumption, which is due to the high friction owing to it being a single-cylinder engine; it could also be caused by carbon deposition in the engine, or aging of the sparkplug.

Figure 4 shows the CO, UHC, and NO_x emissions of E30, B30, and ABE30 at $\Phi = 1$ and 3 bar BMEP. A higher CO emission occurred for E30. Generally, a higher CO emission level can be caused by the conditions of locally rich, insufficient oxidizer, or low combustion temperature. After

adding fuel oxygenates, the lack of oxygen should not lead to the increased CO emission. Previous studies explained that the fuel producing more products in terms of heat capacity of the combustion products can lower combustion temperature and further slow down the oxidation process of CO emission [44, 45]. The stoichiometric chemical reactions of acetone, ethanol, and *n*-butanol are listed equation (1). Moreover, E30 had a shorter combustion duration, and thus insufficient oxidation of CO could also cause the increased CO emission. UHC emission was mainly influenced by the combustion quality. The higher oxygen content in E30 was beneficial to improve combustion quality, resulting in a lower UHC emission compared to B30 and ABE30. Zeldovich thermal activation was the predominate mechanism for NO_x emission formation from internal combustion engines. The higher combustion temperature and local oxygen concentration in the peak temperature zone were in

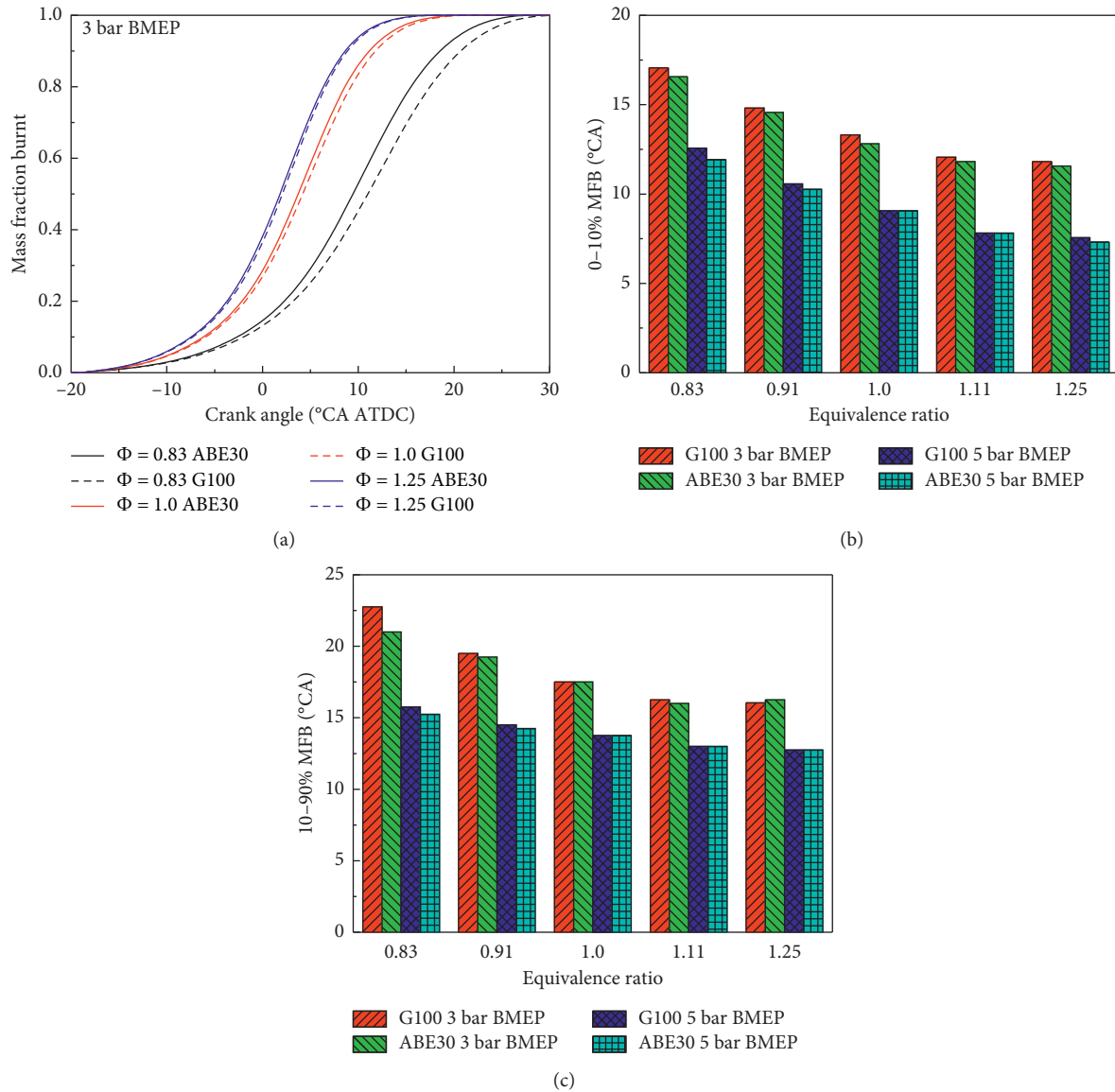
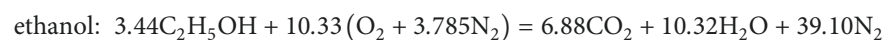
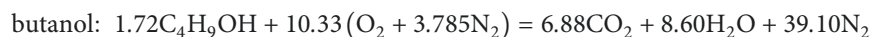


FIGURE 5: Combustion characteristics of ABE30 and G100 under various engine loads and equivalence ratios.

favor of NO_x emission formation [46]. By using fuel oxygenates, an increased oxygen concentration was caused due to fuel self-provided oxygen, but a lower combustion

temperature could also be resulted. Based on the competition between the factors, the similar NO_x was finally obtained by E30, B30, and ABE30.



3.2. Comparison between G100 and ABE30 under Various Engine Loads and Equivalence Ratios. In this section, the performance, combustion, and emission characteristics of ABE30 and G100 were compared under different equivalence ratios ($\Phi = 0.83 \sim 1.25$) and engine loads (3 and 5 bar BMEP). It was apparent that the ICD and MCD were

reduced with increasing equivalence ratios and engine loads. A higher cylinder temperature was achieved at 5 bar BMEP, which led to a faster combustion rate. Gauthier et al. [47] discovered that when the equivalence ratio increased, the ICD decreased. A similar trend was also obtained in Figure 5(b). A similar trend was also obtained in Figure 5(b).

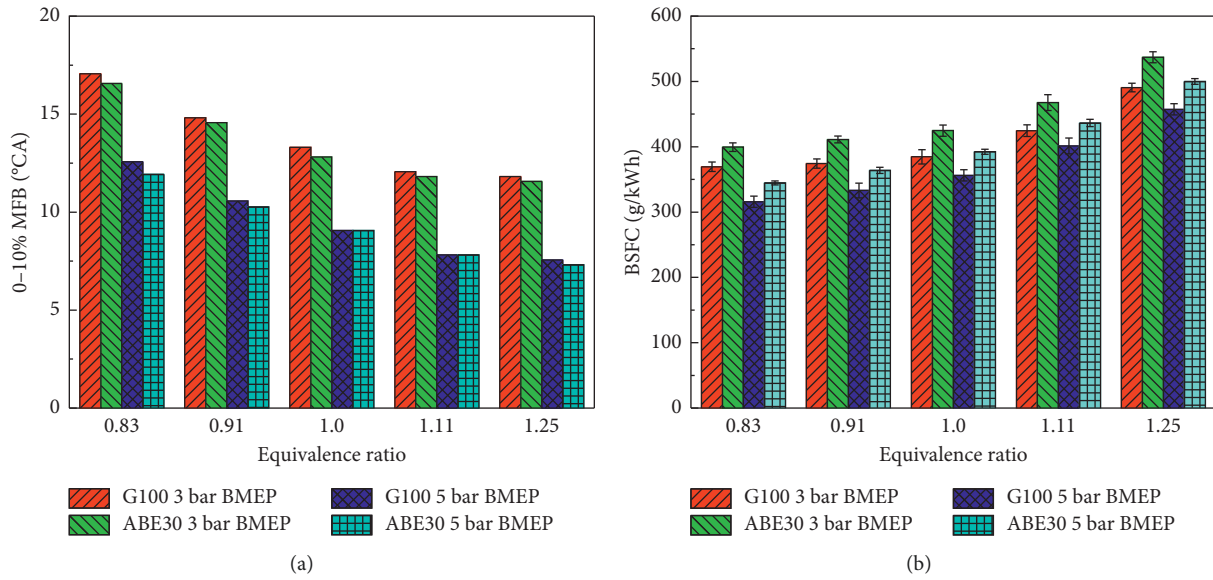


FIGURE 6: Engine performance of ABE30 and G100 under various engine loads and equivalence ratios.

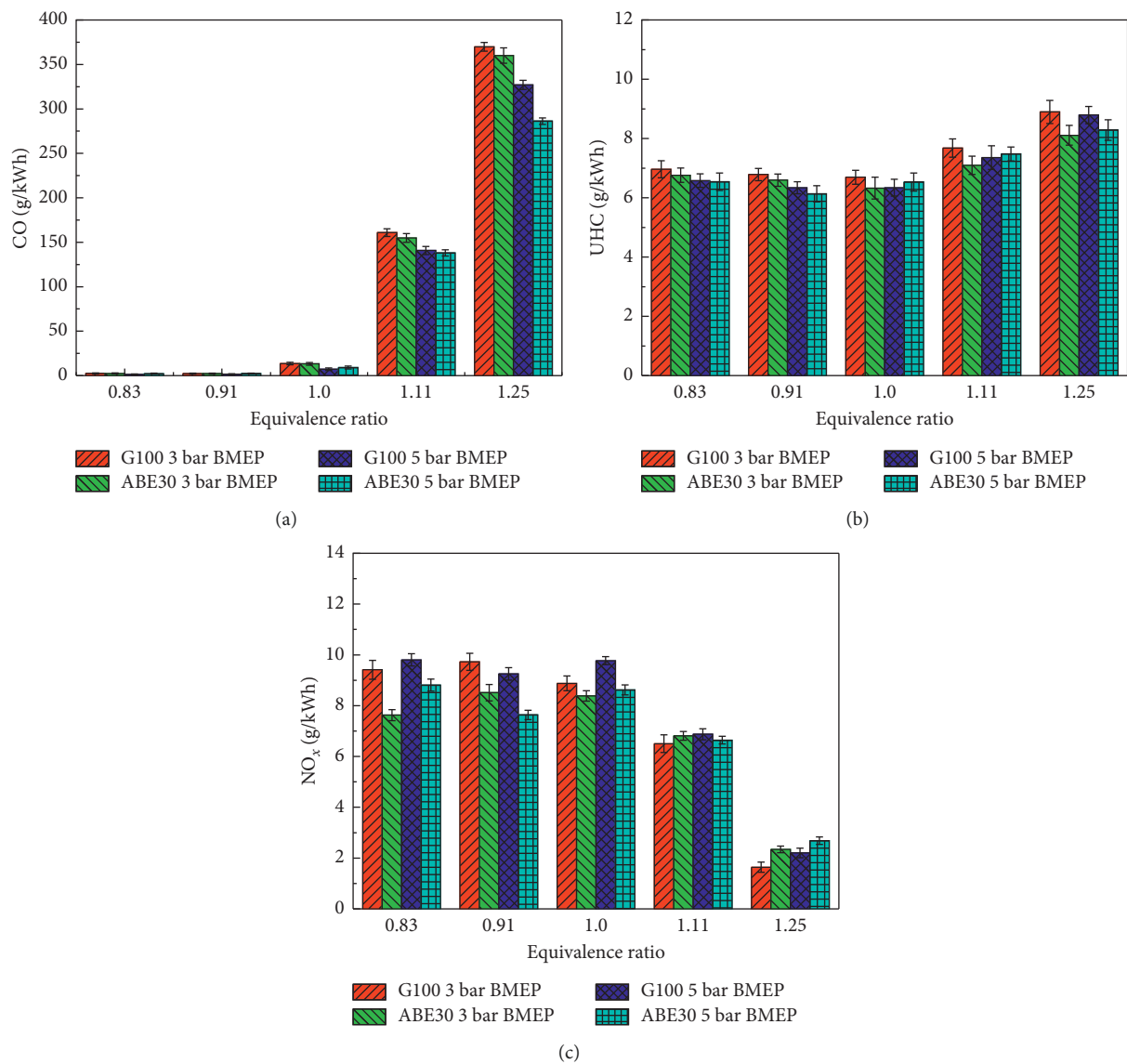


FIGURE 7: Engine emissions of ABE30 and G100 under various engine loads and equivalence ratios.

In addition, with the increases of equivalence ratios and engine loads, the differences of ICD and MCD between ABE30 and G100 were reduced. These trends were consistent with those of [47, 48]. In general, compared with G100, ABE30 had a more advanced combustion phasing with 1.7–3.9% shorter ICD and 1.2–8.3% shorter MCD.

Figure 6 shows the BTE and BSFC of ABE30 and G100 with respect to equivalence ratio and engine load. The BTE increased with decreasing equivalence ratio and increasing engine load. That was based on the fact that combustion was not complete in the rich conditions. With the further decrease of equivalence ratio, increased dilution improved isentropic efficiency by decreasing heat loss and increasing adiabatic exponent due to the lower temperatures than that in stoichiometric conditions [49]. The higher cylinder temperature at 5 bar BMEP resulted in the improved combustion quality and higher BTE than that at 3 bar BMEP. For the BTE, ABE30 increased BTE by 0.2–1.4% compared with G100 due to the improved combustion quality and shorter combustion duration, and apparent increase occurred at lean conditions. This could be explained that the combustion phasing of fuels was retarded at lean conditions, but the engine was still running at gasoline's MBT at stoichiometric condition, and thus the advanced combustion phasing of ABE30 was more suitable as shown in Figure 5(a), and the side effect of improper combustion phasing of ABE at stoichiometric and rich conditions was avoided. Due to the improved BTE, the BSFC of fuels was decreased with decreasing equivalence ratio and increasing engine load. Based on the lower energy density, ABE30 showed 8.1–10.4% higher BSFC than that of G100.

Figure 7 shows the variations of CO, UHC, and NO_x emissions with equivalence ratio and engine load for ABE30 and G100. It was observed that the equivalence ratio controlled CO emission until lean conditions were reached, and after that CO emission did not vary significantly. This low CO emission under lean condition can be explained by the fact that there was more than enough oxygen available to carry on the oxidation process [48]. In addition, the lower CO emission and higher NO_x were attained in the higher engine load due to the higher cylinder temperature. When compared with G100, ABE30 produced the 1.3–14% lower CO and 0.5–9.7% lower UHC emissions due to the improved combustion quality as a result of fuel-borne oxygen. UHC emission increased for rich conditions because of incomplete combustion as the combustion quality deteriorates. In comparison with G100, although an increased oxygen concentration was provided, a decreased combustion temperature was also caused as mentioned above so that the final 3.4–23.4% lower NO_x emission was produced at lean and stoichiometric conditions for ABE30. It was also observed that ABE30 presented a higher NO_x emission compared with G100 at $\Phi = 1.25$. It probably resulted from the fuel-rich prompt mechanism of NO_x emission formation, which meant more hydrocarbon radicals generated from ABE30 due to the lower molecular weight and more injected amounts of fuel increased the formation of HCN and led to the higher NO_x emission [46].

4. Conclusions

This study investigates the potential of ABE-gasoline blend as a green fuel for SI engines. The comparisons of combustion, performance, and emission characteristics between E30, B30, ABE30, and G100 are analyzed.

The comparisons between E30, B30, and ABE30 at stoichiometric condition show that E30 and B30 had a more advanced combustion, causing the lower BTE than that of ABE30. The significant increase of CO and UHC emissions occurred for E30 and ABE30, respectively. A similar NO_x was obtained by E30, B30, and ABE30.

ABE30 was further compared with G100 under various equivalence ratios and engine loads. ABE30 had a generally advanced combustion phasing, and the difference of combustion phasing between ABE30 and G100 was decreased with increasing equivalence ratio and engine load. For engine performance and emissions, compared with G100, the higher BTE (0.2–1.4%) and the lower CO (1.3–14%), UHC (0.5–9.7%) and NO_x (3.4–23.4%) emissions were observed for ABE30 in some conditions.

Nomenclature

ABE:	Acetone- <i>n</i> -butanol-ethanol
SI:	Spark ignition
ATDC:	After top dead center
BMEP:	Brake mean effective pressure
Φ :	Equivalence ratio
RON:	Research octane number
BSFC:	Brake-specific fuel consumption
PM:	Particular matter
MTBE:	Methyl tertiary butyl ether
ICD:	Initial combustion duration
BTE:	Brake thermal efficiency
ECU:	Engine control unit
MFB:	Mass fraction burned
UHC:	Unburned hydrocarbons
CO:	Carbon monoxide
NO _x :	Nitrogen oxides
COV:	Coefficient of variation
PAHs:	Polycyclic aromatic hydrocarbons
CO ₂ :	Carbon dioxide
MCD:	Major combustion duration.

Data Availability

All data used to support the findings of this study are included within the article.

Conflicts of Interest

The authors declare that they have no conflicts of interest regarding the publication of this paper.

Acknowledgments

This work was supported by the National Natural Science Foundation of China (grant nos. 51976016 and 61903287). The authors also thank the Open Research Subject of State

Key Laboratory of Engines, China, (grant no. K2018-07), and the Research Foundation of Education Bureau of Hunan Province (grant no. 18B149) for their support.

References

- [1] M. F. Othman, A. Adam, G. Najafi, and R. Mamat, "Green fuel as alternative fuel for diesel engine: a review," *Renewable and Sustainable Energy Reviews*, vol. 80, pp. 694–709, 2017.
- [2] E. Jiaqiang, M. Zhao, Q. Zuo et al., "Effects analysis on diesel soot continuous regeneration performance of a rotary microwave-assisted regeneration diesel particulate filter," *Fuel*, vol. 260, Article ID 116353, 2019, In press.
- [3] E. Jiaqiang, M. Zhao, G. Liu et al., "Effects analysis on optimal microwave energy consumption in the heating process of composite regeneration for the diesel particulate filter," *Applied Energy*, vol. 254, Article ID 113736, 2019.
- [4] E. Jiaqiang, G. Liu, Z. Zhang et al., "Effect analysis on cold starting performance enhancement of a diesel engine fueled with biodiesel fuel based on an improved thermodynamic model," *Applied Energy*, vol. 243, pp. 321–335, 2019.
- [5] Y. Li, W. Tang, Y. Chen, J. Liu, and C.-f. F. Lee, "Potential of acetone-butanol-ethanol (ABE) as a biofuel," *Fuel*, vol. 242, pp. 673–686, 2019.
- [6] X. Zhao, E. Jiaqiang, Z. Zhang et al., "A review on heat enhancement in thermal energy conversion and management using field synergy principle," *Applied Energy*, vol. 257, Article ID 113995, 2019, In press.
- [7] S. Pouloupoulos and C. Philippopoulos, "Influence of MTBE addition into gasoline on automotive exhaust emissions," *Atmospheric Environment*, vol. 34, no. 28, pp. 4781–4786, 2000.
- [8] S. Liu, E. R. Cuty Clemente, T. Hu, and Y. Wei, "Study of spark ignition engine fueled with methanol/gasoline fuel blends," *Applied Thermal Engineering*, vol. 27, no. 11-12, pp. 1904–1910, 2007.
- [9] R. K. Niven, "Ethanol in gasoline: environmental impacts and sustainability review article," *Renewable and Sustainable Energy Reviews*, vol. 9, no. 6, pp. 535–555, 2005.
- [10] W.-D. Hsieh, R.-H. Chen, T.-L. Wu, and T.-H. Lin, "Engine performance and pollutant emission of an SI engine using ethanol-gasoline blended fuels," *Atmospheric Environment*, vol. 36, no. 3, pp. 403–410, 2002.
- [11] M. B. Celik, "Experimental determination of suitable ethanol-gasoline blend rate at high compression ratio for gasoline engine," *Applied Thermal Engineering*, vol. 28, no. 5-6, pp. 396–404, 2008.
- [12] P. Dürre, "Biobutanol: an attractive biofuel," *Biotechnology Journal*, vol. 2, no. 12, pp. 1525–1534, 2007.
- [13] X. Gu, Z. Huang, J. Cai, J. Gong, X. Wu, and C.-f. Lee, "Emission characteristics of a spark-ignition engine fuelled with gasoline-*n*-butanol blends in combination with EGR," *Fuel*, vol. 93, pp. 611–617, 2012.
- [14] S. Szwaja and J. D. Naber, "Combustion of *n*-butanol in a spark-ignition IC engine," *Fuel*, vol. 89, no. 7, pp. 1573–1582, 2010.
- [15] M. Kumar and K. Gayen, "Developments in biobutanol production: new insights," *Applied Energy*, vol. 88, no. 6, pp. 1999–2012, 2011.
- [16] C.-L. Cheng, P.-Y. Che, B.-Y. Chen, W.-J. Lee, C.-Y. Lin, and J.-S. Chang, "Biobutanol production from agricultural waste by an acclimated mixed bacterial microflora," *Applied Energy*, vol. 100, pp. 3–9, 2012.
- [17] A. Ranjan, S. Khanna, and V. S. Moholkar, "Feasibility of rice straw as alternate substrate for biobutanol production," *Applied Energy*, vol. 103, pp. 32–38, 2013.
- [18] Y.-C. Chang, W.-J. Lee, S.-L. Lin, and L.-C. Wang, "Green energy: water-containing acetone-butanol-ethanol diesel blends fueled in diesel engines," *Applied Energy*, vol. 109, pp. 182–191, 2013.
- [19] Y.-C. Chang, W.-J. Lee, T. S. Wu, C.-Y. Wu, and S.-J. Chen, "Use of water containing acetone-butanol-ethanol for NO_x-PM (nitrogen oxide-particulate matter) trade-off in the diesel engine fueled with biodiesel," *Energy*, vol. 64, pp. 678–687, 2014.
- [20] N. Zhou, M. Huo, H. Wu, K. Nithyanandan, C.-f. F. Lee, and Q. Wang, "Low temperature spray combustion of acetone-butanol-ethanol (ABE) and diesel blends," *Applied Energy*, vol. 117, pp. 104–115, 2014.
- [21] H. Wu, K. Nithyanandan, N. Zhou, T. H. Lee, C.-f. F. Lee, and C. Zhang, "Impacts of acetone on the spray combustion of acetone-butanol-ethanol (ABE)-diesel blends under low ambient temperature," *Fuel*, vol. 142, pp. 109–116, 2015.
- [22] H. Wu, K. Nithyanandan, T. H. Lee, C.-f. F. Lee, and C. Zhang, "Spray and combustion characteristics of neat acetone-butanol-ethanol, *n*-butanol, and diesel in a constant volume chamber," *Energy & Fuels*, vol. 28, no. 10, pp. 6380–6391, 2014.
- [23] H. Wu, K. Nithyanandan, J. Zhang et al., "Impacts of acetone-butanol-ethanol (ABE) ratio on spray and combustion characteristics of ABE-diesel blends," *Applied Energy*, vol. 149, pp. 367–378, 2015.
- [24] H. Wu, T. H. Lee, C.-f. Lee, F. Liu, and B. Sun, "Optical soot measurement of bio-butanol upstream product, ABE (acetone-butanol-ethanol), under diesel-like conditions," *Fuel*, vol. 181, pp. 300–309, 2016.
- [25] K. Nithyanandan, H. Wu, M. Huo, and C. F. Lee, "A preliminary investigation of the performance and emissions of a port-fuel injected SI engine fueled with acetone-butanol-ethanol (ABE) and gasoline," in *Proceedings of the SAE 2014 World Congress & Exhibition*, Detroit, MI, USA, April 2014.
- [26] Y. Li, K. Nithyanandan, T. H. Lee et al., "Effect of water-containing acetone-butanol-ethanol gasoline blends on combustion, performance, and emissions characteristics of a spark-ignition engine," *Energy Conversion and Management*, vol. 117, pp. 21–30, 2016.
- [27] Y. Li, L. Meng, K. Nithyanandan et al., "Experimental investigation of a spark ignition engine fueled with acetone-butanol-ethanol and gasoline blends," *Energy*, vol. 121, pp. 43–54, 2017.
- [28] Z. Zhao, H. Wu, M. Wang et al., "Computational investigation of oxygen concentration effects on a soot mechanism with a phenomenological soot model of acetone-butanol-ethanol (ABE)," *Energy & Fuels*, vol. 29, no. 3, pp. 1710–1721, 2015.
- [29] J. Luo, Y. Zhang, Q. Zhang, J. Liu, and J. Wang, "Evaluation of sooting tendency of acetone-butanol-ethanol (ABE) fuels blended with diesel fuel," *Fuel*, vol. 209, pp. 394–401, 2017.
- [30] X. Ma, F. Zhang, K. Han, and G. Song, "Numerical modeling of acetone-butanol-ethanol and diesel blends droplet evaporation process," *Fuel*, vol. 174, pp. 206–215, 2016.
- [31] K. M. Van Geem, A. Cuoci, A. Frassoldati, S. P. Pyl, G. B. Marin, and E. Ranzi, "An experimental and kinetic modeling study of pyrolysis and combustion of acetone-butanol-ethanol (ABE) mixtures," *Combustion Science and Technology*, vol. 184, no. 7-8, pp. 942–955, 2012.
- [32] S. Zhang, T. H. Lee, H. Wu, J. Pei, W. Wu, and F. Liu, "Experimental and kinetical study of component volumetric

- effects on laminar flame speed of acetone-butanol-ethanol (ABE),” *Energy & Fuels*, vol. 32, no. 5, pp. 6278–6292, 2018.
- [33] L. A. Graham, S. L. Belisle, and C.-L. Baas, “Emissions from light duty gasoline vehicles operating on low blend ethanol gasoline and E85,” *Atmospheric Environment*, vol. 42, no. 19, pp. 4498–4516, 2008.
- [34] P. S. Veloo, Y. L. Wang, F. N. Egolopoulos, and C. K. Westbrook, “A comparative experimental and computational study of methanol, ethanol, and *n*-butanol flames,” *Combustion and Flame*, vol. 157, no. 10, pp. 1989–2004, 2010.
- [35] C. T. Chong and S. Hochgreb, “Measurements of laminar flame speeds of acetone/methane/air mixtures,” *Combustion and Flame*, vol. 158, no. 3, pp. 490–500, 2011.
- [36] T. Wallner, A. Ickes, and K. Lawyer, “Analytical assessment of C2-C8 alcohols as spark-ignition engine fuels,” in *Proceedings of the FISITA 2012 World Automotive Congress*, pp. 15–26, Beijing, China, November 2012.
- [37] Y. Li, L. Meng, K. Nithyanandan et al., “Combustion, performance and emissions characteristics of a spark-ignition engine fueled with isopropanol-*n*-butanol-ethanol and gasoline blends,” *Fuel*, vol. 184, pp. 864–872, 2016.
- [38] Y. Li, Y. Chen, G. Wu, C.-f. F. Lee, and J. Liu, “Experimental comparison of acetone-*n*-butanol-ethanol (ABE) and isopropanol-*n*-butanol-ethanol (IBE) as fuel candidate in spark-ignition engine,” *Applied Thermal Engineering*, vol. 133, pp. 179–187, 2018.
- [39] G. Wu, Z. Lu, W. Pan, Y. Guan, S. Li, and C. Z. Ji, “Experimental demonstration of mitigating self-excited combustion oscillations using an electrical heater,” *Applied Energy*, vol. 239, pp. 331–342, 2019.
- [40] K. Key, T. Last, C. Haywood, and R. Raine, “Measurement of vapor pressures and enthalpies of vaporization of gasoline and ethanol blends and their effects on mixture preparation in an SI engine,” *SAE International Journal of Fuels & Lubricants*, vol. 1, no. 1, pp. 132–144, 2008.
- [41] J. Zhang, K. Nithyanandan, Y. Li, C. F. Lee, and Z. Huang, “Comparative study of high-alcohol-content gasoline blends in an SI engine,” in *Proceedings of the SAE 2015 World Congress & Exhibition*, Detroit, MI, USA, April 2015.
- [42] K. Nithyanandan, J. Zhang, Y. Li et al., “Improved SI engine efficiency using acetone-butanol-ethanol (ABE),” *Fuel*, vol. 174, pp. 333–343, 2016.
- [43] G. Wu, Z. Lu, X. Xu et al., “Numerical investigation of aeroacoustics damping performance of a Helmholtz resonator: effects of geometry, grazing and bias flow,” *Aerospace Science and Technology*, vol. 86, pp. 191–203, 2019.
- [44] T. Topgül, H. S. Yücesu, C. Ç. ces, and A. Koca, “The effects of ethanol-unleaded gasoline blends and ignition timing on engine performance and exhaust emissions,” *Renewable Energy*, vol. 31, no. 15, pp. 2534–2542, 2006.
- [45] M. Canakci, A. N. Ozsezen, E. Alptekin, and M. Eyidogan, “Impact of alcohol-gasoline fuel blends on the exhaust emission of an SI engine,” *Renewable Energy*, vol. 52, pp. 111–117, 2013.
- [46] B. M. Masum, H. H. Masjuki, M. A. Kalam, I. M. Rizwanul Fattah, S. M. Palash, and M. J. Abedin, “Effect of ethanol-gasoline blend on NO_x emission in SI engine,” *Renewable and Sustainable Energy Reviews*, vol. 24, pp. 209–222, 2013.
- [47] B. M. Gauthier, D. F. Davidson, and R. K. Hanson, “Shock tube determination of ignition delay times in full-blend and surrogate fuel mixtures,” *Combustion and Flame*, vol. 139, no. 4, pp. 300–311, 2004.
- [48] J. B. Heywood, *Internal Combustion Engine Fundamentals*, Mcgraw-Hill Education, New York, NY, USA, 1988.
- [49] D. Dunn-Rankin, *Lean Combustion: Technology and Control*, Academic Press, Cambridge, MA, USA, 2011.

Research Article

Numerical Investigation of the Combustion in an Improved Microcombustion Chamber with Rib

Hai Chen  and Wei-qiang Liu

College of Aerospace Science and Engineering, National University of Defense Technology, Changsha 410073, China

Correspondence should be addressed to Hai Chen; chfair@163.com

Received 26 July 2019; Revised 27 September 2019; Accepted 12 October 2019; Published 22 November 2019

Guest Editor: Jiaqiang E

Copyright © 2019 Hai Chen and Wei-qiang Liu. This is an open access article distributed under the Creative Commons Attribution License, which permits unrestricted use, distribution, and reproduction in any medium, provided the original work is properly cited.

This study proposes an improved microcombustor with a rectangular rib to improve the temperature level of the combustor wall. Moreover, the OH mass fraction, temperature distribution, and outer wall temperature of the original and improved combustors of premixed hydrogen/air flames are numerically investigated under various inlet velocities and equivalence ratios. Results show that the improved microcombustor enhances heat transfer between the mixture and wall because its recirculation zone is larger than that of the original, thereby resulting in high wall temperature. Conversely, thermal resistance in the horizontal direction increases with upstream and downstream step lengths. Consequently, the outer wall temperature decreases with step length in the improved combustor. A high equivalence ratio (e.g., 0.6) may result in the destruction of the combustor because the wall temperature has exceeded the acceptable temperature of wall material quartz. Therefore, the improved microcombustor is recommended for micro-thermo-photovoltaic systems.

1. Introduction

Micro-electro-mechanical system (MEMS) technology has received considerable attention in recent years [1–3]. Micro-power generation devices based on combustion has several advantages, such as light weight, high-power density, long charge duration, and short recharging time [4–6]. Thus, micro-power generation devices are deemed suitable alternatives to conventional batteries. Moreover, these devices can be applied in micro fuel cells, micro gas turbines, and micro-thermo-electric, and thermo-photovoltaic systems [7, 8].

A micro-thermophotovoltaic (TPV) system geometry consists of photovoltaic cells, emitter, filter, and heat source (Figure 1). A microcombustor is a core part of the micro-TPV system, in which the chemical energy of the fuel is converted into other energy through combustion. Hence, research on microcombustor with a large operation range has received increasing attention. However, the short residence time of mixtures and high heat loss due to the high surface area-to-volume ratio of the microcombustor result

in flame instability and low blow-off limit [9–11]. Therefore, enhancing flame stability and extending the operating range present significant issues. By using structure design to form a low-velocity zone or recirculation zone, the flame stability and combustion performance of the microcombustor can be improved.

Peng et al. [12] numerically examined the thermal performance of a microcombustion chamber with and without a front cavity and found that the front cavity enhances the stability of the microcombustor. Wan et al. [13–16] numerically investigated the behavior of an H₂/air blend in a microcombustion chamber with cavities and found that recirculation and low-velocity zones are formed in the concave cavity. The flame is unstable in the combustor without cavities but can be effectively stabilized in a combustor with cavities. These cavities can also expand the working range of the inlet velocity. Bagheri et al. [17] numerically studied the combustion characteristics of premixed hydrogen/air in microcombustors with different bluff body structures (e.g., semicircular, ellipse, half ellipse, wall-blade, and arrowhead) at different inlet velocities and found

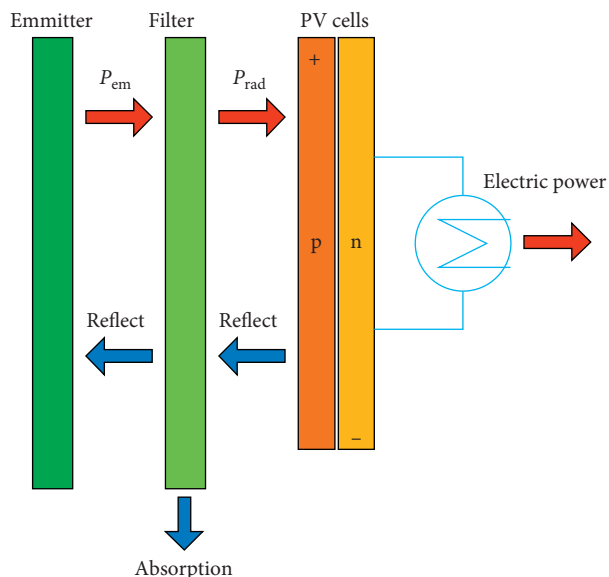


FIGURE 1: Energy conversion process of a micro-thermophotovoltaic (TPV) system.

that the combustion chamber with a wall fin as a bluff body shows the highest flame temperature and emission efficiency when the inlet velocity is 10 m/s. Jiaqiang et al. [18] established a methane/air premixed combustion model in a microcombustor and found that the combustion performance is improved at a 45° backward-facing step angle, a quartz wall material, an inlet velocity ranging from 2 m/s to 4 m/s, and a high field synergy. Zuo et al. [19] proposed a microcylindrical combustion chamber with a rib and numerically investigated the behavior of microcombustors. They found that the outer wall temperature of the improved combustion chamber is higher and more uniform than that of the microcombustion chamber without a rib. Wan et al. [20] designed a microcombustor with a flat flame stabilizer and two preheating channels and found that the blowout limit of the combustor initially increases and then decreases along with an increasing plate length. Jiaqiang et al. [21] found that the inlet pipe structure of the combustor improves the mixing performance of H_2/O_2 and enhances flame stabilization and heat recirculation by using a backward-facing step and cavity. Yilmaz et al. [22, 23] established a combined structure of cavity, poststage, and microchannel in a combustor and then studied its combustion characteristics. They found that the average wall temperature, wall temperature distribution, and combustion efficiency of the new combustor have been significantly improved. Zuo et al. [24] designed a counterflow double-channel microcombustion chamber in which the inner diameter of the combustor gradually increases. They found that the improved combustor has a more uniform and a much higher wall temperature compared with the combustor with a backward-facing step. Yan et al. [25] numerically analyzed the behavior of methane/air in a microcombustion chamber with a regular triangular pyramid bluff body and found that the blow-off limit of the improved microcombustor is nearly twice larger than that of the original microcombustor. Ansari and

Amani [26] numerically examined a novel planar microcombustion chamber with a combined bluff and baffle structure for micro-TPV systems and found that this new combustor outperforms a combustor with only one baffle or cylinder in terms of flame stability and combustion efficiency. Li et al. [27] numerically studied the effects of channel height and inlet velocity on combustion characteristics in a 2D planar microcombustion chamber with a separating plate and found that the mixing effect can be improved by reducing the inlet velocity and channel height. Tang et al. [28] numerically and experimentally studied the propane/air premixed combustion performance of a new cross-plate microplanar combustor and found that the cross-plate enhances the heat transfer and increases the average wall temperature by more than 90 K. The new structure also extended the blowout limit of the cross-plate combustor. Zuo et al. [29] found that the efficiency and emission power of the microelliptical combustor are 2.17% and 0.68 W higher than those of the microcircular tube combustor when the long axis-short axis ratio and hydrogen mass flow rate are 1.9/1.18 and 7×10^{-7} kg/s, respectively. Akhtar et al. [30] found that the outer wall temperature of the curved groove combustor increases by 110 K and that the energy conversion rate increases by 7.84% compared with the straight groove. Aravind et al. [31] proposed a three-backward-facing-step microcombustion chamber with a recirculation hole and added a porous medium (ceramic cotton) to the combustion chamber. They found that the porous media preheat the mixture through a thermal cycle and that the flame stability is significantly improved.

The use of a catalyst on the surface of a microcombustion chamber can reduce the activation energy required for the ignition of mixed gas and improve the combustion efficiency and stability of the combustion chamber.

Li and Hong [32] added hydrogen to methane fuel by using a platinum tube with a perforated ring to improve the combustion stability and radiation intensity of the microthermoelectric system of the combustion chamber. They found that the effective power efficiency of the TPV system is 3.24%. Yan et al. [33] performed a numerical simulation of platinum catalytic combustion on a microplate combustor for methane/air catalytic combustion. They found that a low inlet velocity can increase methane conversion, but a high-temperature region can easily be formed near the inlet. Therefore, preheating the mixed gas by using a wall material with high thermal conductivity is necessary. Ran et al. [34] conducted numerical studies on the characteristics of methane catalytic combustion in a microcombustion chamber with a convex cavity and a combustion chamber without a cavity. The results showed that the methane conversion increases and then decreases with the increase in equivalence ratio. When the equivalence ratio equals 1, the conversion rate of methane in the convex wall cavity reaches the maximum at 85.3%. The convex cavity microcombustion chamber reaches the highest flameout limit at 16.5 m/s. Luo et al. [35] used the $Pd/Al_2O_3/Fe-Ni$ catalyst to perform catalytic combustion experiments on low-concentration methane in a microcombustion chamber; they analyzed the effects of flow rate, methane concentration, and burner

temperature on the methane conversion rate. The results showed that temperature is the most critical factor affecting conversion. Pan et al. [36] investigated the catalytic combustion process of premixed methane/air in a rectangular microcombustion chamber via experimentation. The outer wall temperature distribution and the main components of flue gas were measured separately. The results indicated that the addition of platinum to the microcombustion chamber significantly improves the combustion stability of the microchannel. After platinum is added to the combustion chamber, the outer wall temperature becomes further uniform and the methane conversion rate is increased. Rodrigues et al. [37] explored the methane/air catalytic combustion of microcombustion chambers with cobalt oxide (CO_3O_4) as coating. They found that methane is completely burned at a temperature of 760°C . When the temperature is lower than 600°C , only the catalytic reaction will occur in the combustion chamber. However, when the temperature is above 600°C , the combustion chamber will simultaneously produce the gas phase and catalytic combustion. Moreover, CO_3O_4 has remarkable application potential. Wang et al. [38] investigated the catalytic combustion of methane and *n*-butane in microtubes with Pt/ZSM-5 as the catalyst via experimentation. The results showed that the stable combustion range of *n*-butane is slightly higher than that of methane. When *n*-butane is used as fuel, the penetrating wall of the combustion chamber has a high heat loss rate and temperature. *n*-butane can be used as an alternative fuel to methane when necessary.

Although a combustor wall temperature level that is sufficiently high is desired for thermoelectric and thermophotovoltaic devices, such a level is difficult to achieve because heat loss increases substantially with the surface area-to-volume ratio of the microcombustor. Furthermore, the residence time of the mixture decreases when the combustion chamber is scaled down. Thus, cavities are included into a planar microcombustor [13–16]. Moreover, the effect of cavity geometry on combustion performance is evaluated. In contrast to previous studies, we improved a microcombustor through the application of a rib on the basis of the literature [13–16]. Thereafter, the current study numerically investigates the combustion performance of the improved microcombustor under various inlet velocities and equivalence ratios.

2. Mathematical-Physical Model of a Combustor

2.1. Physical Model of a Microcombustor. The schematic diagram of a ribless microcombustion chamber is presented in Figure 2. The cavity length (L_2) and total length (L_0) of the microcombustion chamber are 3.0 mm and 18.0 mm, respectively. The thickness of the combustion chamber walls (W_3) is 2 mm. The height (W_1) and width (W_0) of the combustor chamber are 1 mm and 10 mm, respectively. The depth (W_2) and length (L_1) of the cavities are 1 mm and 3 mm, respectively. In contrast to the original combustion chamber in Figure 2(a), a rib is added into the cavity, as shown in Figure 2(b). The rib width is 0.5mm. The rib

heights (H), upstream (L_3), and downstream (L_4) step lengths are various. The improved microcombustion chamber with various step lengths and rib heights are shown in Table 1.

2.2. Modeling Equations. The characteristic scale of the microcombustion chamber is substantially larger than the molecular mean-free path of blends. Therefore, the gas mixture is regarded as continuous [13–16].

Kuo and Ronney found that the realizable k-epsilon model is optimal in calculating the combustion performance compared with the laminar model because the Reynolds number is above or approximately 500 [39]. In this study, the Reynolds number exceeds 500 because the inlet velocity is either equal to or over 10 m/s in the improved combustor. In addition, the laminar finite rate model is optimal compared with the other model. Hence, this research adopts the realizable k-epsilon model and laminar finite rate model for the numerical simulation. Moreover, a two-dimensional steady-state model was employed because of the large aspect ratio ($W_0/W_1 = 10:1$) of the microcombustion chamber.

Continuity equation is given as follows:

$$\frac{\partial(\bar{v}_x + v'_x)}{\partial x} + \frac{\partial(\bar{v}_y + v'_y)}{\partial y} = 0. \quad (1)$$

The momentum equation is given as follows:

$$\frac{\partial(\rho\bar{v}_i\bar{v}_j)}{\partial x_j} = -\frac{\partial\bar{p}}{\partial x_i} + \frac{\partial}{\partial x_j} \left(\eta \frac{\partial\bar{u}_i}{\partial x_j} - \rho u'_i u'_j \right). \quad (2)$$

The energy equation is given as follows:

$$\begin{aligned} \frac{\partial(\rho v_x C_p T)}{\partial x} + \frac{\partial(\rho v_y C_p T)}{\partial y} &= \frac{\partial((\lambda_f + \lambda_{ft})\partial T)}{\partial x^2} \\ &+ \frac{\partial((\lambda_f + \lambda_{ft})\partial T)}{\partial y^2} + \sum_i \left[\frac{\partial}{\partial x} \left(C_{p,i} T \rho D_{m,i} \frac{\partial Y_i}{\partial x} \right) \right. \\ &\left. + \frac{\partial}{\partial y} \left(C_{p,i} T \rho D_{m,i} \frac{\partial Y_i}{\partial y} \right) \right] + \sum_i C_{p,i} T R_i. \end{aligned} \quad (3)$$

The species equation is given as follows:

$$\frac{\partial(\rho Y_i v_x)}{\partial x} + \frac{\partial(\rho Y_i v_y)}{\partial y} = \frac{\partial}{\partial x} \left(\rho D_{m,i} \frac{\partial Y_i}{\partial x} \right) + \frac{\partial}{\partial y} \left(\rho D_{m,i} \frac{\partial Y_i}{\partial y} \right) + R_i, \quad (4)$$

where $C_{p,i}$, R_i , and Y_i denote specific heat capacity, generation or consumption rate, and the mass fraction of species i , separately; while λ_{ft} and λ_f are turbulent thermal conductivity and thermal conductivity of the blends, separately.

2.3. Computation Scheme. The mass, momentum, energy, and species conservation equations are solved using Fluent. The density of the gas blends is calculated using the ideal gas assumption, while the specific heat is determined using the mixing law. Kinetic theory is used for the blend mass diffusivity, while the mass-weighted mixing law is adopted to calculate the

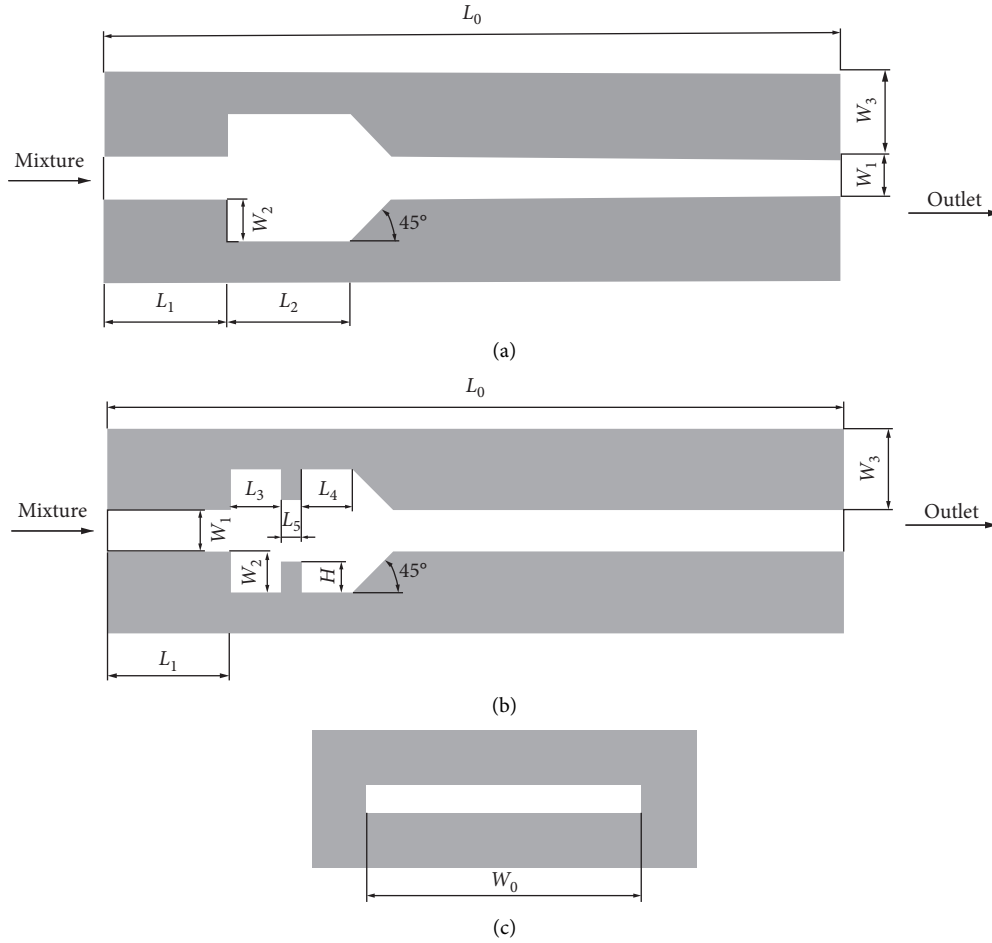


FIGURE 2: Schematic diagram of the microcombustor: (a) without rib, (b) with rib, and (c) combustor exit.

TABLE 1: The improved microcombustion chamber with various step lengths and rib heights.

	Upstream step lengths (L_3) (mm)	Downstream step lengths (L_4) (mm)	Rib heights (H) (mm)
Case A	1.25	1.25	0.75
Case B	2.25	1.25	0.75
Case C	3.25	1.25	0.75
Case D	1.25	2.25	0.75
Case E	1.25	3.25	0.75
Case F	1.25	1.25	0.25
Case G	1.25	1.25	0.55

thermal conductivity and viscosity of the gas mixture. The COUPLED algorithm and the second-order upwind scheme were selected to couple the pressure and velocity. “Temperature patches” of 2000 K and 1350 K on the fluid and solid zones, respectively, were used to ignite the H_2 /air mixture.

This study adopts the chemical kinetic mechanism of the H_2 reaction reported in Li et al. [40], which comprises 13 species and 19 reversible elementary reactions. Wan et al. [13–16] verified the chemical mechanism by simulating the combustion of H_2 /air. The simulated results were compared with the experimental results reported in the literature [41]. Accordingly, the numerical results are consistent with the experimental data.

The boundary conditions are as follows. The velocity condition was specified at the inlet, whereas the pressure outlet condition was adopted at the outlet. The nonslip boundary condition was adopted in the simulation. The inlet temperature of the microcombustor was fixed at 300 K. Quartz was used as the solid material. The specific heat capacity, density, and thermal conductivity of the quartz material were 750 J/kg/K, 2650 kg/m³, and 1.05 W/m/K, respectively.

The heat loss in the solid wall immensely influences the combustion. Therefore, the heat transfer in the channel walls is considered in the numerical simulation. The heat loss on the exterior surfaces includes radiation, while natural convection is computed as follows:

TABLE 2: Calculation results of the different grid spacings in the two-dimensional structure of a microcombustor.

Grid spacing (m)	Exhausted gas temperature (K)	Mean outer wall temperature (K)	Mass fraction of hydrogen at the outlet (%)
1×10^{-5}	1197.1	1037.5	0.001930354
2×10^{-5}	1197.01	1037.7	0.001931158
3.3×10^{-5}	1195.2	1041.5	0.002078265
4×10^{-5}	1195	1043.5	0.002161413

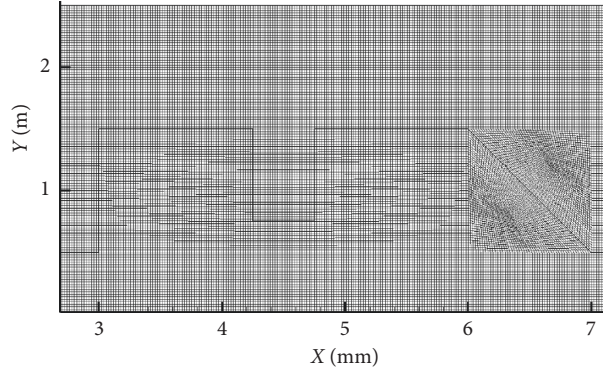


FIGURE 3: Demonstration of the grid system near the upper cavity.

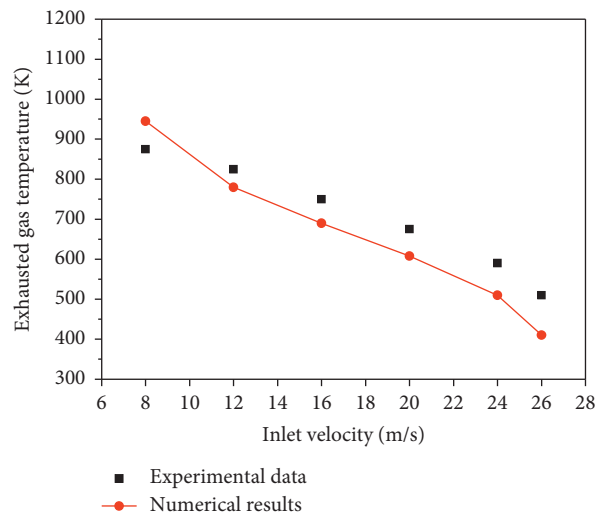


FIGURE 4: Comparison between experimental data and numerical results for exhaust gas temperature in the original microcombustor.

$$q = h_0(T_w - T_\infty) + \varepsilon\sigma(T_w^4 - T_\infty^4), \quad (5)$$

where h_0 is the natural convection heat transfer coefficient, $20 \text{ W}/(\text{m}^2\text{K})$, T_w is the exterior wall temperature, ε is the interior and exterior emissivity of solid surface with a value of 0.92, T_∞ is the ambient temperature (300 K), and σ is the Stephan–Boltzmann constant $5.67 \times 10^{-8} \text{ W}/\text{m}^2/\text{K}^4$.

2.4. Grid Independence. A grid correlation test was conducted with a two-dimensional model of the original microcombustion chamber under four mesh intervals: 1×10^{-5} , 2×10^{-5} , 3.3×10^{-5} , and 4×10^{-5} m, as shown in Table 2. The inlet velocity and equivalence ratios of the simulation case were equal to 10 m/s and 0.4, respectively; the heat transfer coefficient was $20 \text{ W}/\text{m}^2/\text{K}$; and the radiation emissivity of the outer wall was 0.92 [13–16]. The

results showed that the hydrogen at the outlet and temperature differences for the four-grid spacing were minimal. Furthermore, the difference was not obvious when grid spacing was equal to 1×10^{-5} and 2×10^{-5} m. Thus, the grid spacing of 2×10^{-5} m was deemed sufficient to achieve high accuracy in a short computation time for the numerical investigation. The numerical model of the microcombustor was meshed using approximately 227600 structured cells, as shown in Figure 3.

2.5. Model Verification. We compared the numerical results of the exhausted gas temperature on the original model with the experimental data in the literature [13–16], as shown in Figure 4. The results of the numerical model and the model in the literature [13–16] shared the same changing trend. The maximum temperature difference was 98 K. This result

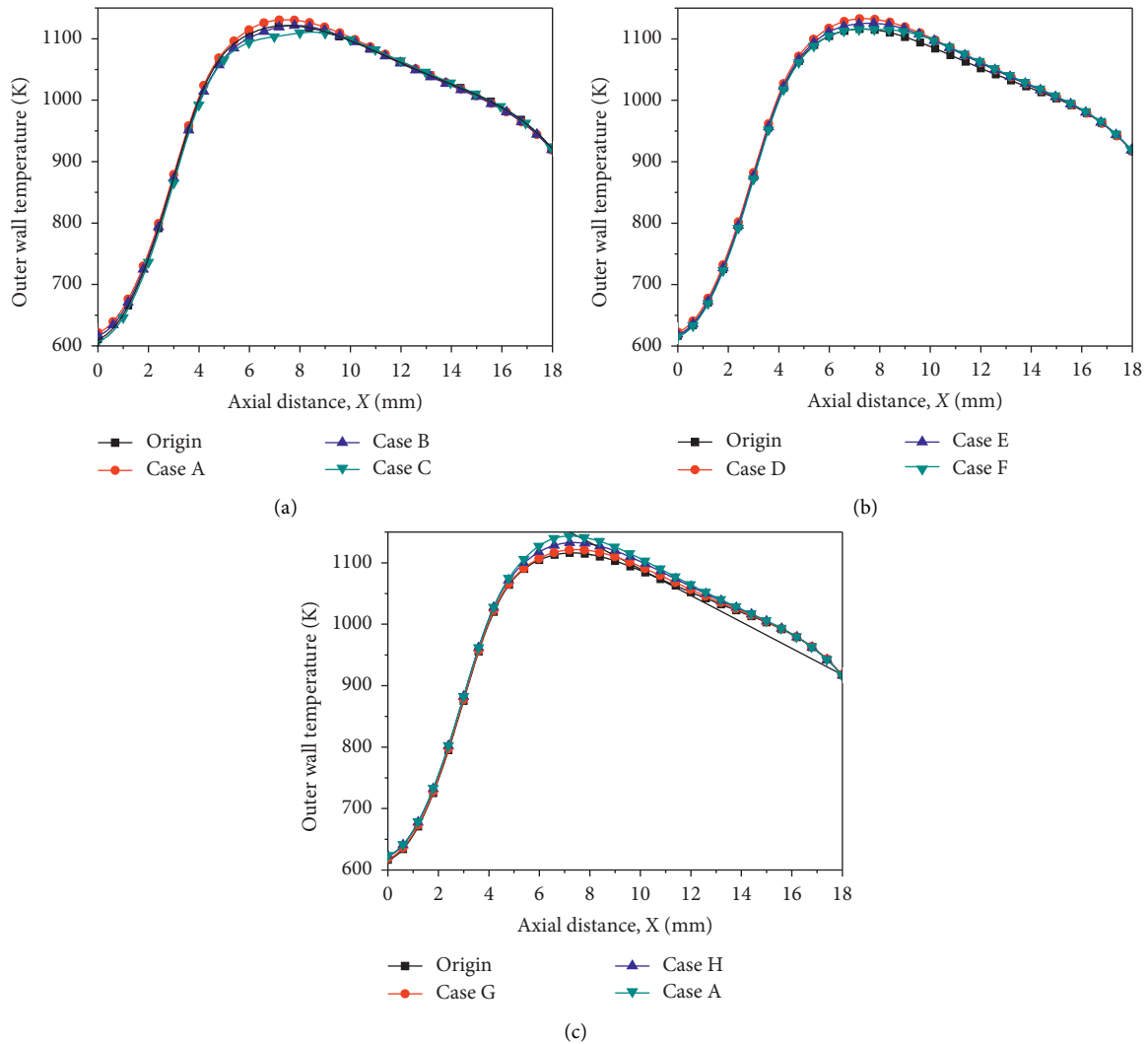


FIGURE 5: Outer wall temperature profiles for the original and improved combustor with inlet velocity equal to 10 m/s.

confirmed the numerical model is reliable to research the combustion performance in the microcombustion chamber.

3. Results and Discussions

3.1. Effects of Rib Position on Combustion Characteristics. We plot the outer wall temperature profiles for the different microcombustors (Figure 5). The lengths of the rib and upstream and downstream steps vary. This figure shows that the outer wall temperature profile increases from the inlet and reaches a peak around the center of the cavity. Thereafter, the temperature profile descends with further increase in the axis length because of heat losses from the outer wall. Figures 5(a) and 5(b) show that the outer wall temperature profile of the combustor becomes inverted against the upstream and downstream step lengths. This result is caused by an increase in the thermal resistance in the horizontal direction because of the thinning outer wall of the cavity. Hence, low heat is conducted upstream through the thin outer wall with a large right-step length. Moreover, the outer wall temperature level increases with an increase in the

rib height (Figure 5(c)). The newly proposed combustor has a higher wall temperature than that of the original.

The contours of the longitudinal velocity component near the cavities at inlet velocities of 10 m/s are presented in Figure 6 to clarify the mechanism by which the newly proposed combustor improves the wall temperature level. The equivalence ratio is maintained at 0.4. The region where the longitudinal velocity is below 0 is considered the recirculation zone, where as that where such a velocity is between 0 and 10 m/s is considered the low-velocity zone. Figure 6 shows that the recirculation zones of the microcombustion chamber with a rectangular rib are divided into two parts, in which the area of the recirculation zone of the microcombustion chamber with the rib is larger than that without the rib. This feature enhances heat transfer between the blends and inner walls, while the residence time of the mixture is also prolonged. Thus, the outer wall temperature of the improved combustor is higher than that of the original combustor. The recirculation zone area is nearly maintained because the upstream and downstream step lengths are approximately 2.25 mm.

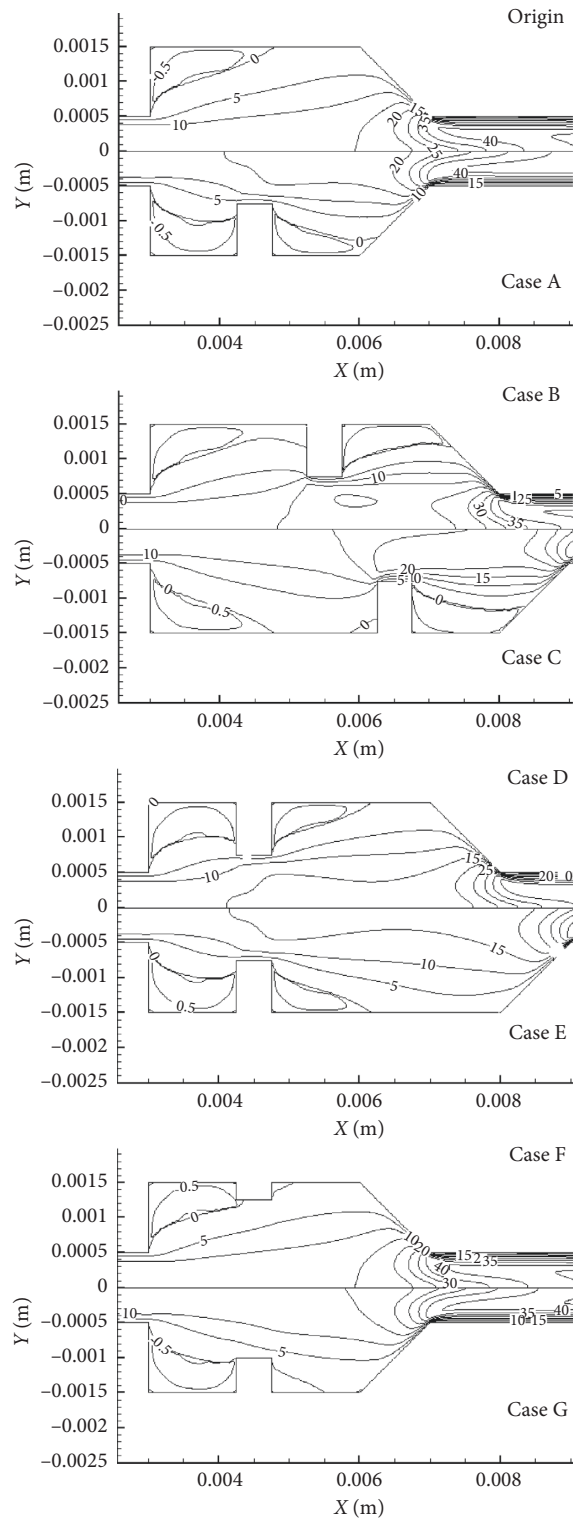


FIGURE 6: Contours of the longitudinal velocity component in the region near the cavities. The inlet velocity is 10 m/s.

Figure 7 presents the average wall temperatures of the different microcombustion chambers with and without the rib under different inlet velocities. Accordingly, the equivalence ratio is maintained at 0.4. Figures 7(a) and 7(b) show that the average wall temperature increases with the inlet velocity, which is below 32 m/s. The mean outer wall temperature decreases with the continuous increase in inlet

velocity because of the short residence time in the combustor. Among the studied microcombustors, the average wall temperature of the combustion chamber with $L_3 = 1.25$ mm and $L_4 = 1.25$ mm is the highest when the inlet velocity is kept constant. Given the increase in upstream and downstream step lengths, the corresponding mean outer wall temperature decreases owing to the increase in thermal

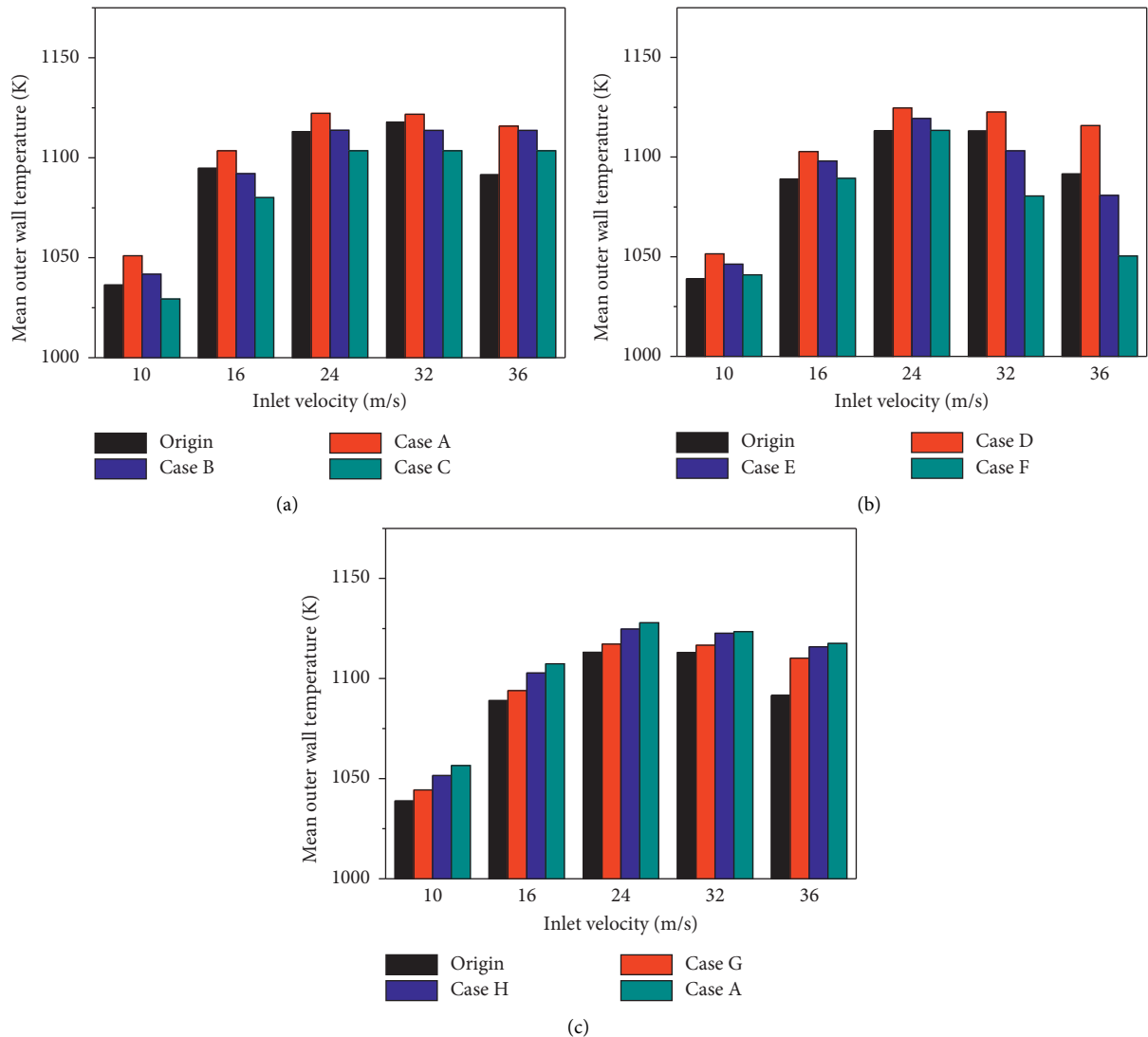


FIGURE 7: Average wall temperature versus inlet velocity for the combustor under $\Phi = 0.4$.

resistance in the horizontal direction caused by the thinning of the outer wall of the cavity. Moreover, the combustion chamber with H equal to 0.75 mm has the highest mean wall temperature, followed by that with H equals 0.5 mm, 0.25 mm, and the original combustion chamber (Figure 7(c)). This phenomenon occurs because the high rib height enlarges the area of the recirculation and low-velocity zones, thereby prolonging the residence time of the mixture and boosting the heat transfer between the mixture and wall.

Figure 8 presents the radical OH distribution of the original and improved microcombustion chambers. Accordingly, the equivalence ratio and inlet velocity are maintained at 0.4 and 10 m/s, respectively. Figure 8 shows that when the inlet velocity equals 10 m/s, the highest mass fractions of OH in the microcombustors are approximately identical. The reaction zone is mainly located in the cavities of the original combustor. Low-velocity and recirculation zones are formed in the cavities, which anchor the flame and provide a high local temperature and an improved heat

recirculation region. In addition, the OH concentration in the boundary layer in the combustion chamber of $L_3 = 1.25$ mm, $H = 0.75$ mm, and $L_4 = 1.25$ mm is higher than those of the original combustion chamber. Given the increase in the upstream and downstream step lengths, the OH concentration in the boundary layer decreases. In addition, the OH concentration in the boundary layer increases with the increase in rib height because the wall temperature level also increases, thereby substantially preheating the mixture and enhancing the reaction intensity.

Figure 9 presents the temperature distribution for different microcombustors, in which the equivalence ratio and inlet velocity are maintained at 0.4 and 10 m/s, respectively. The variation in high-temperature regions is consistent with that in the reaction zones, as demonstrated by the comparison shown in Figure 8. The highest wall temperature zone is near the downstream of the cavities. The outer wall temperature levels of the improved microcombustor are higher than that of the original microcombustor. As the

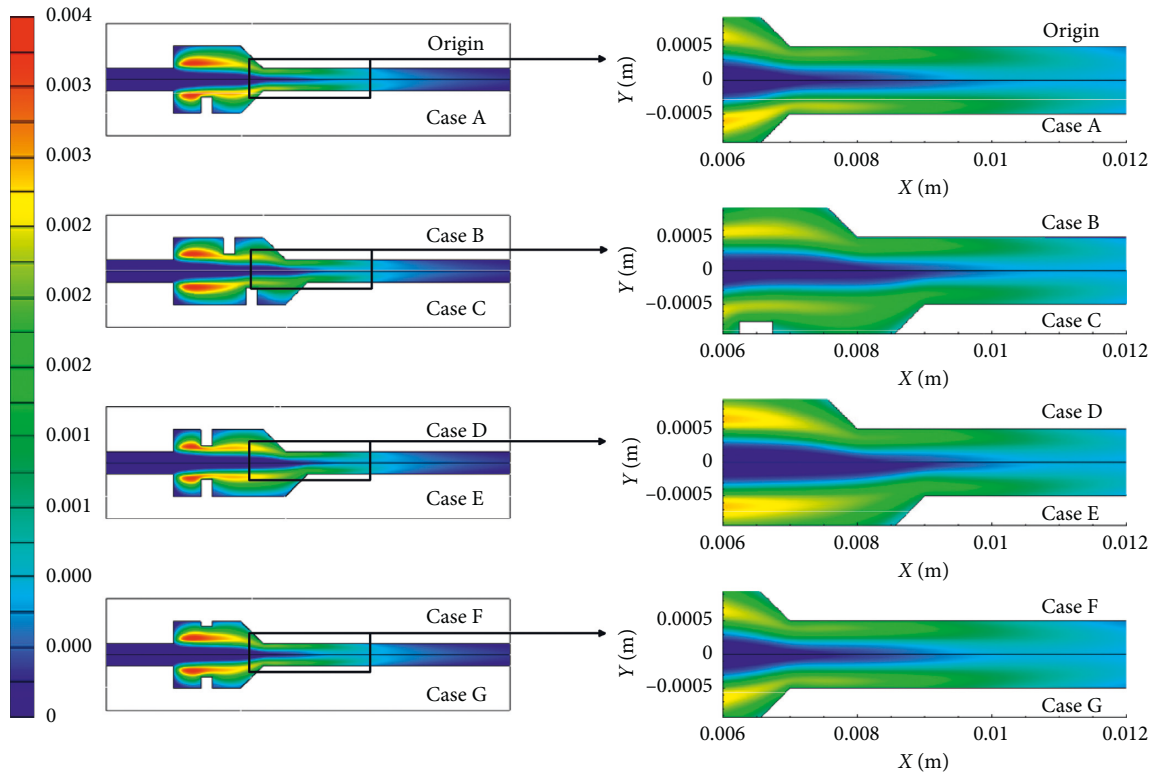


FIGURE 8: Mass fraction contours of OH in the different combustor; the inlet velocity is 10 m/s.

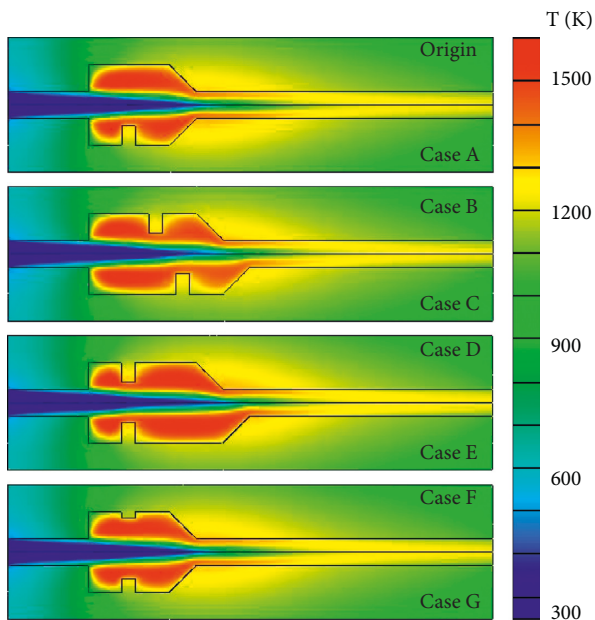


FIGURE 9: Temperature distribution in the different combustor; the inlet velocity is 10 m/s.

upstream and downstream step lengths increase, the area of the high-temperature zone and temperature level near the cavities decrease correspondingly.

Figure 10 presents the radical H_2 distribution of the original and improved microcombustion chambers. Compared with that of the original combustor, hydrogen

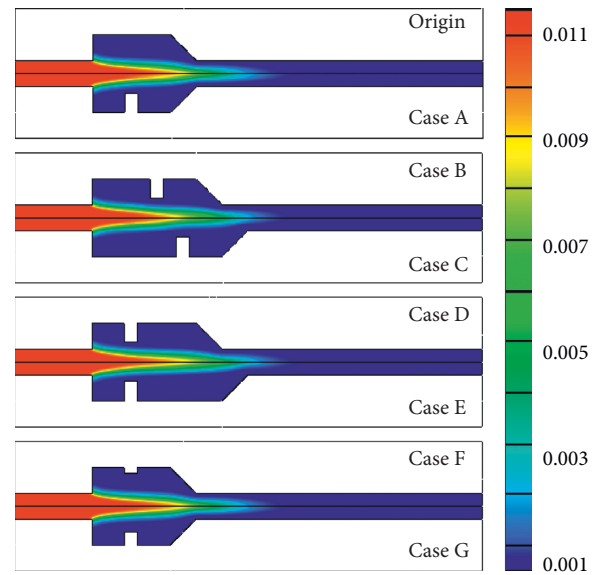


FIGURE 10: Radical H_2 distribution in the different combustors; inlet velocity is 10 m/s.

has a longer consume distance. Moreover, the hydrogen consumes distance increased with the step length. The combustor also has a considerably short hydrogen consume distance with the rib height raised. The combustion chamber of $L_3=1.25$ mm, $H=0.75$ mm, and $L_4=1.25$ mm has the shortest hydrogen consume distance compared with those of other improved combustion chambers.

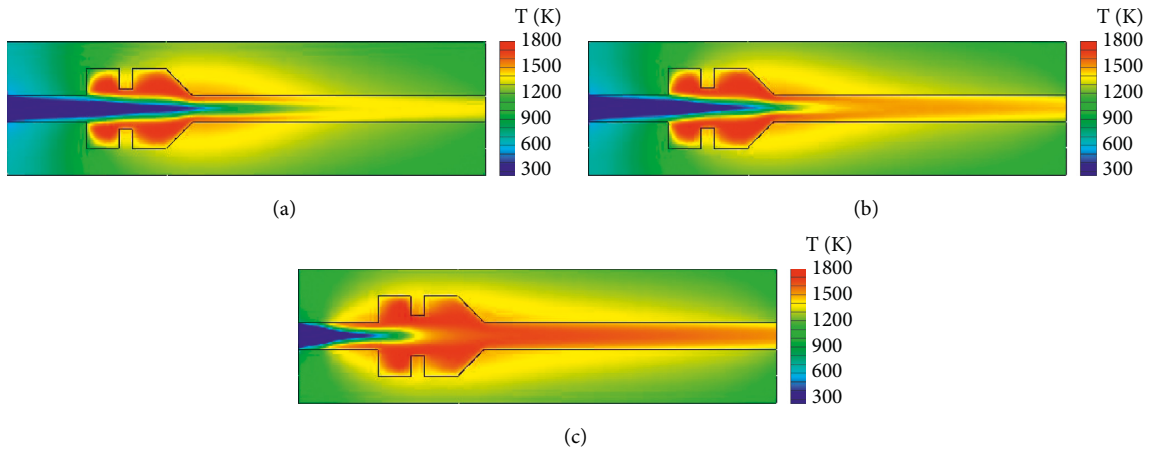


FIGURE 11: Temperature distribution of the improved microcombustor at equivalence ratios: (a) $\Phi = 0.4$, (b) $\Phi = 0.5$, and (c) $\Phi = 0.6$.

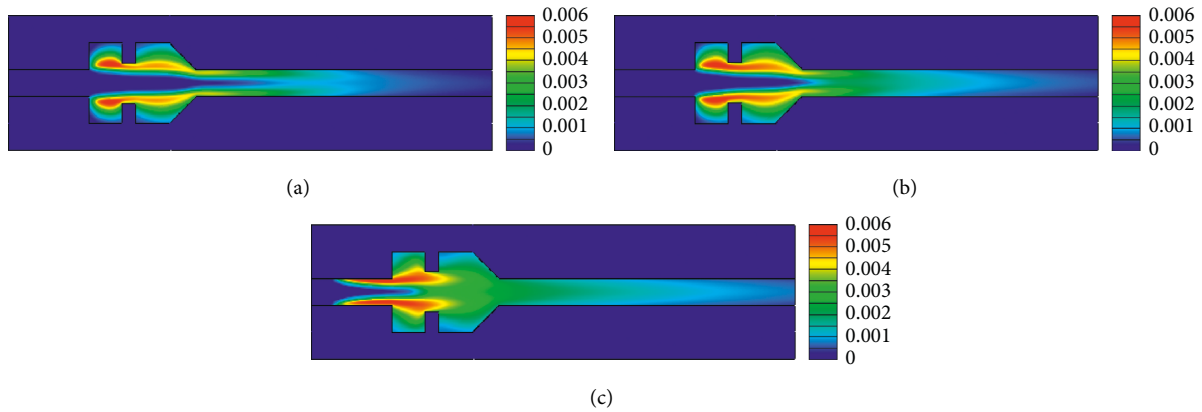


FIGURE 12: OH distribution of the improved microcombustor at equivalence ratios: (a) $\Phi = 0.4$, (b) $\Phi = 0.5$, and (c) $\Phi = 0.6$.

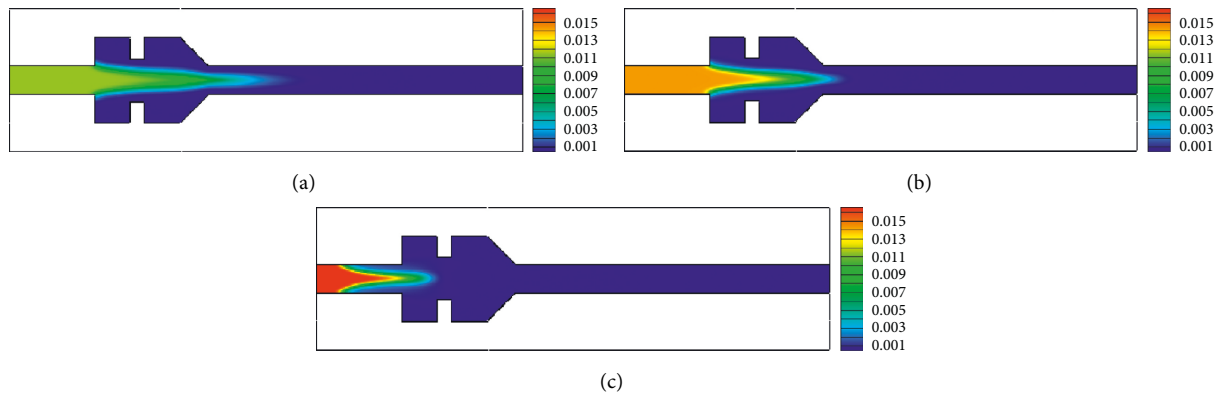


FIGURE 13: H_2 distribution of the improved microcombustor at the following equivalence ratios: (a) $\Phi = 0.4$, (b) $\Phi = 0.5$, and (c) $\Phi = 0.6$.

3.2. Effects of Equivalence Ratio on Combustion Performances of Microcombustors with Rectangular Ribs. Figure 11 shows the contours of the temperature distributions for the microcombustor with the upstream and downstream step lengths and rib height equal to 1.25, 1.25, and 0.75 mm, respectively, under various equivalence ratios. The inlet velocities are maintained at 10 m/s. The temperature levels in the cavities increase as the equivalence ratio is boosted.

This increase indicates that the chemical reaction becomes intensive at large equivalence ratios (Figure 12). When the equivalence ratio is below 0.5, the main reaction zone is located in the cavities. With further increase of the equivalence ratio, the flame front moved upstream in the combustor as the equivalence ratio equals 0.6.

Figure 13 shows the contours of the H_2 distributions for the microcombustor with the upstream and downstream

step lengths and rib height equal to 1.25, 1.25, and 0.75 mm, respectively, under various equivalence ratios. The inlet velocities are maintained at 10 m/s. The hydrogen consumes distance in the combustor decreased with an increase in the equivalence ratio. As the equivalence ratio equals 0.6, hydrogen is consumed completely before the cavities, which means rapid burning speed.

4. Conclusions

This study designed a microcombustion chamber with a rectangular rib. The effects of the step length and rib height on the premixed H₂/air combustion were numerically investigated. The performance of the original design was compared with that of the newly proposed designs under different inlet velocities.

The results show that the new design improves the outer wall temperature profile for the thermoelectric and thermophotovoltaic devices. This outcome occurs because the recirculation and low-velocity zone areas of the improved microcombustion chamber are equal to or above those of the combustor without the rectangular rib. Consequently, the heat transfer between the mixture and the wall is enhanced by the rectangular rib. Moreover, the flow field is not the sole factor that influences wall temperature level because the outer wall profile and average wall temperature of the combustor decrease with step length. This situation is due to the increase in the thermal resistance in the horizontal direction because of the thinning of the outer wall of the cavity, thereby resulting in low heat being conducted upstream through the thin outer wall with a large step length; hence, the upstream and downstream step lengths and rib height equal to 1.25, 1.25, and 0.75 mm microcombustor is recommended due to the higher outer wall temperature and average wall temperature. Moreover, when the equivalence ratio is extremely high (e.g., 0.6), the combustion chamber wall temperature has exceeded the tolerable temperature of the quartz.

A sufficiently high combustor wall temperature level is desired for thermoelectric and thermophotovoltaic devices. Thus, the improved microcombustor is recommended.

Data Availability

The numerical data used to support the findings of this study are included within the article.

Additional Points

Highlights. (1) A microcombustor with an improved rib is proposed. (2) The working performance of combustors with various step lengths and rib height is studied. (3) The combustion performances of the original and improved combustors are compared.

Conflicts of Interest

The authors declare that they have no conflicts of interest.

References

- [1] S. Meziane and A. Bentebbiche, "Numerical study of blended fuel natural gas-hydrogen combustion in rich/quench/lean combustor of a micro gas turbine," *International Journal of Hydrogen Energy*, vol. 44, no. 29, pp. 15610–15621, 2019.
- [2] Q. Peng, W. Yang, E. Jiaqiang et al., "Experimental investigation on premixed hydrogen/air combustion in varied size combustors inserted with porous medium for thermophotovoltaic system applications," *Energy Conversion and Management*, vol. 200, 2019.
- [3] Y. Yan, G. Wu, W. Huang, L. Zhang, L. Li, and Z. Yang, "Numerical comparison study of methane catalytic combustion characteristic between newly proposed opposed counter-flow micro-combustor and the conventional ones," *Energy*, vol. 170, pp. 403–410, 2019.
- [4] Q. Peng, E. Jiaqiang, W. M. Yang et al., "Effects analysis on combustion and thermal performance enhancement of a nozzle-inlet micro tube fueled by the premixed hydrogen/air," *Energy*, vol. 160, pp. 349–360, 2018.
- [5] J. Pan, J. Zhu, Q. Liu, Y. Zhu, A. Tang, and Q. Lu, "Effect of micro-pin-fin arrays on the heat transfer and combustion characteristics in the micro-combustor," *International Journal of Hydrogen Energy*, vol. 42, no. 36, pp. 23207–23217, 2017.
- [6] Q. Peng, Y. Wu, E. Jiaqiang, W. Yang, H. Xu, and Z. Li, "Combustion characteristics and thermal performance of premixed hydrogen-air in a two-rearward-step micro tube," *Applied Energy*, vol. 242, pp. 424–438, 2019.
- [7] G. Wu, Z. Lu, W. Pan, Y. Guan, S. Li, and C. Z. Ji, "Experimental demonstration of mitigating self-excited combustion oscillations using an electrical heater," *Applied Energy*, vol. 239, pp. 331–342, 2019.
- [8] Q. Peng, E. Jiaqiang, W. M. Yang et al., "Experimental and numerical investigation of a micro-thermophotovoltaic system with different backward-facing steps and wall thicknesses," *Energy*, vol. 173, pp. 540–547, 2019.
- [9] Y. Yan, Z. Zhang, L. Zhang, X. Wang, K. Liu, and Z. Yang, "Investigation of autothermal reforming of methane for hydrogen production in a spiral multi-cylinder micro-reactor used for mobile fuel cell," *International Journal of Hydrogen Energy*, vol. 40, no. 4, pp. 1886–1893, 2015.
- [10] R. Wang, J. Ran, X. Du, J. Niu, and W. Qi, "The influence of slight protuberances in a micro-tube reactor on methane/moist air catalytic combustion," *Energies*, vol. 9, no. 6, p. 421, 2016.
- [11] P. Zhang, R. Jing-yu, Z. Zhang, X. Du, W. Qi, and J. Niu, "Investigation on the effect of water vapor on the catalytic combustion of methane on platinum," *Petroleum Science & Technology*, vol. 36, no. 7, pp. 494–499, 2018.
- [12] Q. Peng, E. Jiaqiang, Z. Zhang, W. Hu, and X. Zhao, "Investigation on the effects of front-cavity on flame location and thermal performance of a cylindrical micro combustor," *Applied Thermal Engineering*, vol. 130, pp. 541–551, 2018.
- [13] J. Wan, A. Fan, H. Yao, and W. Liu, "Effect of thermal conductivity of solid wall on combustion efficiency of a micro-combustor with cavities," *Energy Conversion and Management*, vol. 96, pp. 605–612, 2015.
- [14] J. Wan, A. Fan, H. Yao, and W. Liu, "Flame-anchoring mechanisms of a micro cavity-combustor for premixed H₂/air flame," *Chemical Engineering Journal*, vol. 275, pp. 17–26, 2015.
- [15] W. Yang, Y. Xiang, A. Fan, and H. Yao, "Effect of the cavity depth on the combustion efficiency of lean H₂/air flames in a

- micro combustor with dual cavities,” *International Journal of Hydrogen Energy*, vol. 42, no. 20, pp. 14312–14320, 2017.
- [16] J. Wan and A. Fan, “Effect of channel gap distance on the flame blow-off limit in mesoscale channels with cavities for premixed CH_4 /air flames,” *Chemical Engineering Science*, vol. 132, pp. 99–107, 2015.
- [17] G. Bagheri, S. Ehsan Hosseini, and M. Abdul Wahid, “Effects of bluff body shape on the flame stability in premixed micro-combustion of hydrogen-air mixture,” *Applied Thermal Engineering*, vol. 67, no. 1-2, pp. 266–272, 2014.
- [18] E. Jiaqiang, H. Liu, X. Zhao et al., “Investigation on the combustion performance enhancement of the premixed methane/air in a two-step micro combustor,” *Applied Thermal Engineering*, vol. 141, pp. 114–125, 2018.
- [19] W. Zuo, E. Jiaqiang, H. Liu, Q. Peng, X. Zhao, and Z. Zhang, “Numerical investigations on an improved micro-cylindrical combustor with rectangular rib for enhancing heat transfer,” *Applied Energy*, vol. 184, pp. 77–87, 2016.
- [20] J. Wan, A. Fan, and H. Yao, “Effect of the length of a plate flame holder on flame blowout limit in a micro-combustor with preheating channels,” *Combustion and Flame*, vol. 170, pp. 53–62, 2016.
- [21] E. Jiaqiang, Q. Peng, X. Zhao, W. Zuo, Z. Zhang, and M. Pham, “Numerical investigation on the combustion characteristics of non-premixed hydrogen-air in a novel micro-combustor,” *Applied Thermal Engineering*, vol. 110, pp. 665–677, 2017.
- [22] H. Yilmaz, O. Cam, and I. Yilmaz, “Effect of micro combustor geometry on combustion and emission behavior of premixed hydrogen/air flames,” *Energy*, vol. 135, pp. 585–597, 2017.
- [23] I. Yilmaz, H. Yilmaz, O. Cam, and M. Ilbas, “Combustion characteristics of premixed hydrogen/air flames in a geometrically modified micro combustor,” *Fuel*, vol. 217, pp. 536–543, 2018.
- [24] W. Zuo, E. Jiaqiang, and R. Lin, “Numerical investigations on an improved counterflow double-channel micro combustor fueled with hydrogen for enhancing thermal performance,” *Energy Conversion and Management*, vol. 159, pp. 163–174, 2018.
- [25] Y.-f. Yan, H.-y. Yan, L. Zhang, L. Li, J. Zhu, and Z. Zhang, “Numerical investigation on combustion characteristics of methane/air in a micro-combustor with a regular triangular pyramid bluff body,” *International Journal of Hydrogen Energy*, vol. 43, no. 15, 2018.
- [26] M. Ansari and E. Amani, “Micro-combustor performance enhancement using a novel combined baffle-bluff configuration,” *Chemical Engineering Science*, vol. 175, pp. 243–256, 2018.
- [27] L. Li, Z. Yuan, Y. Xiang, and A. Fan, “Numerical investigation on mixing performance and diffusion combustion characteristics of H_2 and air in planar micro-combustor,” *International Journal of Hydrogen Energy*, vol. 43, no. 27, pp. 12491–12498, 2018.
- [28] A. Tang, J. Deng, Y. Xu, J. Pan, and T. Cai, “Experimental and numerical study of premixed propane/air combustion in the micro-planar combustor with a cross-plate insert,” *Applied Thermal Engineering*, vol. 136, pp. 177–184, 2018.
- [29] W. Zuo, E. Jiaqiang, W. Hu, Y. Jin, and D. Han, “Numerical investigations on combustion characteristics of H_2 /air premixed combustion in a micro elliptical tube combustor,” *Energy*, vol. 126, pp. 1–12, 2017.
- [30] S. Akhtar, M. N. Khan, J. C. Kurnia, and T. Shamim, “Investigation of energy conversion and flame stability in a curved micro-combustor for thermo-photovoltaic (TPV) applications,” *Applied Energy*, vol. 192, pp. 134–145, 2017.
- [31] B. Aravind, G. K. S. Raghuram, V. R. Kishore, and S. Kumar, “Compact design of planar stepped micro combustor for portable thermoelectric power generation,” *Energy Conversion and Management*, vol. 156, pp. 224–234, 2018.
- [32] Y.-H. Li and J.-R. Hong, “Performance assessment of catalytic combustion-driven thermophotovoltaic platinum tubular reactor,” *Applied Energy*, vol. 211, pp. 843–853, 2018.
- [33] Y. Yan, W. Huang, W. Tang et al., “Numerical study on catalytic combustion and extinction characteristics of premixed methane-air in micro flatbed channel under different parameters of operation and wall,” *Fuel*, vol. 180, pp. 659–667, 2016.
- [34] J. Ran, L. Li, X. Du, R. Wang, W. Pan, and W. Tang, “Numerical investigations on characteristics of methane catalytic combustion in micro-channels with a concave or convex wall cavity,” *Energy Conversion and Management*, vol. 97, pp. 188–195, 2015.
- [35] C. Luo, Y. Li, Z. Liu, and Y. Dong, “Catalytic combustion of low concentration methane in micro-combustor,” *CIESC Journal*, vol. 66, pp. 216–221, 2015.
- [36] J. Pan, R. Zhang, Q. Lu, Z. Zha, and S. Bani, “Experimental study on premixed methane-air catalytic combustion in rectangular micro channel,” *Applied Thermal Engineering*, vol. 117, pp. 1–7, 2017.
- [37] J. M. Rodrigues, M. F. Ribeiro, and E. C. Fernandes, “Catalytic activity of electrodeposited cobalt oxide films for methane combustion in a micro-channel reactor,” *Fuel*, vol. 232, pp. 51–59, 2018.
- [38] Y. Wang, J. Zhou, Q. Zhao, W. Yang, J. Zhou, and Y. Zhang, “Comparison of catalytic combustion of methane and n-butane in microtube,” *CIESC Journal*, vol. 68, pp. 896–902, 2017.
- [39] C. H. Kuo and P. D. Ronney, “Numerical modeling of non-adiabatic heat-recirculating combustors,” *Proceedings of the Combustion Institute*, vol. 31, no. 2, pp. 3277–3284, 2007.
- [40] J. Li, Z. Zhao, A. Kazakov, and F. L. Dryer, “An updated comprehensive kinetic model of hydrogen combustion,” *International Journal of Chemical Kinetics*, vol. 36, no. 10, pp. 566–575, 2004.
- [41] J. Wan, W. Yang, A. Fan et al., “A numerical investigation on combustion characteristics of H_2 /air mixture in a micro-combustor with wall cavities,” *International Journal of Hydrogen Energy*, vol. 39, no. 15, pp. 8138–8146, 2014.